Université catholique de Louvain
École polytechnique de Louvain
Institute of Mechanics, Materials and Civil Engineering

The failure of metal-to-metal adhesive joints: numerical modelling, energy contributions and constraint effects

Philippe Martiny

Thèse présentée en vue de l'obtention du grade
de docteur en sciences de l'ingénieur

Composition du jury

Prof. Th. Pardoen (Promoteur)	Université catholique de Louvain
Prof. A.J. Kinloch (Promoteur)	Imperial College London
Prof. G. Winckelmans (Président)	Université catholique de Louvain
Dr. F. Lani (Secrétaire)	Université catholique de Louvain
Prof. F. Delannay	Université catholique de Louvain
Prof. V. Tvergaard	Technical University of Denmark
Prof. J-P. Ponthot	Université de Liège

Août 2012

Acknowledgements

First of all, I would like to thank my supervisors: Prof. Th. Pardoen, Prof. A.J. Kinloch and Dr. F. Lani (who I have always considered as one of my supervisors too). It has been an honor and a real pleasure working with you. Each one of you brought his own expertise into this project and they all complemented each other perfectly. Through our different meetings, either here in Belgium or in U.K., you made me discover that good food and science go together well! Thank you also for your patience. I know that I was sometimes kept away from this thesis for too long periods of time…

I shall not forget of course Prof. C. Landis whom I did not get the chance to have many contacts with but who was kind enough to provide us with the finite element code at the basis of most of the developments made in this thesis. Thank you for that. I hope you will be happy with what it has become.

I would like also to thank Dr. M. Delanaye, General Manager of Cenaero, for giving me the opportunity to do (and to finish) this Ph.D. thesis. This project would not have been possible without the financial support of Cenaero, Wallonia and the European ERDF funds, first through the contract N° EP1A122030000102 and then through the SINUS project.

I would like to thank Prof. G. Winckelmans, Prof. F. Delannay, Prof. J.-P. Ponthot and Prof. V. Tvergaard for being part of the jury and for the time they will devote to appraise this thesis. I hope you will enjoy reading it and I am looking forward to discuss with you in more details what has been achieved… but also what would be the next steps!

All my gratitude goes to the many people at the Université catholique de Louvain (M. Sinnaeve and Emile) and at Imperial College (L. Kawashita, S. Rodriguez Sanchez, B.R.K. Blackman, G. Williams, R. Moore, P. Cook and A. Taylor) for their warm welcome and their experimental assistance every time I needed to carry out some tests myself or to get them done. Thank you also for the many fruitful discussions we have had.

I am grateful to D. Dumas and B. Wucher, both now working at Cenaero, for all the work they did on the finite element program as part of their student projects. Thank you also to you and to the other members of the composites team at Cenaero. Lately, I was quite busy finishing this thesis and I am afraid I did not give you all the support you might have needed.

There are of course many more people at Cenaero that I would like to thank for their help, for the discussions we had or simply for the good moments that we shared. My thoughts go especially to M. Duflot and E. Wyart, my first colleagues with F. Lani in the MMM team, to D. Coulon, for her support in Fortran programming, and to V. Madhavan for the help he has offered me so many times.

Finally, last but not least, I would like to thank my family for their continuous support and affection and for their great help over the last few weeks, in various domains, which made it possible for me to complete this thesis. I would like also to give my wife, Sylvie, a special thank for having taken care of our two little girls so as to give me more time to work on this thesis as well as for her huge help at the very end.

To my wife,
Sylvie,

And to our two lovely girls,
Élodie and Charline

Table of Contents

Chapter 1
Introduction

1.1. About adhesive bonding and structural applications

Adhesive bonding is a joining technique which consists of using an intermediate material layer which adheres to, and hence bonds together, two substrates or adherends. Adhesives are being used in many different applications (e.g. packaging, electronics, shoes, dentistry, etc.) but the focus will here be on structural applications, that is, on applications where significant loads need to be transferred from one adherend to the other (e.g. as found in the aerospace, vehicle, rail transport, marine, etc. industries). Most adhesives used in these types of application are polymeric materials (CETIM, 2006; Kinloch, 1997): epoxies, urethanes, phenolics, acrylics and cyanoacrylates, the chemical composition of which is usually modified with second-phase particles to enhance their baseline properties. Figure 1.1 shows that epoxies and urethanes largely dominate the market of structural adhesives (Broxterman, 2001). These adhesives are generally applied in the liquid state to the adherends and solidify by a chemical reaction, making the joining technique an irreversible process. To make it possible to store the adhesives in the liquid state for extended periods of time (referred to as the shelf life of the adhesive), this chemical reaction usually requires some external factor to initiate it, and/or to proceed at a significant rate. This external factor can be (CETIM, 2006): the mixing of two reactants, an elevation of the temperature, exposure to UV light, the ambient humidity, etc. Now, the capability of the joint to transfer the loads across it will not only depend upon the intrinsic resistance of the adhesive material but also on the resistance of the two adhesive/adherends interfaces. To assist in obtaining the required degree of intrinsic adhesion, the adherends generally undergo a surface preparation treatment, such as (CETIM, 2006; Kinloch, 1997) degreasing, grinding, chromic acid etching, plasma treatment, corona discharge, application of a primer, etc., prior to the application of the adhesive. The role of this surface treatment is boost the intrinsic adhesion of the

adhesive to the adherends, especially over time with respect to the potentially negative action of the environment the joint will be subjected to in-service.

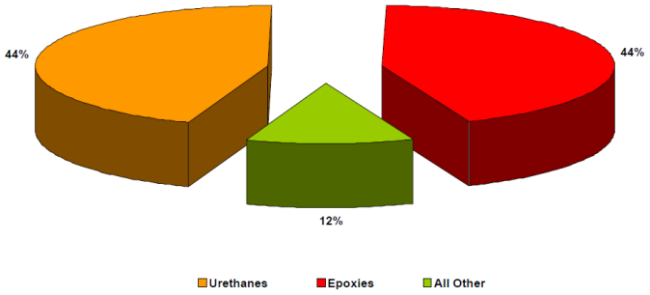

Figure 1.1: The market of structural adhesives broken down into raw material classes (Broxterman, 2001)

As opposed to other joining techniques found in structural applications such as bolting, riveting or welding, adhesive bonding offers a number of significant advantages (see e.g. CETIM, 2006; Kinloch, 1997), some of which are listed below:

- A more uniform stress distribution across the joint, as illustrated in Figure 1.2(a), which potentially results in stiffer assemblies (see Figure 1.2(b)) and in an increased service-life under cyclic-fatigue loading; this more uniform stress distribution is a direct consequence of the elastic-plastic behaviour of most adhesives and of the absence of holes in the adherends which is of particular interest to the joining of composite materials since drilling is likely to induce delamination;
- A reduced weight for a given load capability which is of great interest to the transportation industry;
- Increased damping properties, due to the viscoelastic properties of the adhesive materials, and, hence, an increased service-life in high-cycle fatigue or under vibration loadings; which is of particular interest in the construction of helicopter and wind-turbine blades, for example;
- The possibility to join dissimilar materials, such as honeycomb core to aluminium or composite skins or glass windshields to metal car bodies, and insulate them electrically from each other which is very useful when joining two different metals that are subject to electrochemical corrosion when brought into contact;
- The sealing effect that can be achieved by the joint;
- The reduced manufacturing costs through automation which is of great interest to the automotive sector in which each and every Euro that can

be saved on a given operation results in large savings due to the size of the production line.

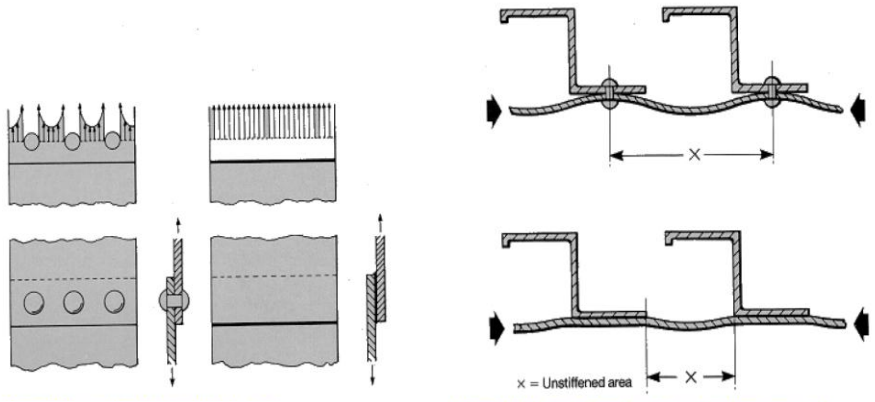

(a) *(b)*

Figure 1.2: (a) Typical stress distributions at mid-overlap in riveted and bonded lap joints, and,(b) comparison of the resulting stiffening effect (Ciba Geigy, 1995)

The above advantages are however balanced by some disadvantages (see e.g. CETIM, 2006; Kinloch, 1997):

- Adhesive joints exhibit a low resistance to cleavage and peel stresses;
- As already mentioned earlier, surface treatment of the adherends is often required to obtain durable joints, especially in hostile environments;
- The upper-service temperature of adhesive joints, typically of the order of 100-175°C, is relatively lower compared to other joining techniques owing to the limited temperature that can be withstood by the polymeric materials which form the adhesives;
- Adhesives exhibit lower strength and toughness than many metals and, hence, are only effective in joining thin sheets of metals or composites; e.g. using them for joining thick metal components would make the joint the weakest link of the structure, which is not desirable as the adherends would then be used well below their load capabilities;
- There is a lack of reliable, proven non-destructive inspection techniques which is best illustrated by the point-of-view expressed still recently by the international airworthiness authorities (FAA CA 20-107B, 2009): " … for the future advancement and validation of non-destructive inspection (NDI) technology to detect weak bonds, which degrade over time and lead to

adhesion failures is urgently needed. Such technology has not been reliably demonstrated at a production scale to date ... ";

- There is a lack of unified design and analysis approaches that are reliably applicable to any joint geometry, loadings conditions or adhesive material without requiring an excessive amount of testing (Crocombe and Kinloch, 1994; McCarthy, 1996; Duncan, 1999; Tomblin et al., 2005) and, hence, relatively high development costs and/or a longer time-to-market.

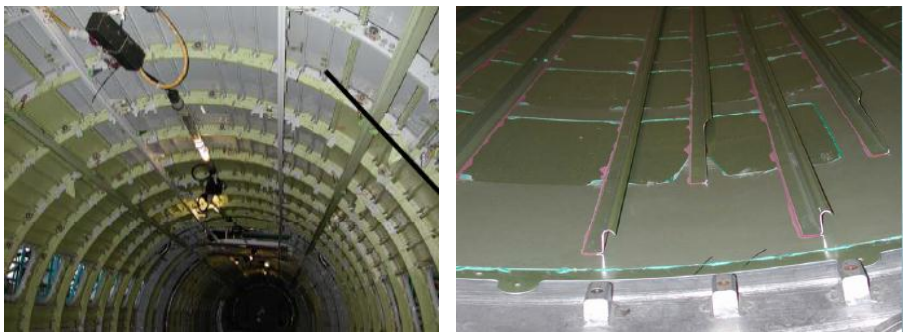

(a) *(b)*

Figure 1.3: (a) Interior view of the fuselage of the ATR 72 aircraft, and, (b) close-up view of the stringers bonded to the skin of the fuselage (Voto, 2004)

1.2. Adhesive bonding for structural applications in aeronautics

Adhesive bonding has been used in aeronautics for a very long time due to its great potential for cost and weight savings and to the increased aerodynamic performance of the assemblies. Figure 1.3 illustrates, as an example, the use of adhesives in the ATR 72 aircraft to bond metal stringers to the metal skin of the fuselage. Nevertheless, adhesive bonding is, to date, still little used in aerospace applications for the bonding of primary structures[1] or, at least, not as the sole method of joining. As an example, Figure 1.4 illustrates the bonding of the two halves making up the composite fuselage of the Adam A500 aircraft which requires the addition of a doubler by wet lay-up and of fasteners.

[1] "Components which are fracture or fatigue critical …, components the single failure of which would cause significant danger to operating personnel or would result in an operational penalty. This includes, loss of major components, loss of control…" (MIL-HDBK-83377, 1997)

(a) *(b)*

Figure 1.4: (a) Adam A500 aircraft and (b) view of the two halves of the fuselage being bonded together (Harter, 2004)

The reason behind this limited use of adhesive bonding in primary structures is that aircraft manufacturers have not been able, so far, to meet the airworthiness requirements, at least without increasing dramatically the development costs and/or the time-to-market. Indeed, three possible means of complying with these requirements are made available to the aircraft manufacturers by the international airworthiness authorities (FAA AC 20-107B, 2009):

1. The maximum disbond of each bonded joint consistent with the capability to withstand the required loads must be determined by analysis, tests or both. Disbonds of each bonded joint greater than this must be prevented by design features.
2. Each joint must be proof-tested to the limit design load.
3. Each bond area must undergo a thorough non-destructive inspection to ensure the strength of the bond.

The first part of item 1 implies relatively large testing costs since, as will be shown later, there are no proven, widely applicable analysis methodologies. Item 2 is associated with even higher testing costs. And, finally, item 3 is presently not possible, since the technology does not currently exist as recalled from the above airworthiness authorities (FAA AC 20-107B, 2009).

1.3. Design practices

Adhesive joints can in general be subject to any combination of the different types of loadings depicted in Figure 1.5: tensile, compression, cleavage, shear and peel. Peel and cleavage loadings induce very high stresses on the boundary line of the joint and are, therefore, very detrimental to the integrity of the joint. On the other hand, compression, tension and shear loadings utilise the joint area to the best advantage in the sense that the load is more uniformly distributed. However, tension loadings can very easily induce significant peel or cleavage loadings if the

load is at all offset. As a consequence, the good design-practice guides (e.g. MIL-HDBK-691B, 1987; MIL-HDBK-83377, 1997; CETIM, 2006) recommend designing the joint for the adhesive to be essentially loaded in shear (or in shear combined with compression) and to minimise as much as possible the generation of peel and cleavage stresses. Figure 1.6 shows some typical joint designs following that recommendation.

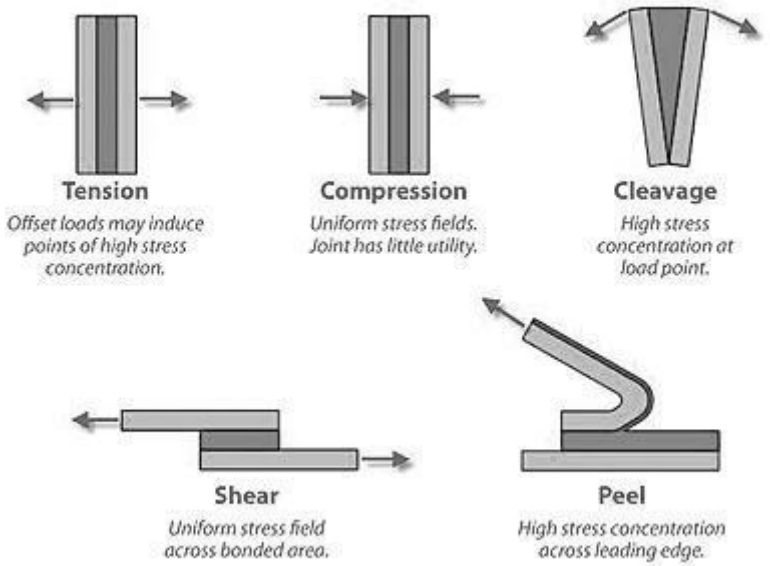

Figure 1.5: Different types of loadings an adhesive joint can be subject to (Dewolfe and Gedney, 2010)

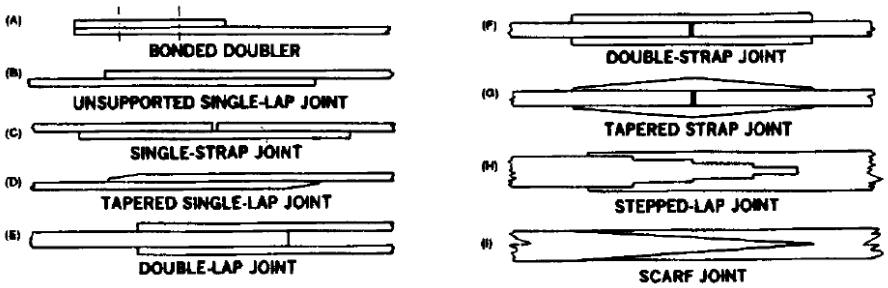

Figure 1.6: Joint designs typically used (MIL-HDBK-17-3F, 2002)

For the case of an adhesive joint being essentially loaded in shear, with only limited peel stresses, the simplest design approach for static load cases consists in using a cut-off value for the average shear stress equal to 500 psi or 3.45 MPa (Harter, 2004), that is, to design the joint to have a sufficient area for the ratio of the load to that area to remain below 500 psi. This rule-of-thumb, which does not even take into account the particular adhesive being used, is only used in early design phases and is over-conservative.

A far more accurate option is to size the joints with the help of diagrams giving the shear strength as a function of the ratio of the length of the overlap to the thickness of the adherends (MIL-HDBK-691B, 1987). Figure 1.7 shows an example of such a diagram and illustrates results which are well-known to joint designers, namely, that there is no real benefit in increasing the length of the overlap or the thickness of the adhesive layer past a certain point. Each curve in such a diagram contains multiple design points which are only valid for a particular joint geometry, loading conditions, adherend and adhesive materials, thickness of the adhesive layer, test temperature, etc. Although quite rigorous, this design methodology requires a large amount of experimental data to provide the designer with sufficient curves and sufficient flexibility in terms of adhesive materials and thicknesses of the adhesive layer.

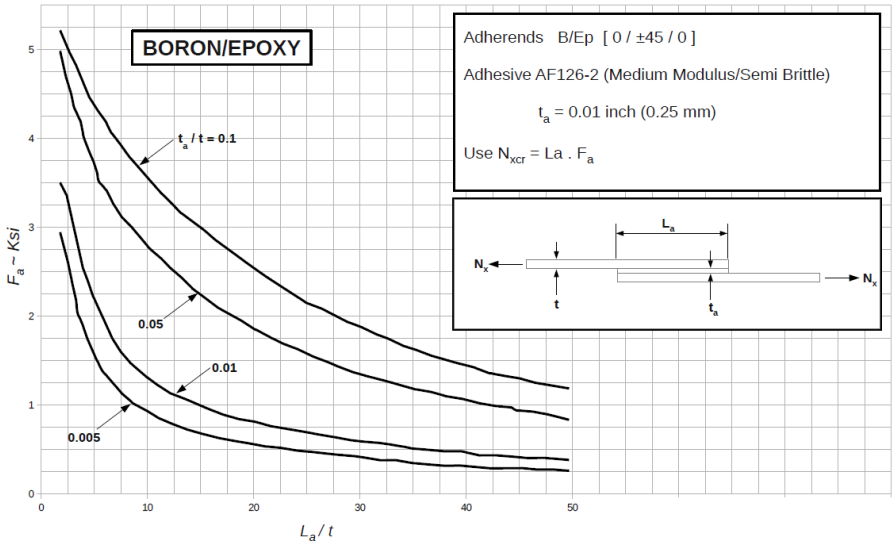

Figure 1.7: Typical design curves for adhesive joints (MIL-HDBK-691B, 1987)

Another commonly adopted methodology in industry, consists in calculating the stresses in the joint from a closed-form solution, applicable to the joint geometry being considered and accounting for the elastic-plastic behaviour of the adhesive, and to apply the design rules derived from the work of Hart-Smith (1981), some of which are illustrated in Figure 1.8:

- the bond should be sized for up to 50% higher load capability than the adherends;
- the minimum stress in the joint should be 10% of the adhesive yield stress (to avoid having an over-conservative design);
- a low stress, elastic region of 6 times the elastic decay length[2], should be included for creep resistance and flaw tolerance.

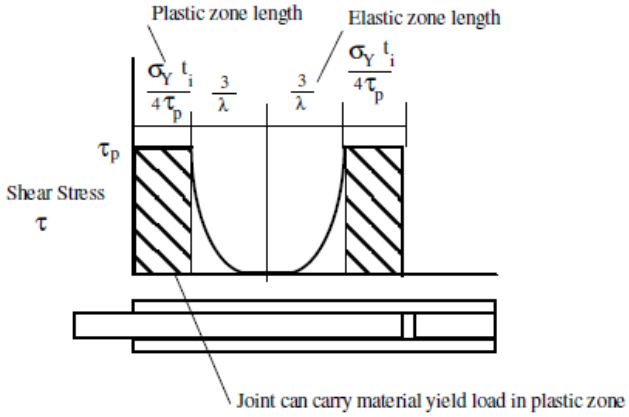

Figure 1.8: Stress distribution over the overlap in a lap joint sized according to the generally accepted design rules (Davis, 1994)

This methodology only requires, as test data, the elastic-plastic stress-strain behaviour in shear of the adhesive, which is typically obtained with the thick adherend test (ASTM D5656), and is, hence, more efficient than the methodology described earlier which necessitates design curves similar to the ones in Figure 1.7. Nevertheless, as loadings and failure modes are always more complex in a full component, joints designed this way always need to be substantiated at the

[2] Characteristic length over which the shear stresses significantly decay from the yield stress value.

different structural levels (Fawcett, 2004) of the building block approach to design represented in Figure 1.9.

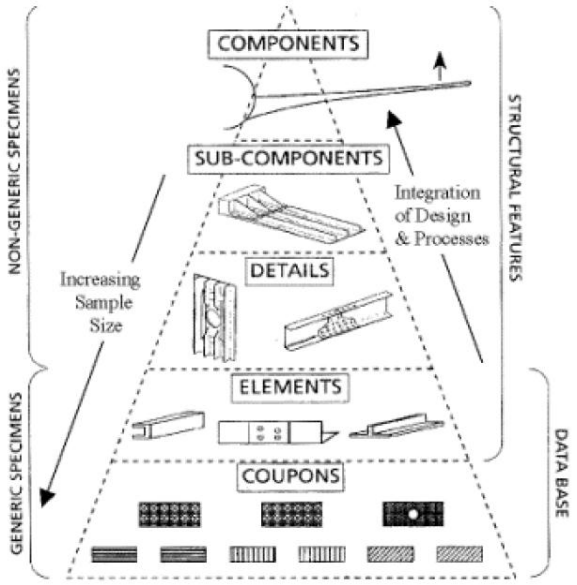

Figure 1.9: The building block approach to design (Tomblin et al., 2005)

The above methodology cannot unfortunately be applied when (Hoyt and Ward, 2004):

- peel stresses are significant, which occurs for example in the well-known stringer pull-off case (Fawcett, 2004);
- failure modes in the adherend need to be taken into account because they are competing with the failure in the adhesive;
- fatigue loadings and/or defects such as barely-visible impact damages (BVID) and cracks, need to be taken into consideration, e.g. for certification purposes.

To tackle these cases, designers can use the more elaborate analysis methodologies described in the next Section, essentially to try to improve the design and to mitigate the risk of failure, but there is no proven solution that is widely used in industry (Hoyt and Ward, 2004). In the end, extensive testing is always made to verify that the design holds against these cases (Hoyt and Ward, 2004).

1.4. Analysis methodologies

A detailed review of the work that was carried out up to 1994 was given by Crocombe and Kinloch (1994). The different methodologies that can be found in the literature for bonded joints that contain no defects and are subjected to only short-term static loadings consist of:

- Calculating the stresses and strains either analytically (see e.g. Volkersen, 1938; Goland and Reissner, 1944; Hart-Smith, 1973, 1981; Oplinger, 1994; Mortensen and Thomsen, 2002) or through finite element analysis (see e.g. Clarke and McGregor, 1993; Crocombe et al. 1995; Cui et al., 2003; Hadavinia et al., 2006) and using a failure criterion based on the attainment of:
    - a particular stress (see e.g. Hart-Smith, 1973; Clarke and McGregor, 1993; Crocombe at al., 1995) or strain (Crocombe et al. 1995; Cui et al., 2003; Hadavinia et al., 2006) either anywhere in the adhesive, at a certain critical distance from a stress singularity, or as an average over a certain distance;
    - a limit load at which the entire adhesive layer yields (Crocombe, 1989);
    - a critical opening displacement past the crack tip;
    - a critical stress intensity factor or, more frequently, an energy release rate (see Hamoush and Ahmad, 1989; Fernlund et al., 1991; Papini et al., 1994) computed with a domain integral or the VCCT technique (Panigrahi and Pradhan, 2007) or from energy balance considerations (Davidson, 1998);
- Using finite element analysis with cohesive zone models to represent either the full thickness of the adhesive layer (Yang et al., 1999; Ferracin et al., 2003) or the local damage mechanisms that are responsible for the failure (Tvergaard and Hutchinson, 1996; Landis et al., 2000; Pardoen et al., 2005; Ferracin et al., 2003; Cooper et al., 2012) and which can predict the onset of failure as well as the ensuing crack propagation;
- Using finite element analysis with continuum damage mechanics principles according to which the material behaviour depends upon a damage parameter that continuously evolves as the material is loaded and continuously degrades the mechanical properties of the material until failure (Imanaka et al., 2003).

Some of the above methodologies were shown to give accurate predictions on a limited set of configurations. However, no unified approach has really emerged that is recognised as being reliably applicable, with a limited amount of material characterization, to any joint geometry, loading conditions or adhesive material

(Crocombe and Kinloch, 1994; McCarthy, 1996; Duncan, 1999; Tomblin et al., 2005). The difficulty of finding such an approach arises, among others, from:

- The fact that most of the criteria that have been proposed are semi-empirical in the sense that they do not rely on the physics of the mechanisms responsible for fracture and, as a consequence,
    - their validity is usually limited to a small number of the joint configurations from which they have been developed (McCarthy, 1996);
    - the particular values of their material parameters are only valid for a given range of joint geometries and, more particularly, adhesive layer thicknesses (see e.g. Yang et al., 1999; Cui et al., 2003);
- The complexity of the behaviour of the adhesive materials, typically nonlinear viscoelastic and temperature dependent, which results from their polymeric nature combined with their complex multi-phase microstructure (Dean and Crocker, 2001);
- The difficulty of measuring experimentally the different material properties that are needed (for example, the ISO standard 25217:2009 for measuring the adhesive fracture energy in mode I loading was only published in 2009, and there is to date no standard for measuring that adhesive fracture energy in mode II loading);
- The significant effect that the details of the manufacturing process can have through:
    - the geometry of the adhesive layer with spew fillets which, for example, significantly modify the strength of single-lap joints (Adams and Wake, 1984) and is illustrated in Figure 1.10 (Grant et al., 2009);
    - the properties of the adhesive which may depend upon the thermal history during cure (Duncan, 1999);
    - the residual stress distribution that may develop in the adhesive during cure owing to the difference in thermal expansion coefficients between the adhesive and the adherends (Liebl et al., 2012).
- The complexity of the failure modes and the competition between the failure modes that can be observed in real components (MIL-HDBK-17-3F, 2002; Fawcett, 2004).

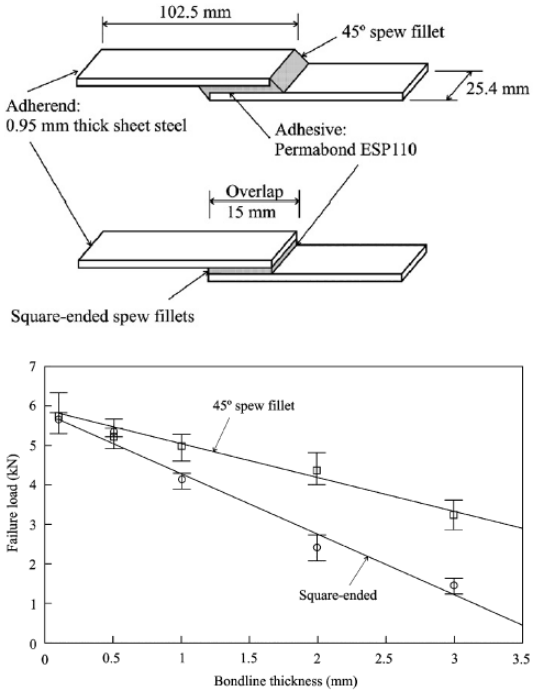

Figure 1.10: Experimental evidence of the effect of the geometry of the adhesive layer and, more particularly,of the spew fillets on the strength of the adhesive joint (Grant et al., 2009)

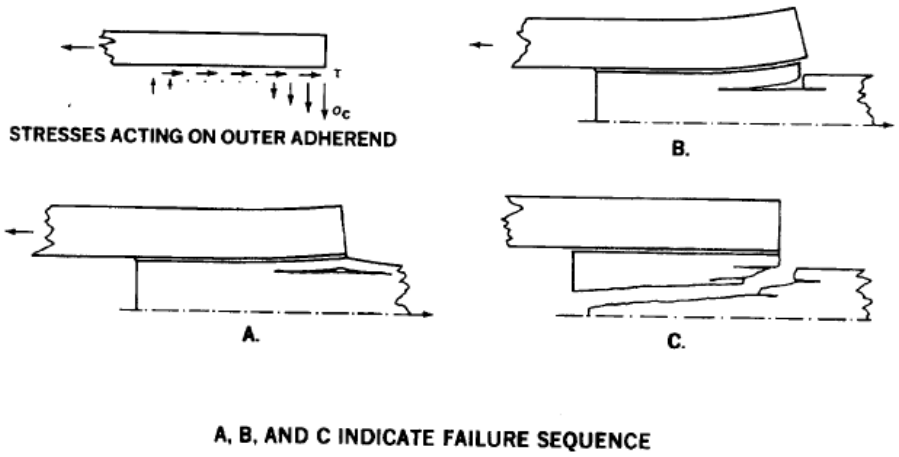

Figure 1.11: Failure modes in composite adherends (MIL-HDBK-17-3F, 2002)

1.5. Scope of the thesis

The present thesis aims to tackle the lack of reliable, generally applicable analysis methodologies. To reduce the scope of this task, the focus of attention will be on:

- Models that are applicable, with constant material parameters, to a large range of configurations, since it is important for the analysis methodology to be considered as generally applicable and to require a reduced amount of testing;
- Epoxy-based structural adhesives, since they are popular structural adhesives (see Figure 1.1) especially in aeronautics due to their good compatibility with polymer-matrix composites;
- Metallic adherends because polymer-matrix composite adherends show different potential failure modes, as can be seen in Figure 1.11, which can be quite complex to model and which can compete with the failure in the adhesive (see e.g. Li et al., 2006);
- Initially cracked joints, since this is in-line with the means of compliance issued by the airworthiness authorities (FAA AC 20-107B, 2009) and also because damage-tolerant design methodologies, which allow for the presence of defects such as cracks, result in more efficient designs;
- Simple test specimens, since in the spirit of the building block approach to design depicted in Figure 1.9, it makes no sense to apply an analysis methodology to larger components if it has not been proven successful on simpler test specimens;
- Mode I loadings or predominantly mode I loadings with some contribution of mode II (the different types of loading that a crack can be subject to are recalled in Figure 1.12), since these are associated with significant peel or cleavage stresses which are known to be very detrimental to adhesive joints and which, therefore , must be properly accounted for;
- Steady-state crack propagation conditions, since adhesives can potentially show an 'R-curve' behaviour (that is, an increase in toughness as the crack propagates) and in that case, steady-state conditions may reflect the limit loading that gives continued crack propagation and, hence, complete failure of the joint;
- Quasi-static loading conditions, since these are the simplest among the types of loading conditions (e.g. fatigue, creep and impact) and, as such, constitute a sound working basis for the development of methodologies applicable to all types of loadings.

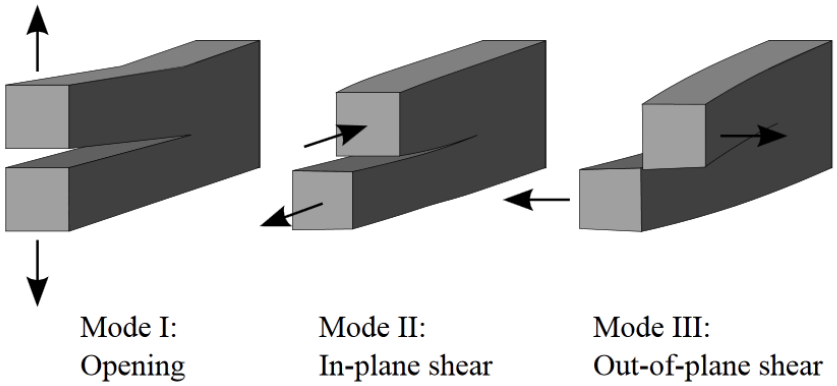

Figure 1.12: The different modes of loadings a crack can be subject to (http://en.wikipedia.org/wiki/Adhesive)

It should be noted that the scope of the thesis fits nicely with other on-going or forthcoming research projects at Cenaero, including:

- The CERFAC FP7 project which one of the two main objectives is: "to reduce the number or fasteners (10 to 100% reduction), the local thickening of fastener areas and minimize the manufacturing & assembly costs (20% reduction)" in composite aerospace structures through "innovative and efficient joining concepts" that could, among others, benefit from the use of adhesive bonding, and through "upgraded design, analysis and testing methodologies";
- The BOPACS FP7 project which the main objective is to "enable secondary bonding as joining technology" for primary composite aerospace structures through the development of means of compliance with the airworthiness requirements and, more particularly, through "thorough research, beyond the state of the art, into the crack growth / disbond extension mechanisms in adhesively bonded joints";
- The composite activities in general since adhesive bonding is clearly one of the most promising methods for joining composites.

1.6. Outline of the thesis

The methodology that will be followed consists of:

- Developing and implementing numerical models applicable to the configurations being focused on;
- Developing and applying suitable methodologies for the identification of the material parameters needed by these models from well-established and widely used tests;

- Critically assessing the accuracy of these models, from an engineering perspective, by confronting their numerical predictions with the available test data;
- Gaining a better understanding of the parameters affecting the toughness of the adhesive joints by conducting thorough parametric studies with the models and analyzing in details the numerical results with a focus on the different energy contributions and constraint effects they depend upon.

The outcome of this work is presented as follows in the manuscript. Chapter 2 details the materials that will be considered in the thesis, the different tests that have been carried out and the resulting experimental data that will be used in the subsequent Chapters to develop and to validate suitable numerical models. Chapter 3 focuses on a first model which relies upon both cohesive zone elements and continuum elements to represent the different mechanisms taking place in the adhesive. The physical motivation behind and the details of the implementation are first reviewed. The model is then applied to a first adhesive, to gauge its capability to reproduce accurately different fracture mechanics tests with a limited number of material parameters. A thorough parametric study of the parameters affecting the toughness of adhesively-bonded joints concludes the study of this first adhesive. Subsequently, the model is applied to a second adhesive, with different properties, to evaluate to which extent it can be applied to other adhesive systems. Conclusions are drawn from the comparison of the performances of the model when used for these two adhesives. Chapter 4 focuses on a completely different model, meant to mitigate the drawbacks of the model developed in Chapter 3, which relies on continuum elements only to represent the adhesive and on a stress based criterion to predict failure. After reviewing the motivation behind that particular model and the details of its implementation, it is applied to three very different adhesives (which include the two adhesives considered in Chapter 3) and critically assessed by confrontation of its numerical predictions with the experimental data detailed in Chapter 2. It is then used to conduct a thorough non-dimensional parametric study of the parameters affecting the toughness of adhesively-bonded joints. Finally, some conclusions are drawn and some perspectives are given in Chapter 5.

Chapter 2
Materials and experimental procedures

2.1. Materials

2.1.1. Adhesive materials

Three different epoxy-based structural adhesives, covering the range of 200-6500 J/m² in their values of adhesive fracture energy[3], G_a, have been studied. They are:

- Adhesive 'Betamate 73455', produced by Dow Automotive, which contains a large fraction of silica particles (Ferracin, 2003) and exhibits an adhesive fracture energy, G_a, of 200-300 J/m² for an adhesive layer thickness, h_{adh}, between 0.1 and 1 mm;
- Adhesive 'ESP 110', produced by Bondmaster, which contains both aluminum and rubber particles (da Silva and Adams, 2002) and which exhibits an adhesive fracture energy of 1000-1500 J/m² for an adhesive layer thickness between 0.1 and 1 mm;
- Adhesive 'Betamate 1493', produced by Dow Automotive, which contains a small volume fraction of small-size silica particles as well as even smaller rubber particles in a large volume fraction (Ferracin, 2003) and which exhibits an adhesive fracture energy of 3500-6500 J/m² for an adhesive layer thickness between 0.1 and 1 mm.

[3] The adhesive fracture energy is defined as the total energy that is expended in the adhesive to propagate a pre-existing crack and increase the crack surface by a unit area.

2.1.2. Adherend materials

Three different adherend materials have been considered in this work. They are:

- mild steel, supplied in the form of 0.78 and 1.20 mm-thick sheets, which was used in combination with the adhesives 'Betamate 73455' and 'Betamate 1493' to make wedge-peel test specimens;
- aluminium alloy (AA) 5754-O, supplied in the form of 1.00 and 1.45 mm-thick sheets, which was used in combination with the adhesive 'ESP 110' to make wedge-peel test specimens and fixed-arm peel test specimens;
- aluminium alloy (AA) 2014, supplied in blocks of bulk material, which was used in combination with three adhesive to make tapered double cantilever beam test specimens.

2.2. Test procedures

2.2.1. Bulk tensile and compression tests

All adherend materials, to the exception of the aluminium alloy 2014, and all three bulk adhesives were tested in uniaxial tension. The bulk adhesive 'Betamate 1493' was also tested in compression. Only the aluminium alloy AA 5754-O and the adhesive 'ESP 110' were tested in the frame of the present thesis. The other materials were tested as part of previous studies.

Flat dumbbell-shaped tensile test specimens were machined out of:

- the mild-steel and aluminium alloy AA 5754-O plates received from the supplier;
- thin plates of bulk adhesive 'Betamate 73455' and 'Betamate 1493' polymerized, following the cure cycle recommended by the supplier, between two thin steel plates protected with Teflon tapes and kept apart by steel wires controlling the gap between the two plates and, hence, the thickness of the adhesive plate being made.

Rounded dumbbell-shaped tensile test specimens were machined out of thick plates of bulk adhesive 'ESP 110' that were prepared in a closed mould following the recommendations of Dean and Duncan (1998) and cured after the cure cycle suggested by the supplier.

Flat cylindrical compression test specimens with different diameter-to-height ratios were machined out of thick plates of bulk adhesive 'Betamate 1493' that were prepared with a procedure similar to the one used to prepare the thick plates of bulk adhesive 'ESP 110'.

All these test specimens were tested with a universal testing machine measuring the force applied to the specimen while an extensometer was measuring their elongation in the waist section.

2.2.2. Wedge-peel tests

All three adhesives were tested with the wedge-peel test, with different adherend materials. Only the adhesive 'ESP 110' was tested in the wedge-peel test in the frame of the present thesis. The other adhesives were tested as part of previous studies.

The wedge-peel test is one of the many types of peel tests (see e.g. ASTM D 903, ASTM D 1876 or ASTM D 3167) that are frequently used in industry for quality control of processes. Most of them consist in measuring the force per unit width, *P/b*, which is referred to as the peel strength that is required to peel apart the two adherends, or substrates, that are initially bonded together. Figure 2.1 shows the different peel test geometries, namely the wedge-peel test and the fixed-arm peel test, that will be specifically dealt with in the present thesis. As the adherends (or one of the adherends) deform plastically in the tests, they are referred to as elastic-plastic fracture mechanics (EPFM) tests.

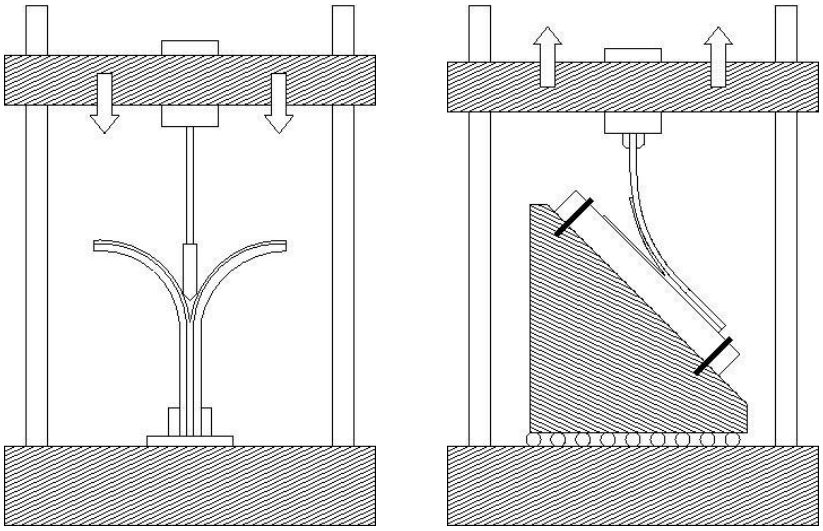

(a) *(b)*

Figure 2.1: Experimental set-up for (a) the wedge-peel test and (b) the fixed-arm peel test

The test specimens were prepared from strips of metal cut from the different sheets of adherend material received from the suppliers. The surface of the aluminium alloy strips were prepared by grit blasting followed by a chromic acid

etch whereas the mild steel strips were only degreased. A layer of adhesive was then deposited with a gun on a first strip, before placing the second strip on top. The thickness of the adhesive layer was controlled by dispersing either short steel wires or glass beads in the adhesive layer or by placing steel wires only at the edges of the specimens. The specimens were finally cured following the recommendations of the adhesive manufacturer.

All specimens were tested in a universal testing machine which, as depicted in Figure 2.1(a), was driving a wedge between the adherends. The load applied by the machine was recorded over time and photographs of the deformed specimens were taken during the test at regular intervals. After testing, the residual radii of curvature of the arms were measured by least-square fitting circles through points located, with the help of a profile projector, on the free surface of the arms. The crack length, a, defined as the axial distance between the crack tip and the contact points with the wedge, was also measured on the different photographs taken during the test. It should be noted that, since the force required to push the wedge is significantly affected by friction, the opening driving force is not a useful parameter for the subsequent analysis.

2.2.3. Fixed-arm peel tests

Only the adhesive 'ESP 110' was tested, as part of another study, with the fixed-arm peel test. It was tested with a single adherend material, namely the aluminium alloy AA 5754-O.

The specimens were prepared similarly to the wedge-peel test specimens and tested, as depicted in Figure 2.1(b) with a universal testing machine. The peel force versus time trace was recorded and an average, steady-state peel force per unit width, P/b, was deduced. The maximum curvature, $1/R_0$, exhibited by the peel arm over its full length was also numerically derived following the methodology described by Kawashita et al. (2005) from digital photographs taken during the course of the test.

2.2.4. Tapered double cantilever beam (TDCB) tests

All three adhesives were tested in the tapered double cantilever beam (TDCB) test depicted in Figure 2.2, with different adhesive layer thickness and a single adherend material, namely the aluminium alloy 2014A. Both the adhesives 'Betamate 73455' and 'ESP 110' were tested in the TDCB test as part of the present thesis whereas the adhesive 'Betamate 1493' was tested as part of another study.

The tapered double cantilever beam test is a standard test (ISO 25217:2009) to measure the adhesive fracture energy in mode I. The particular tapered shape of the adherends was designed to achieve a constant crack growth rate when

imposing, through the crosshead of the testing machine, a constant opening velocity to the tip of the specimen and to prevent the adherends from deforming plastically in the test. As a consequence:

- the TDCB test is referred to as a linear elastic fracture mechanics (LEFM) test;
- no energy is expended in the adherends and the load applied by the testing machine gives a more or less direct measure of the adhesive fracture energy.

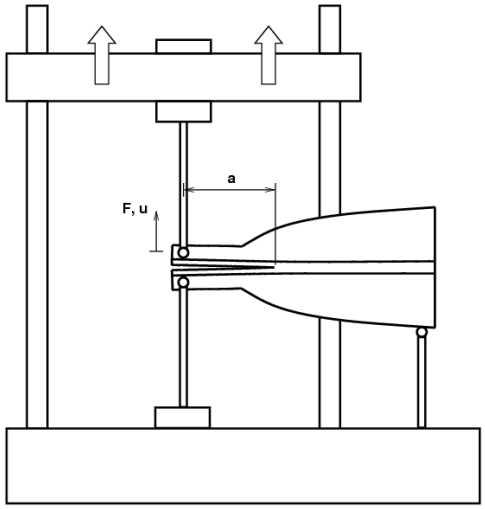

Figure 2.2: The experimental set-up for the LEFM tapered double-cantilever beam (TDCB) test

The specimens were prepared similarly to the wedge-peel test specimens, including the surface preparation treatment (degreasing, grit blasting and chromic acid etch), with the particularity that the adherends needed to be machined from a block of bulk material to the tapered profile with a numerically commanded machine. They were then tested as depicted in Figure 2.2. The load, P, the cross-head displacement, u, and the crack length, a, were recorded as a function of time. From these measurements, the adhesive fracture energy, G_a, was derived as a function of the crack length according to the LEFM corrected beam theory (CBT) (Blackman et al., 2003a):

$$G_a = \frac{4P^2}{EB^2} m \left[1 + 0.43 \left(\frac{3}{ma}\right)^{1/3}\right] \quad (2.1)$$

where B is the width of the specimen and E is the modulus of the beam material. As a cross-check, the value of G_a was also obtained via the LEFM experimental-compliance method (ECM):

$$G_a = \frac{P^2}{2B}\frac{dC}{da} \tag{2.2}$$

where $C = u/P$ is the compliance, the derivative of which, $\mathrm{dC/da}$, is obtained by a regression analysis of a plot of C versus a.

2.2.5. SEM images

The fracture surfaces of some joint test specimens were examined using a scanning electron microscope.

2.3. Test data

2.3.1. Adherend materials

A mild-steel specimen was machined to a dumbbell shape from a 0.78 mm-thick plate of bulk material and tested in tension. The stress-strain curve is shown in Figure 2.3(a) up to a strain of 2%, which is the estimated upper-bound to the strain range experienced by the adherends in the wedge-peel tests.

Three dumbbell-shaped specimens were machined from both 1.00 mm and 1.45 mm thick aluminum-alloy 5754-O sheets and tested in tension using a universal testing machine with a crosshead speed of 1 mm/min. The corresponding stress versus strain curves are shown in Figure 2.3(b). Small differences can be observed as a function of the thickness of the aluminum-alloy specimens and these differences have been taken into account in the later modelling studies.

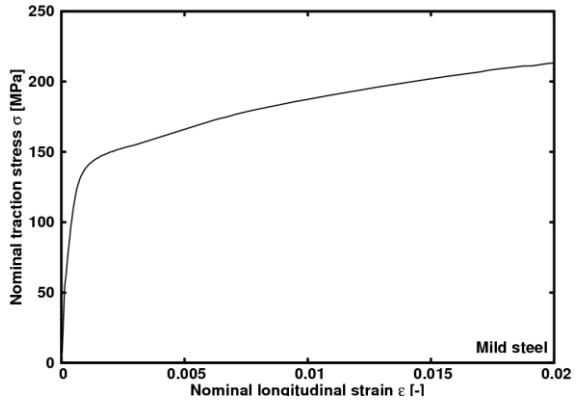

Figure 2.3(a): Experimental tensile stress versus strain curves for the mild steel

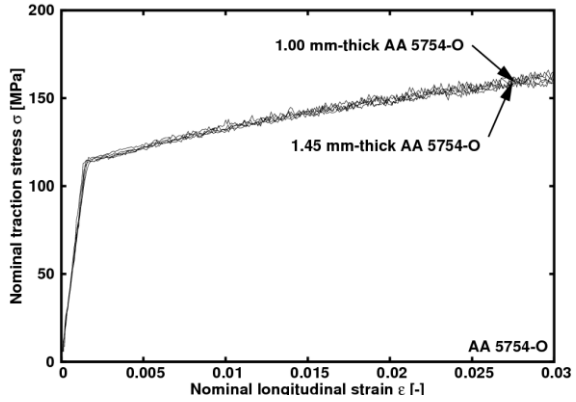

Figure 2.3(b): Experimental tensile stress versus strain curves for the aluminium alloy 5754-O

2.3.2. Adhesive 'Betamate 73455'

Bulk tensile tests

Flat dumbbell-shaped specimens made of bulk adhesive 'Betamate 73455' were tested in uniaxial tension by Ferracin (2003) at different strain-rates ranging from $2.5x10^{-5}$ to $2.5x10^{-2}$ s^{-1}. Figure 2.4 shows the corresponding stress-strain curves. It can be seen that the adhesive exhibits little rate-dependence, little strain-hardening capacity and a relatively small fracture strain of below about 1%.

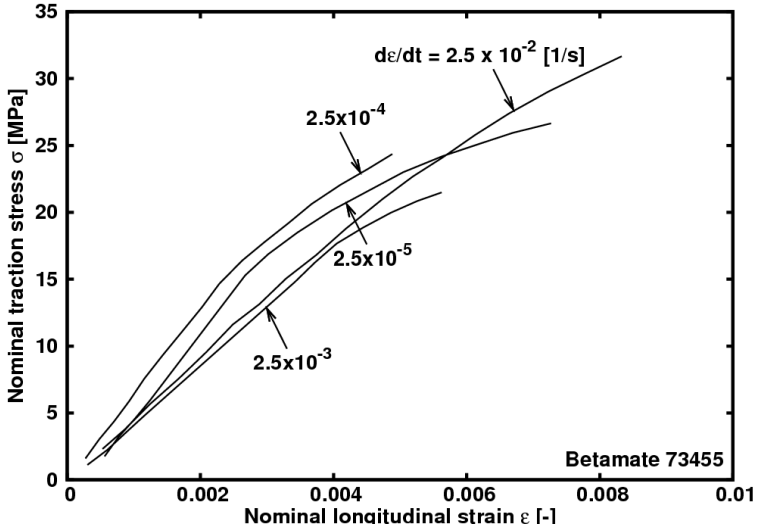

Figure 2.4: Experimental tensile stress versus strain curves for the adhesive 'Betamate 73455'

Wedge-peel tests

The adhesive 'Betamate 73455' has been previously tested using the wedge-peel test specimen by Pardoen et al. (2005). A series of test configurations, with various adhesive layer thicknesses, h_{adh}, were manufactured by bonding together 30 mm wide strips cut from a 0.78 mm thick plate of mild steel, after degreasing the surfaces. The specimens were cured for 45 minutes at 180°C. The specimens were peeled apart in a testing machine by driving a wedge of thickness, D_w, equal to 1.8 mm between the adherends at a crosshead speed of 10 mm/min. The residual radii of curvature, R_1, and R_2, of both arms were obtained after the test by fitting a circle through a set of points taken, using a profile projector, on the free surfaces of the peeled arms. For each specimen, the values of R_1, and R_2 were averaged to give a single value, R_a, according to:

$$\frac{1}{R_a} = \left[\frac{1}{2}\left(\frac{1}{R_1^{n+1}} + \frac{1}{R_2^{n+1}}\right)\right]^{\frac{1}{n+1}} \tag{2.3}$$

where n is the strain-hardening exponent of the substrate material. The results that were obtained are given in Table 2.1 and shown in Figure 2.5. The values quoted, for each specimen geometry, are the mean and standard deviation from five replicate tests, which all showed a locus of failure that was close to the centreline of the adhesive layer and, hence, quasi pure mode I conditions. This observation supports, of course, the averaging of the different radii of curvature. Table 2.1 reveals that the work of fracture increases with increasing thicknesses of the adhesive layer, as illustrated by the smaller radii.

Table 2.1: Experimental EPFM wedge-peel test results for the adhesive 'Betamate 73455' (mild-steel adherend thickness, $h = 0.78$ mm locus of failure: close to the centreline of the specimens)

h_{adh} [mm]	R_a [mm]
0.08	186 ± 14
0.18	128 ± 27
0.24	110 ± 4

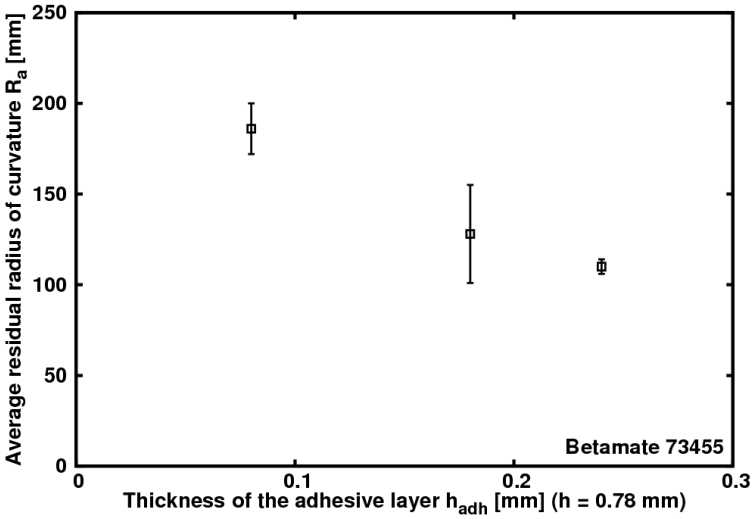

Figure 2.5: Average residual radius of curvature obtained from the wedge-peel test for the adhesive 'Betamate 73455'

Tapered double cantilever beam tests

The mode I adhesive fracture energy, G_a, of the adhesive was obtained experimentally for different thicknesses of the adhesive layer using the LEFM TDCB test specimen. The adherends were machined from bulk aluminium-alloy (grade 2014A) with a taper characterised by a value of m (see ISO 25217: 2009) equal to 2 mm^{-1}. The adherends were then subjected to grit blasting, degreasing and a chromic-acid etch. The TDCB joints were tested to failure using a cross-head speed of 0.2 mm/min. Stable crack propagation mainly occurred. The adhesive fracture energy, G_a, was derived as a function of the crack length according to the CBT theory, see Equation (2.1). As a cross-check, the value of G_a was also obtained via the ECM method, see Equation (2.2). No significant differences in the values of G_a from these two calculation methods were observed, and no significant 'R-curve' was recorded.

The experimental values of the adhesive fracture energy, G_a, are shown in Table 2.2 and in Figure 2.6, where the average and standard deviation values are quoted. All specimens showed a locus of failure that was cohesive through the adhesive layer. The failure was near the centreline of the adhesive layer for most specimens meaning that failure was taking place almost under pure mode I conditions. However, for a few joints which possessed relatively thin adhesive layers, the crack path was close to one of the adhesive/adherend interfaces meaning that failure, though still predominantly mode I, was showing some contribution of mode II. These results are shown separately in Table 2.2. When the crack runs near the centreline of the adhesive layer, the value of G_a increases from

212 to 277 J/m^2 as the layer thickness, h_{adh}, is increased from 0.24 to 0.87 mm; and a local peak in the value of G_a occurs at an intermediate thickness of $h_{adh} \cong 0.4$ mm. However, when the crack runs in the adhesive layer, but close to one of the adhesive/adherend interfaces, the values of G_a are significantly lower.

Table 2.2: Experimental LEFM TDCB test results for the adhesive 'Betamate 73455' (adherend: aluminium alloy).

h_{adh} [mm]	G_a [J/m^2]	Locus of failure
0.24	212 ± 4	Near the centreline of the adhesive layer
0.38	263 ± 13	
0.56	226 ± 12	
0.87	277 ± 42	
0.20	153 ± 3	Near the adhesive / adherend interface
0.41	186 ± 15	

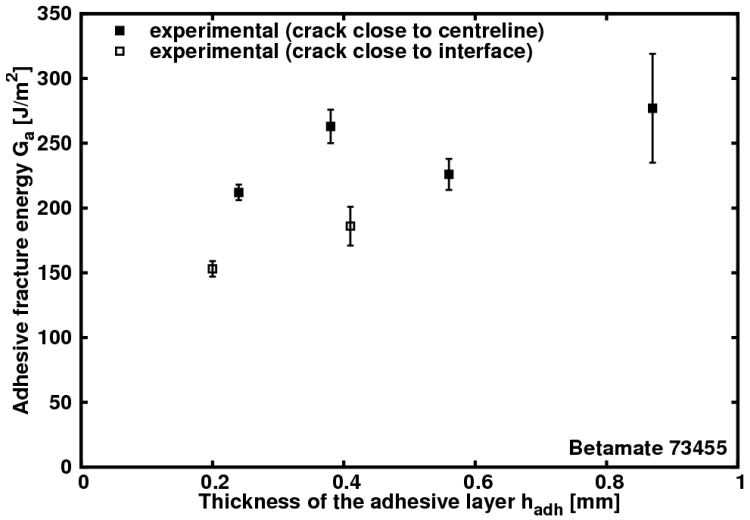

Figure 2.6: Adhesive fracture energy values measured from the TDCB test for the adhesive 'Betamate 73455'

Fracture surfaces

Figure 2.7, obtained by Ferracin (2003) using a scanning electron microscope, shows typical micrographs of the fracture surface of the wedge-peel test specimens. It can be seen in Figure 2.7(b) that failure is accompanied by the cleavage of the silica particles which can be of very different sizes (from 10 µm to 200 µm) and which can be separated by 20 to 200 µm, see Figure 2.7(a-b), depending on their size.

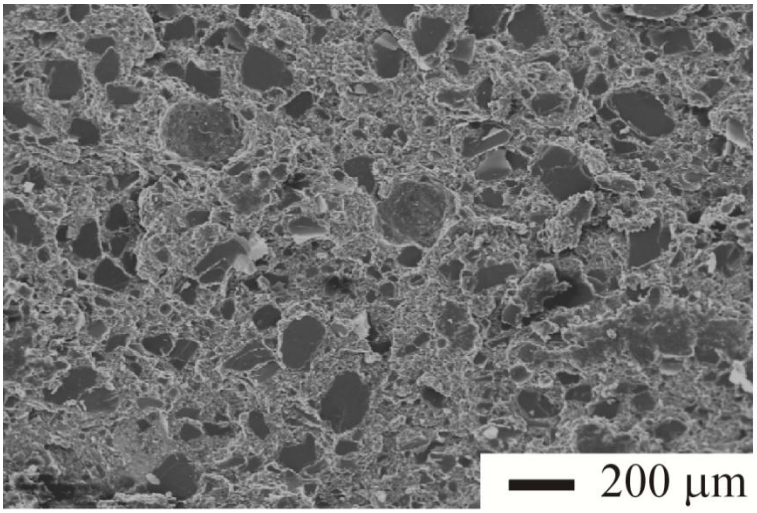

(a)

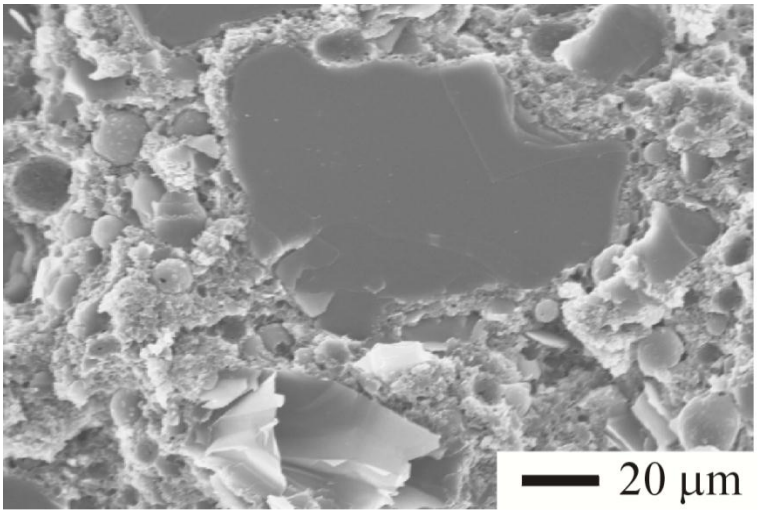

(b)

Figure 2.7: Typical fracture surface of the adhesive 'Betamate 73455' at two different magnification levels

2.3.3. Adhesive 'ESP 110'

Bulk tensile tests

Eight round tension-test specimens were machined from a single bulk adhesive plate, which was cured for 45 minutes at 150°C. The specimens were tested using a universal testing machine with crosshead speeds ranging from 0.1 to 10 mm/min, in order to quantify any possible rate-dependent behaviour. Figure 2.8 shows the corresponding stress-strain curves. It can be seen that the adhesive exhibits little rate-dependence, some strain-hardening capacity and a relatively small fracture strain of the order of 3%. Compared to the stress versus strain curves shown in Figure 2.4, these curves reveal that the adhesive 'ESP 110' shows a similar modulus and a somewhat more ductile behaviour than the adhesive 'Betamate 73455', most likely due to the presence of the rubber particles.

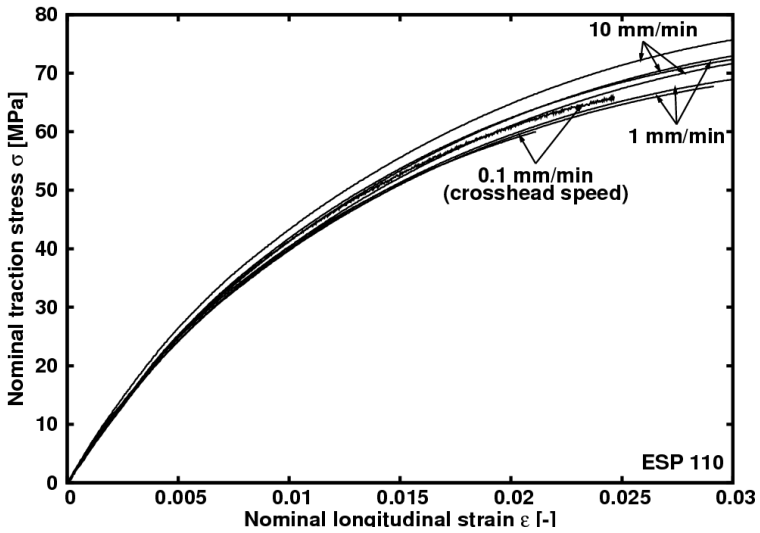

Figure 2.8: Experimental tensile stress versus strain curves for the adhesive 'ESP 110'

Wedge-peel tests

Three distinctly different specimen geometries, but with identical thicknesses for the two arms, were tested using the wedge-peel test. They correspond to three different combinations of adhesive layer, h_{adh}, and adherend thickness, h, respectively: (i) h_{adh} = 0.25 mm and h = 1.00 mm, (ii) h_{adh} = 0.25 mm and h = 1.45 mm, and (iii) h_{adh} = 0.40 mm and h = 1.45 mm.

The specimens were prepared from 200 mm x 20 mm aluminum-alloy strips cut from sheets of the appropriate thickness. The adhesive was then cured for 45 minutes at 150°C. Three specimens were tested for each geometry employing the set-up schematically presented in Figure 2.1(a). Fracture was always cohesive in the adhesive layer, but near one adhesive/adherend interface hence involving some degree of mode mixity though being still predominantly mode I. By convention, the side of the specimen close to which the crack propagated will be called the 'crack side', whereas the side on which most of the adhesive remains will be termed as the 'adhesive side'. The wedge thickness was equal to 1.50 mm and was inserted in the adhesive layer at an advancing rate of 7.5 mm/min. After testing, the residual radii of curvature of the arms were measured, on both sides of the adhesive layer, as an indicator of the overall energy expended in the test. These radii will be denoted by R_1 and R_2 on the adhesive and on the crack side, respectively, and were measured via photographic measurements.

The experimental results pertaining to the wedge-peel test are gathered in Table 2.3 and shown in Figure 2.9, and several noteworthy comments are to be made. The measured radii of curvature show a moderate to large variation from one specimen to the other for a given coupon geometry. Moreover, the larger the measured radius of curvature, then the larger the associated scatter; probably because the relative variation in the overall energy expenditure is smaller. Values of R_2 on the crack side are systematically smaller than on the adhesive side, R_1. As a reminder, the detached arm on the crack side is essentially made of the metallic adherend while, on the adhesive side, it is covered with most of the adhesive which increases its bending stiffness and explains the larger values of R_1. For an increasing adhesive layer thickness, the value of R_1 increases while both a and R_2 decrease. Assuming that the adhesive layer is fully plastic, an increase in h_{adh} makes the adhesive/adherend sandwich (i.e. on the adhesive side) more compliant at crack tip, in the direction normal to the crack plane. Therefore, a shorter crack length and, hence, a larger bending moment are needed to produce sufficient crack opening. This increased bending moment causes the value of R_2 on the crack side to drop while R_1 still increases because the gain, associated to the larger value of h_{adh}, in bending stiffness of the adhesive/adherend sandwich dominates. Finally, for an increasing adherend thickness, overall the flexural stiffness increases, so that the crack length can become longer to produce the same opening effect, and both radii of curvature increase.

Table 2.3: Experimental results obtained in the wedge-peel test for the adhesive 'ESP 110' with D_w = 1.5 mm

h_{adh} [mm]	h [mm]	a [mm]	R_1 [mm]	R_2 [mm]
0.25	1.00	5.4 $\pm$ 0.4	93.4 $^{+65.5}_{-26.6}$	16.0 $^{+0.9}_{-0.8}$
0.25	1.45	8.2 $\pm$ 0.6	119 $^{+11}_{-9}$	37.4 $^{+1.9}_{-1.7}$
0.40	1.45	7.7 $\pm$ 0.5	234 $^{+802}_{-98}$	30.8 $^{+1.7}_{-1.5}$

Table 2.4: Experimental results obtained in the fixed-arm peel test on specimens with h_{adh} = 0.40 mm and h = 1.00 mm

Peel angle [deg]	P/b [N/mm]	R_0 [mm]
45	16.7 $\pm$ 0.6	16.4 $\pm$ 0.7
90	6.05 $\pm$ 0.05	13.2 $\pm$ 0.29
135	4.11 $\pm$ 0.12	11.6 $\pm$ 0.22

(a)

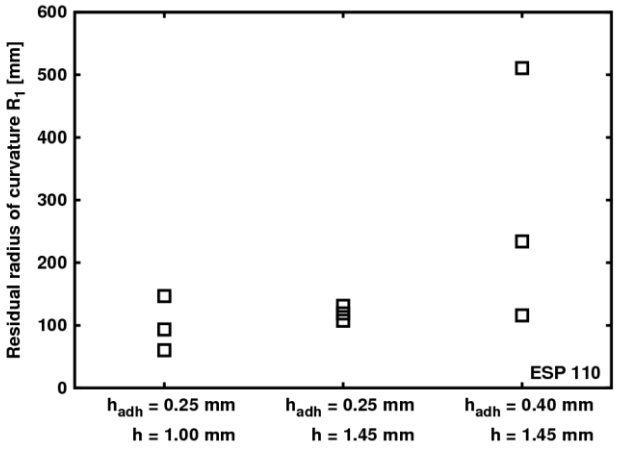

(b)

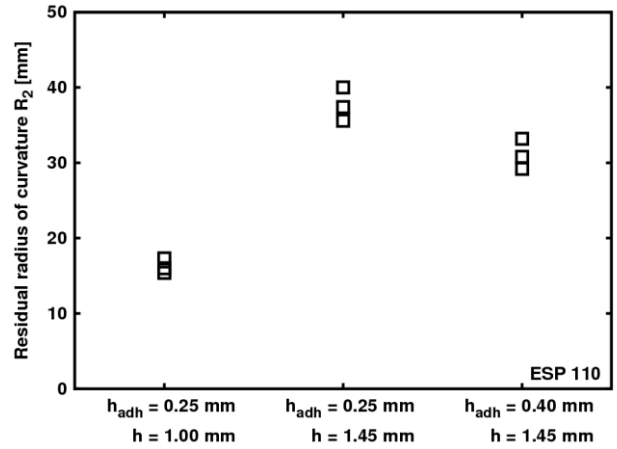

(c)

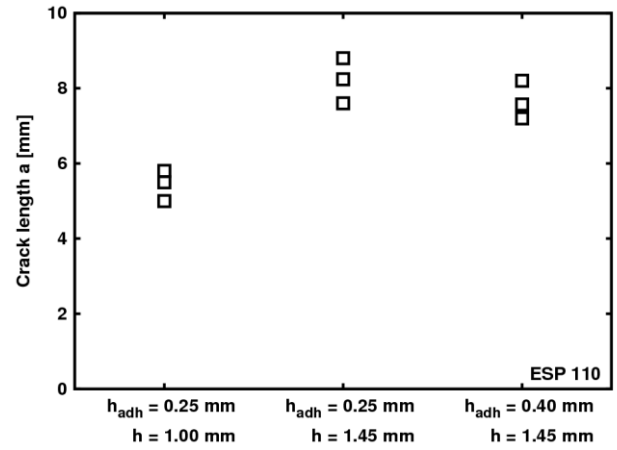

Figure 2.9: (a-b) Radii of curvature and (c) crack length obtained from the wedge-peel test for the adhesive 'ESP 110'

Fixed-arm peel tests

Fixed-arm peel tests have been performed during the course of a previous study (Kawashita et al., 2005). A single joint geometry is considered and it was manufactured using a 1.00 mm thick AA 5754-O 'flexible' adherend bonded to a 10.0 mm thick AA 5754-O 'rigid' substrate with a 0.40 mm thick layer of 'ESP 110' adhesive. The dimensions of the specimens were 220 mm x 20 mm. The adhesive was cured for 45 minutes at 150°C.

The fixed-arm peel test specimens were bolted through their base plate onto the experimental set-up shown in Figure 2.1(b) and tested using a crosshead speed of 5 mm/min at three different peel angles: 45, 90 and 135 degrees. For all specimens, failure was cohesive in the adhesive layer, but near the interface of the adhesive/flexible adherend, hence meaning, that though predominantly mode I, failure was showing some degree of mode mixity. The peel force versus time trace was recorded and an average, steady-state peel force per unit width, *P/b*, was deduced. The maximum curvature of the peel arm, $1/R_0$, was also numerically derived from digital photographs taken during the course of the test.

The fixed-arm peel test results are given in Table 2.4 and shown in Figure 2.10. They show that the maximum curvature of the flexible peeling arm increases with the peel angle, since the plastic bending becomes more intense. Nevertheless, the peel force decreases at the same time as the lever (i.e. peel) arm available for producing the bending moment increases.

Tapered double cantilever beam tests

TDCB test specimens prepared with different thicknesses of the adhesive layer and with aluminium-alloy arms (grade 2014A) showing a taper characterized by a value of m equal to 2 mm^{-1} were tested using a cross-head speed of 0.2 mm/min. The adhesive fracture energy was evaluated as for the adhesive 'Betamate 73455'. All specimens failed with the crack running close to the centreline of the adhesive layer, that is, in quasi pure mode I conditions. The results showed no significant 'R-curve' behaviour and the values of G_a were independent of the crack length for crack length values, a, between 70 and 230 mm. The corresponding steady-state values of the adhesive fracture energy are given in Table 2.5 and Figure 2.11. Table 2.5 shows that G_a values for this adhesive are about five times larger than for the adhesive 'Betamate 73445', most likely thanks to the rubber particles, and vary from 1000 to 1500 J/m² as the adhesive layer thickness, h_{adh}, is increased from 0.25 to 0.88 mm.

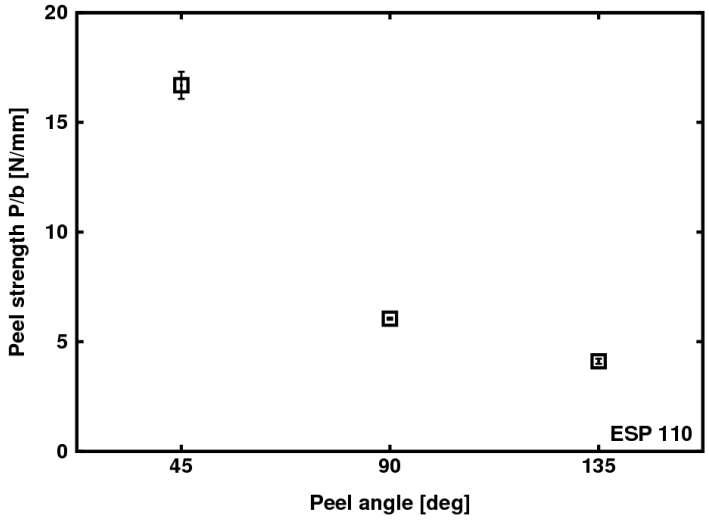

(a)

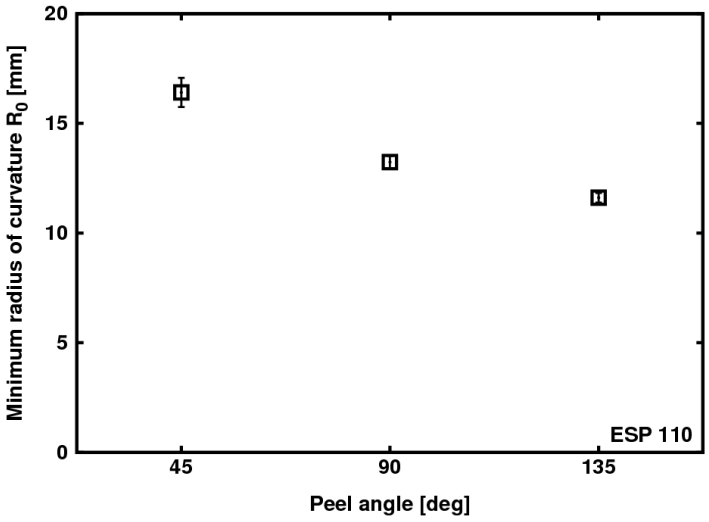

(b)

Figure 2.10: (a) Peel strength and (b) minimum radius of curvature obtained from the fixed-arm peel test for the adhesive 'ESP 110'

Table 2.5: Experimental LEFM TDCB test results for the adhesive 'ESP 110' (adherend: aluminium alloy; locus of failure: close to the centreline of the specimens)

h_{adh} [mm]	G_a [J/m^2]
0.25	1006 ± 165
0.32	988 ± 61
0.40	1168 ± 101
0.57	1409 ± 90
0.88	1483 ± 31

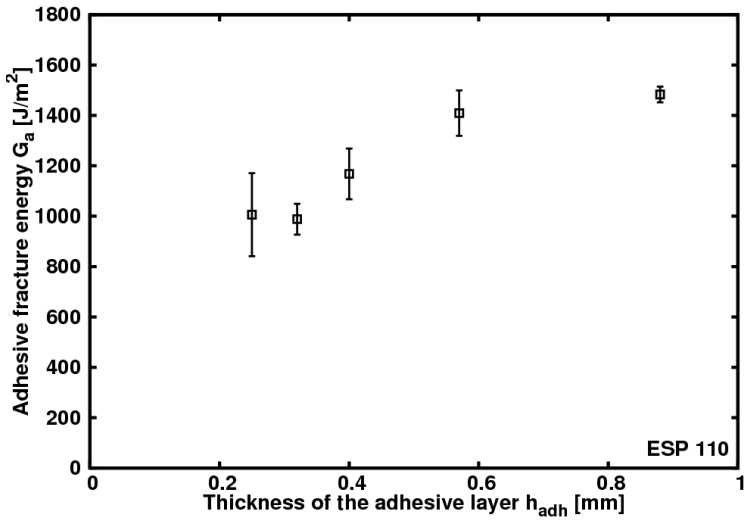

Figure 2.11: Adhesive fracture energy values measured from the TDCB test for the adhesive 'ESP 110'

Fracture surfaces

Figure 2.12 shows typical scanning electron micrographs of the fracture surface of the TDCB test specimens. It can be seen in Figure 2.12(b) that failure is accompanied by debonding of both the aluminium and the rubber particles which are of 30 to 100 µm in size, see Figure 2.12(b), and which are all separated by about 50 to 100 µm, see Figure 2.12(a).

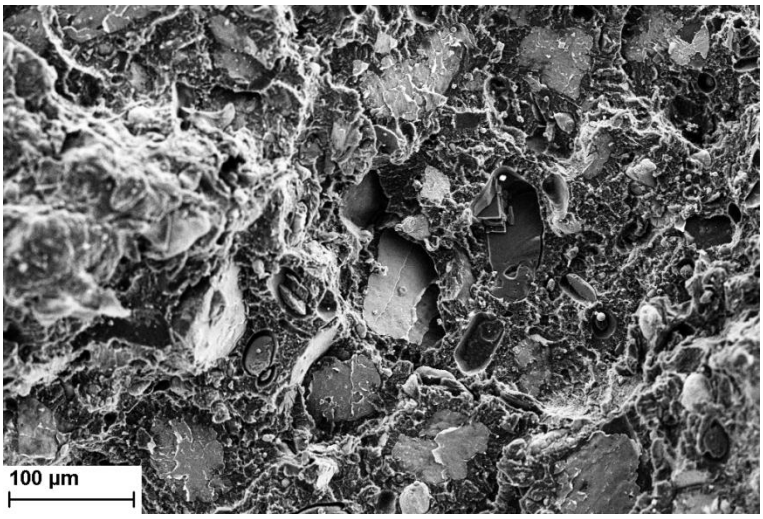

(a)

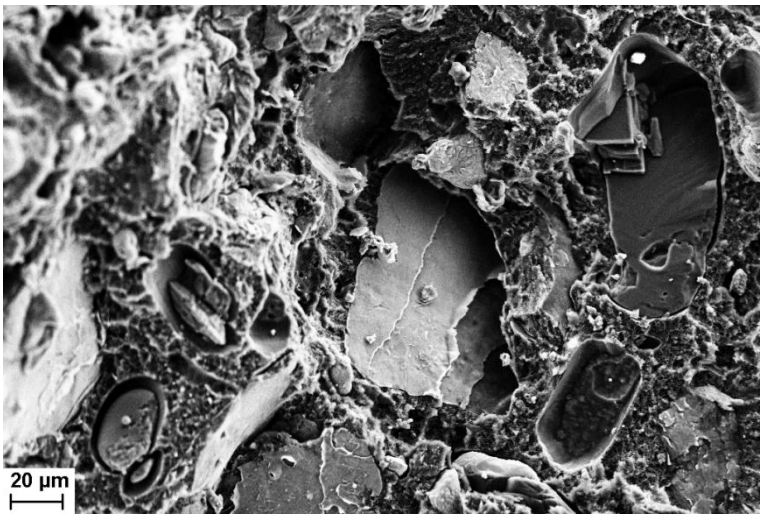

(b)

Figure 2.12: Typical fracture surface of the adhesive 'ESP 110' at two different magnification levels

2.3.4. Adhesive 'Betamate 1493'

Bulk tensile and compression tests

Flat dumbbell-shaped specimens made of bulk adhesive 'Betamate 1493' were tested in uniaxial tension by Ferracin (2003) at strain-rates from $2.5x10^{-5}$ to $2.5x10^{-3}$ s^{-1} and cylindrical specimens made of bulk adhesive 'Betamate 1493' were tested in uniaxial compression by Georgiou (2003) at a strain-rate of about 10^{-3} s. Figure 2.13 shows the corresponding stress-strain curves. It can be seen that, in tension, the adhesive exhibits significant rate-dependence, no hardening capacity and failure strains of the order of 5% and that, in compression, it exhibits a larger yield stress by a factor of approximately 1.35, some rehardening capability and a much larger failure strain of the order of 30%. These differences, commonly observed in polymeric materials (Raghava et al., 1973), can be attributed to the free volume required by the atomistic motions associated with yield being diminished by compressive stresses (Roylance, 1996). By comparison with Figure 2.8, the stress-strain curves in Figure 2.13 show that the adhesive 'Betamate 1493' possesses a lower modulus and exhibits a more ductile behaviour owing to the very limited amount of brittle or weakly bonded particles leading to early nucleation of small microcracks.

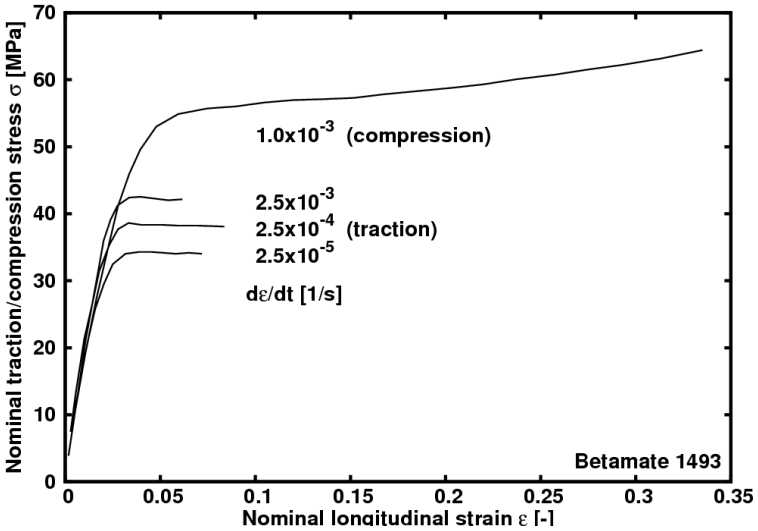

Figure 2.13: Experimental tensile and compression stress versus strain curves for the adhesive 'Betamate 1493'

Wedge-peel tests

Wedge-peel test specimens prepared with different thicknesses of the adhesive 'Betamate 1493' and with 1.2 mm-thick mild-steel arms (being the same grade as for the wedge-peel test specimens prepared with the adhesive 'Betamate 73455' in

Section 2.3.2) were tested by Ferracin (2003) with a 1.8 mm thick wedge advancing at a speed of 10 mm/min. The residual radius of curvature of both arms, R_1 and R_2, were measured on each specimen after being removed from the testing machine. Most of the specimens reported here failed under quasi pure mode I conditions, with the crack running at a short distance from the centreline of the adhesive layer. As a consequence, both radii were reasonably close to each other in value, and hence were combined together to give a single, average value R_a according to Equation (2.3). The resulting radii values are given in Table 2.6 and Figure 2.14 which show that the thicker the adhesive layer, the smaller the radius and, hence, the higher the adhesive fracture energy.

Table 2.6: Experimental EPFM wedge-peel test results for the adhesive 'Betamate 1493' (mild-steel adherend thickness, $h = 1.2$ mm; locus of failure: close to the centreline of the specimens)

h_{adh} [mm]	R_a [mm]
0.05	27.4 ± 1.5
0.18	18.4 ± 0.3

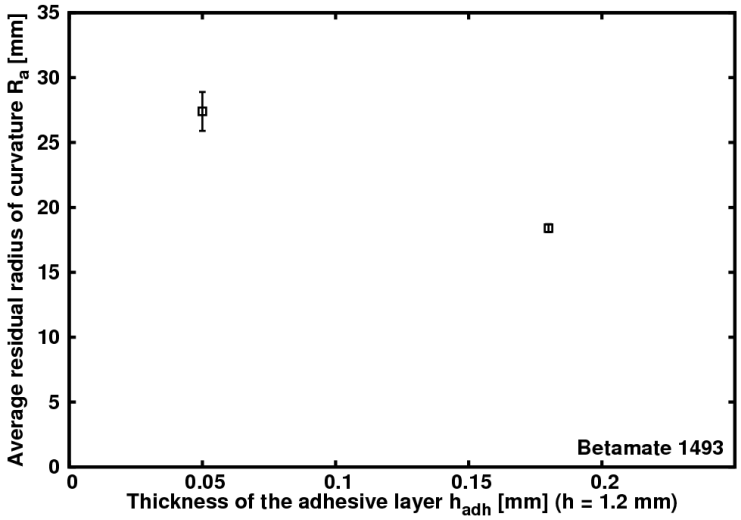

Figure 2.14: Average residual radius of curvature obtained from the wedge-peel test for the adhesive 'Betamate 1493'

Tapered double cantilever beam tests

TDCB test specimens prepared with different thicknesses of the adhesive 'Betamate 1493' and with aluminium-alloy arms (grade 2014A) showing a taper characterised by a value of m equal to 2 mm^{-1} were tested by Ferracin (2003) and by Georgiou (2003) using a cross-head speed of 0.1 mm/min. The adhesive fracture energy was evaluated as for the adhesive 'Betamate 73455'. All the specimens failed with the crack running close to the centreline of the adhesive layer, that is, under quasi pure mode I conditions. The results showed no significant 'R-curve' behaviour and G_a values that were independent of the crack length for crack length values, a, between 90 and 180 mm. The corresponding steady-state values of the adhesive fracture energy are given in Table 2.7 and Figure 2.15 which show that the value of G_a is approximately three to six times larger than for the adhesive 'ESP 110' and increases from 3500 J/m² to 6500 J/m² as the thickness, h_{adh}, of the adhesive layer is increased from 0.25 to 0.6 mm. These higher toughness values are thought to originate from the small amount of particles triggering the nucleation of microcracks and to the extensive plastic dissipation allowed by the cavitation of the rubber particles.

Table 2.7: Experimental LEFM TDCB test results for the adhesive Betamate 1493 (adherend: aluminium alloy; locus of failure: close to the centreline of the specimens)

h_{adh} [mm]	G_a [J/m^2]	Reference
0.25	3665 ± 321	Georgiou (2003)
0.40	5037 ± 287	Georgiou (2003)
0.60	6250 ± 441	Georgiou (2003)
0.80	6100 ± 300	Ferracin (2003)

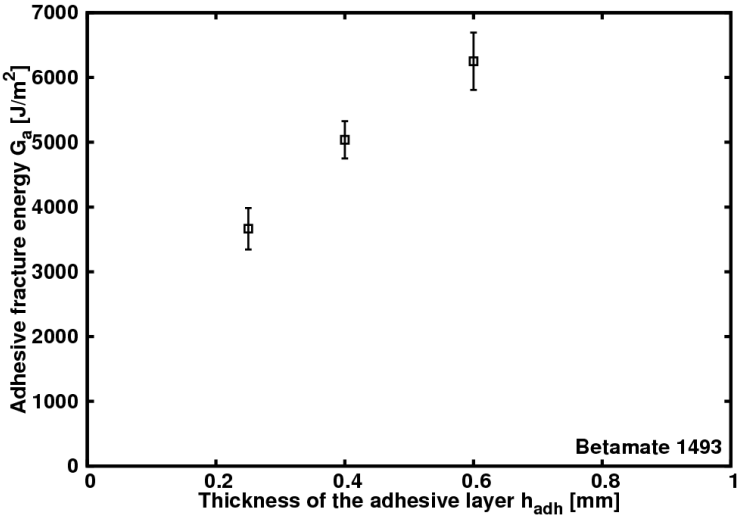

Figure 2.15: Adhesive fracture energy values measured from the TDCB test for the adhesive 'Betamate 1493'

Fracture surfaces

Figure 2.16, which was obtained by Ferracin (2003) shows typical scanning electron micrographs of the fracture surface of the TDCB test specimens. It can be seen in Figure 2.16(b) that secondary cracks initiate from debonded silica particles which are of less than 20 µm in size and grow radially, see Figure 2.16(a), over a distance of about 150-200 µm. Crack propagation thus seems to proceed by the succession of discrete events consisting of the debonding of second-phase particles immediately followed by the rapid, dynamic growth of crack patches over a finite distance before being arrested.

2.4. Summary

Three different epoxy-based adhesives are therefore being considered. As explained above, (i) they show different levels of ductility, (ii) their fracture surfaces are all associated with the debonding or cleavage of second-phase particles, and, (iii) they exhibit significantly different values of the adhesive fracture energy. As they all have different microstructures (e.g. type, size distribution and volume fraction of second-phase particles), it is considered that this aspect accounts for the differences observed in their macroscopic properties. In particular, it is to be expected that the resistance to cleavage or debonding of the second-phase particles, as well as their spacing and their tendency to promote plastic dissipation, will of course affect the value of the adhesive fracture energy of the adhesive.

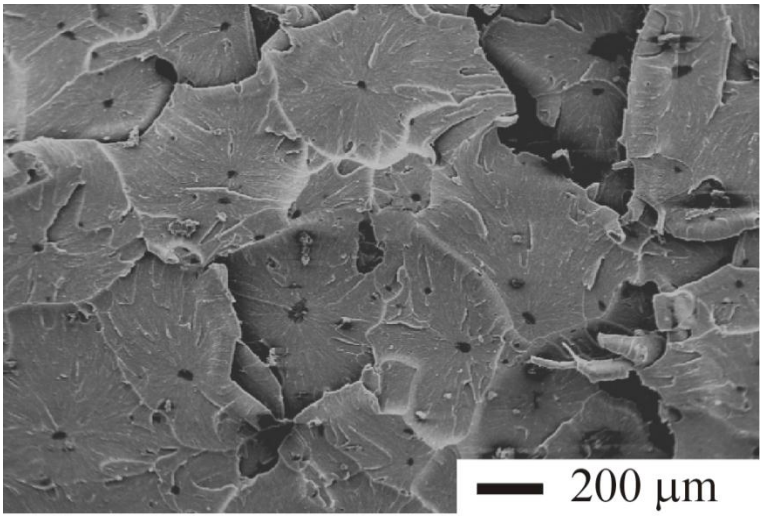

(a)

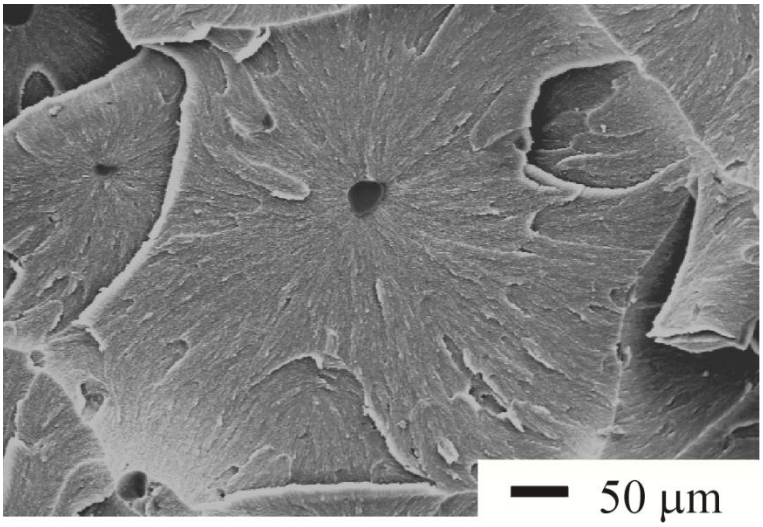

(b)

Figure 2.16: Typical fracture surface of the adhesive 'Betamate 1493' at two different magnification levels

Chapter 3
The AACZ model

3.1. Motivation behind the model

The goal that we set ourselves here is to develop a model capable of reproducing accurately the failure of adhesively-bonded joints with a limited number of material parameters and, with the help of such model, to conduct parametric studies with a view to gain a better understanding of the parameters affecting the adhesive fracture energy.

The idea behind the model that will be developed in this Chapter was first suggested by Needleman (1987) in the context of inclusion debonding in heterogeneous materials, and has been applied recently to cohesive failure in adhesive joints (Blackman et al., 2003b; Cooper et al., 2009; Pardoen et al., 2005; Salomonsson and Andersson, 2008; Tvergaard and Hutchinson, 1994). It consists in following a 'top-down approach' to fracture (Hutchinson and Evans, 2000): that is, both cohesive zone elements and continuum elements are used to represent the different phenomena taking place at different length scales in the adhesive as it fractures, which is the reason why this model will be referred to as the AACZ model (Adherend + Adhesive + Cohesive Zone). Besides, the cohesive zone properties will be kept constant in the model throughout all the modelling studies, even when the thickness of the adhesive layer will be modified. And, finally, the model that will be used here directly searches, in an iterative process, for the test-specimen configuration corresponding to the conditions of steady-state crack propagation.

These modelling choices are particularly well suited to performing the parametric study envisaged in the present thesis. Firstly, the model relies on a single set of material parameters, like other types of model in the literature (e.g. Chai and Chiang, 1998; Hadavinia et al., 2006), to reproduce accurately the failure of the adhesive for different types of test specimen and over a wide range of geometrical

configurations. This is in contrast to numerous solutions that can be found in the literature (e.g. Ferracin et al., 2003; Yang et al., 1999, 2000) that rely on material parameters that need to be re-identified experimentally or re-calculated numerically when, for example, the thickness of the adhesive layer is changed (Kafkalidis et al., 2000). Secondly, the proposed model gives a detailed description of the stress state in the adhesive, which is very useful for identifying a rationale for the trends that have been observed experimentally. Again, this is in contrast to some simplified models (e.g. Ferracin et al., 2003; Yang et al., 1999, 2000) which miss these details by replacing the actual adhesive layer by a single cohesive zone. Finally, the proposed model directly searches for the steady-state solution to the problem and, hence, is computationally efficient. This is very desirable when many geometrical configurations of different types of specimen need to be studied, as it is the case in the present study. Yet again, in contrast, transient-solution schemes (e.g. Cui et al., 2003; Hadavinia et al., 2006) only reach the steady-state solution after solving numerous intermediate time-steps, which are required in order to propagate the crack over a distance equal to several adhesive layers thicknesses before reaching the steady-state. This is a very time consuming process, since very small element sizes have to be used over the entire region of successive crack tip locations to properly represent the response of the fracture process zone whereas, in the steady-state formulation, such very small element sizes only have to be used at a single crack tip location since the latter does not move through the mesh. Wucher (2009) showed, by comparison with transient simulations performed with a commercial FE code, that significantly lower computational times could be achieved with a steady-state code. Wucher (2009) even showed that, in some cases, when imposing small element sizes over the full range of successive crack tip locations in the transient calculations, the total number of degrees of freedom was simply too large for the problem to run with a commercial FE code whereas the corresponding steady-state calculation succeeded in running in reasonable computational times, typically below 24 hours. It should be noted, as later addressed in Sections 3.3.3 and 3.3.4 below, that the improved computational efficiency of the steady-state formulation unfortunately comes with an increased complexity in the definition of suitable boundary conditions.

A somewhat similar model has been previously used to conduct parametric studies on the toughness of rate-independent materials (Tvergaard and Hutchinson, 1992), rate-dependent materials (Landis et al., 2000) and thin ductile layers joining semi-infinite elastic media (Tvergaard and Hutchinson, 1994). Also, the present model shares some common features with the one reported by Salomonsson and Andersson (2008), but in their work they set out to identify the cohesive zone model that would best represent the full adhesive layer. The present study aims to add significantly to the understanding gained in these previous studies by

considering the toughness of adhesive joints, i.e. by conducting a parametric study on the toughness of a polymeric layer (the adhesive), sandwiched between two elastic-plastic materials with finite dimensions (the adherends). Indeed, it completes the work that was initiated by Pardoen et al. (2005) by studying in depth, and explaining, the different local dissipation mechanisms that contribute to the value of the adhesive fracture energy via an analysis of the detailed stress and strain fields. The model used in the present work will assume that the energy associated with the fracture process zone, as described by the traction--separation law is a constant, and so independent of the stress state. This is indeed a major assumption that will be justified from the experimental validation undertaken, as well as being based on physical arguments related to the mechanisms of damage and failure that occur; and which follow from the relatively low toughness of the adhesive employed in the present work.

3.2. Fundamentals of the model

A typical adhesive joint with a pre-existing crack is shown schematically in Figure 3.1(a). When it is loaded, damage mechanisms such as particle cleavage, particle debonding, cavitation, shear yielding, etc. take place in a region ahead of the crack tip, which irreversibly affect the integrity of the material. Depending on the adhesive system, the damage zone may remain very small, or spread over a relatively large region. The model assumes the existence of a localised damage and deformation region immediately ahead of the crack tip called the 'fracture process zone', and the crack then propagates with such a zone immediately preceding the crack. As shown in Figure 3.1(b), this intrinsic 'fracture process zone' is represented by a traction versus separation condition across the crack plane, i.e. a cohesive zone model (CZM) is employed. The surrounding material is considered as a continuous medium and, thus, the intrinsic damage mechanisms are extracted from the continuum medium and condensed onto a plane with zero thickness. The adhesive fracture energy, G_a, is therefore evaluated in the model, see Figure 3.1(b), as the sum of the energy, Γ_0, required to break the cohesive elements and of the total energy expended in the bulk of the adhesive layer, Γ_b, i.e. by inelastic deformations such as viscoplastic-energy dissipation or by locked-in elastic strain-energy. As suggested by Pardoen et al. (2005), it is further assumed that the cohesive zone response is independent upon the stress-state existing in the near crack-tip region. Thus, the material parameters defined for the CZM, i.e. the peak stress, $\hat{\sigma}$, and intrinsic fracture energy, Γ_0, are considered to be material constants for a given adhesive. Therefore, any dependence of the adhesive fracture energy, G_a, upon the adhesive layer thickness, for example, can only enter through changes in the energy expended in the bulk of the adhesive layer, Γ_b. As indicated above,

the assumption of using a constant value for Γ_0, which is independent of the constraint, will be discussed later in the text.

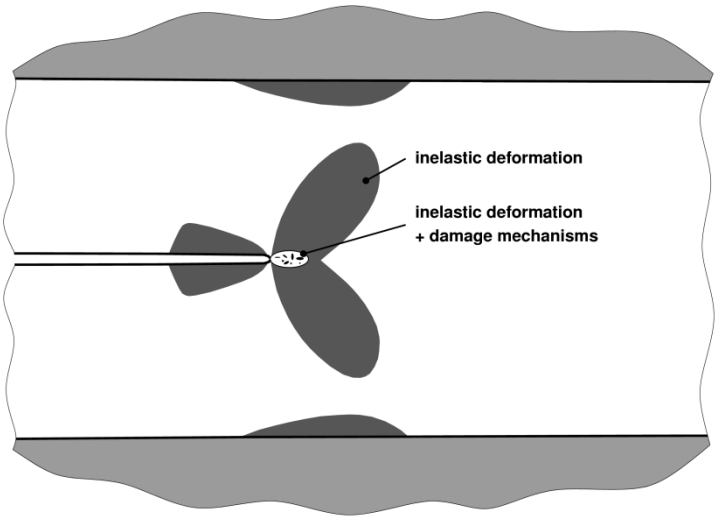

(a)

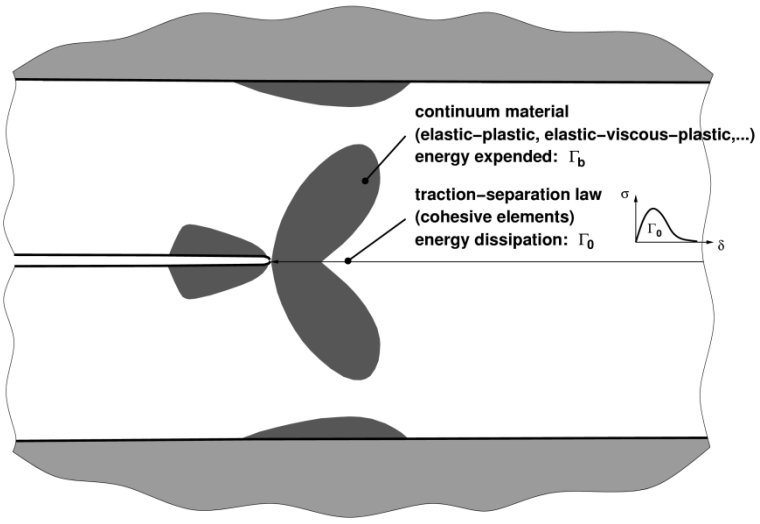

(b)

Figure 3.1: A schematic representation of (a) the phenomena associated with the fracture of an adhesive layer, and (b) the corresponding model. (Dark shaded areas represent inelastic deformation in the adhesive layer.)

3.3. Implementation

The above modelling approach was implemented via a large-rotation, 2D plane-strain, steady-state, FEM formulation. The need for large rotations comes from the fact that, in most peel tests, including the wedge-peel test specimen, the arms of the specimen can bend appreciably, hence moving away and rotating from their original positions. The 2D, plane-strain and steady-state assumptions stem from concerns of computational efficiency, related to the very small mesh sizes needed to resolve properly the stresses in the fracture process zone. As a reminder, Wucher (2009) showed, by comparison with transient simulations performed with a commercial FE code, that significant speed-ups and more accurate calculations could be achieved with the help of such a steady-state formulation.

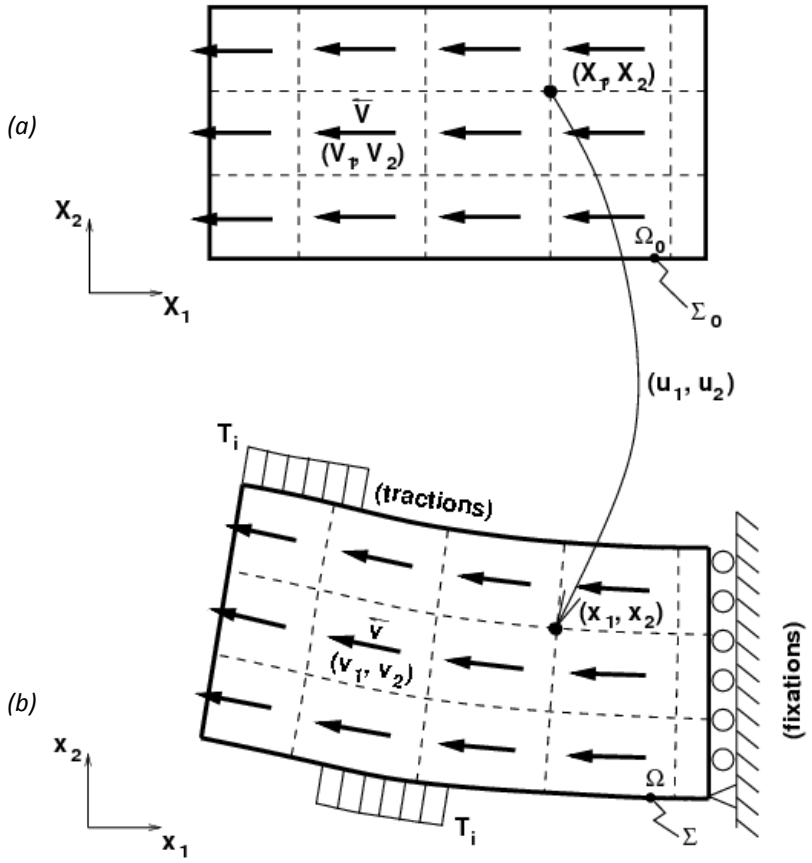

Figure 3.2: The definition of the (a) undeformed, and (b) deformed configurations and associated quantities involved in the steady-state formulation.

3.3.1. The steady-state finite-element model formulation

The present steady-state FEM formulation is an extension to the approach initially proposed by Dean and Hutchinson (1980). Consider the 2D domain depicted in Figure 3.2(a), which spans a volume Ω_0 enclosed by a surface Σ_0. In the steady-state regime, and in the absence of any loads or deformation, solid material is flowing through, free of any stress, from the right-hand to the left-hand side, with a uniform and constant material velocity given by:

$$\begin{cases} V_1 = -\dot{a} \\ V_2 = 0 \end{cases} \tag{3.1}$$

where $\dot{a}$ is a constant and corresponds to the crack velocity. This configuration is the 'reference configuration, Ω_0,' in which any given spatial point is located through a pair of coordinates (X_1, X_2). Next consider that different fixed points and loadings are applied to Σ_0, and held constant over time. Upon completion of a transient phase, a new steady-state configuration, i.e. the 'deformed configuration, Ω,' is reached, as shown in Figure 3.2(b). In this configuration, any given spatial point is now located through a pair of coordinates (x_1, x_2) and the material is flowing through a different volume, Ω, with a material velocity given by:

$$v_i = \frac{\partial x_i}{\partial X_j} V_j \quad (i = 1,2) \tag{3.2}$$

Indeed, referring to a given material particle by its location (ξ_1, ξ_2) in the reference configuration at time $t = 0$:

$$\xi_i = X_i(\xi_i, t = 0) \quad (i = 1,2) \tag{3.3}$$

the material velocity is defined as:

$$v_i = \lim_{\Delta t \to 0} \frac{x_i(X_i(\xi_i, t+\Delta t)) - x_i(X_i(\xi_i, t))}{\Delta t} \quad (i = 1,2) \tag{3.4}$$

since, under the present steady-state conditions, the position (x_1, x_2) of any given spatial point (x_1, x_2) in the deformed configuration is only a function of the position (X_1, X_2) of the same spatial point in the reference configuration. As a consequence, Equation (3.4) can further be rewritten as:

$$v_i = \frac{\partial x_i}{\partial X_j} \lim_{\Delta t \to 0} \frac{X_j(\xi_i, t+\Delta t) - X_j(\xi_i)}{\Delta t} \quad (i = 1,2) \tag{3.5}$$

where the limit term on the right hand side is precisely the velocity field (V_1, V_2) defined in Equation (3.1) in the reference configuration (X_1, X_2) so that Equation (3.2) is recovered.

The deformed configuration, Ω, is unequivocally defined by the displacement field, (u_1, u_2), which maps the position of any point in the reference configuration, Ω_0, to the corresponding position in the deformed configuration, Ω:

$$x_i = X_i + u_i \quad (i = 1,2) \tag{3.6}$$

The deformed configuration can be found by solving the equations of equilibrium. Therefore, the reference configuration is discretised using finite elements and the displacement field is approximated, via shape functions, from the displacement values at the nodes of the resulting mesh, which become the unknowns of the problem. The latter are then found by solving the weak form of the equilibrium conditions which, in the absence of inertial effects and volume forces, may be stated as:

$$\int_{\Omega_0} S_{ij} \delta E_{ij} \, d\Omega = \int_{\Sigma_0} T_i \delta u_i \, d\Sigma \tag{3.7}$$

where T_i are the tractions acting on Σ_0, and E_{ij} and S_{ij}, respectively, denote the Green-Lagrange strain-tensor and the second-order Piola-Kirchhoff stress-tensor, respectively. (This particular choice of the strain and stress makes it possible to account for large rotations, whilst integrating the equilibrium equations of the unknown deformed configuration over the undeformed configuration which is known *a priori*.) The Green-Lagrange strains in Equation (3.7) are defined under 2D plane-strain conditions as:

$$E_{ij} = \left(\frac{\partial u_i}{\partial X_j} + \frac{\partial u_j}{\partial X_i} + \frac{\partial u_k}{\partial X_i} \frac{\partial u_k}{\partial X_j} \right) \quad (i, j = 1,2,3) \tag{3.8}$$

with $u_3 = 0$ and, hence, $E_{13} = E_{23} = E_{33} = 0$ under 2D plane-strain conditions. The second Piola-Kirchhoff stresses in Equation (3.7) depend upon the strain history seen by the material particles according to a material law of the form:

$$\frac{DS_{ij}}{Dt} = f\left(E_{ij}, \frac{DE_{ij}}{Dt}, \phi_m \right) \quad (i, j = 1,2,3) \tag{3.9}$$

where ϕ_m are the state variables and D/Dt denotes the material derivation:

$$\frac{D}{Dt} = \frac{\partial}{\partial t} + V_k \frac{\partial}{\partial X_k} \tag{3.10}$$

Under steady-state conditions, the partial derivative with respect to time in Equation (3.10) vanishes, so that Equation (3.9) becomes:

$$V_k \frac{\partial S_{ij}}{\partial X_k} = f\left(E_{ij}, V_k \frac{\partial E_{ij}}{\partial X_k}, \phi_m\right) \tag{3.11}$$

or, by making use of Equation (3.1):

$$-\dot{a} \frac{\partial S_{ij}}{\partial X_1} = f\left(E_{ij}, -\dot{a} \frac{\partial E_{ij}}{\partial X_1}, \phi_m\right) \tag{3.12}$$

The Piola-Kirchhoff stresses in Equation (3.7) can thus be evaluated by integrating Equation (3.12), in the undeformed configuration, over lines with constant X_2, i.e. streamlines, from the right boundary of the domain, corresponding to $X_1 = X_1^r$, down to the X_1 coordinate of interest:

$$\begin{aligned} S_{ij}(X_1, X_2) = \quad & S_{ij}(X_1^r, X_2) \\ & -\frac{1}{\dot{a}} \int_{X_1^r}^{X_1} f\left(E_{ij}, -\dot{a} \frac{\partial E_{ij}}{\partial X_1}, \phi_m\right) dX_1 \end{aligned} \tag{3.13}$$

Equation (3.8) is non-linear in the displacement field and the function $f\left(E_{ij}, -\dot{a} \frac{\partial E_{ij}}{\partial X_1}, \phi_m\right)$ appearing in Equation (3.13) is non-linear in the presence of plasticity, so that the equation of equilibrium, Equation (3.7), needs to be solved numerically. A Newton procedure, similar to that outlined by Dean and Hutchinson (1980), is followed. Also, the integrals appearing in Equations (3.7) and (3.13) must be evaluated numerically. This is achieved for Equation (3.7) through Gauss integration, whilst the integral in Equation (3.13) is evaluated by a backward-Euler scheme. This is possible by using structured meshes only, as shown in Figure 3.2(a), so that the Gauss points are aligned on lines with constant X_2 values. The FEM solution is an approximation to the exact solution of the equilibrium equations. A mesh-convergence analysis is conducted for each analysis to ensure that the FEM solution, and the derived numerical results, are sufficiently close to the exact solution. This is achieved by decreasing the size of the elements successively until no significant change is observed in the numerical results.

3.3.2. The CZM formulation

The above FEM is supplemented with a CZM to simulate the behaviour of the intrinsic fracture process zone. Considering Figure 3.3(a), the crack is extended ahead of the actual crack tip and prevented from opening freely in that region by the cohesive forces acting in opposite directions on each of the crack faces. The forces per unit of crack area, T_n and T_t, acting in the directions normal and tangential to the crack faces depend upon the corresponding crack-opening

displacements, δ_n and δ_t, according to a particular traction versus separation relationship (e.g. see Figure 3.3(b)).

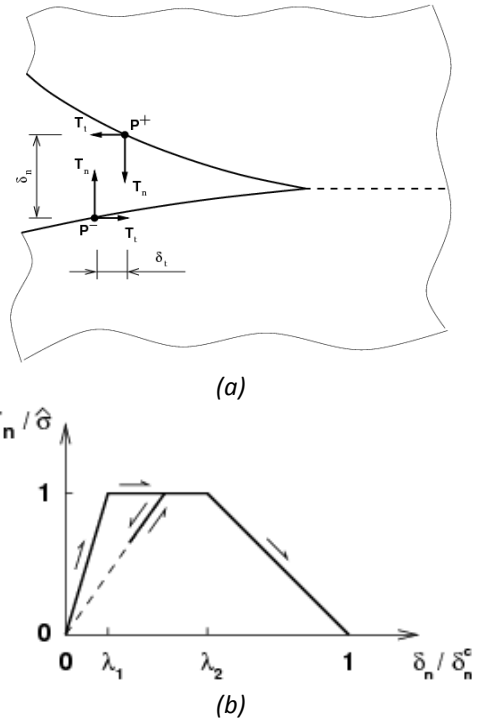

Figure 3.3: (a) The definition of the quantities related to the cohesive elements, and (b) a schematic of the traction versus separation law.

The present model deals with cases where mode I is the predominant mode of fracture. Hence, the opening displacement in the tangential direction, δ_t, will be assumed to evolve free of any tangential force, i.e. $T_t = 0$. The only relationship that, therefore, needs to be made explicit is the dependence of the normal traction upon the normal opening displacement: $T_n = T_n(\delta_n)$. From Needleman (1987), the traction T_n is assumed to respond linearly to the opening displacement δ_n with a modulus E_n that progressively degrades as a damage parameter, d, evolves from a value of 0, in the initial, undamaged state, to a value of 1 at complete failure, when the traction drops to zero and the actual crack propagates. Thus:

$$T_n = E_n(d)\delta_n \tag{3.14}$$

The main feature of this approach is that the tractions linearly return to zero when the opening displacement decreases as shown in Figure 3.3(b). Following the work

of Tvergaard (1990), the damage parameter, d, in Equation (3.14) is evaluated as a function of time, t , so that:

$$d(t) = \max_{t' < t} \frac{\delta_n(t')}{\delta_n^c} \tag{3.15}$$

where δ_n^c is the critical opening displacement at which failure occurs and the variation of the modulus E_n, appearing in Equation (3.14), as a function of the damage parameter, d, completely defines the behaviour of the cohesive elements.

It should be noted that it is crucial to give the cohesive zone elements that capability to unload elastically. Figure 3.4 shows for instance that significant differences can be seen in the numerical predictions if that capability is not offered. More importantly, it was not possible to reproduce some of the trends observed experimentally without that elastic unloading capability.

In addition to Equation (3.14), the 'virtual' crack faces ahead of the actual crack tip are prevented from interpenetrating by introducing inequalities of the form $\delta_n \leq 0$, implemented with the help of Lagrange multipliers, and added to the finite-element formulation. From a numerical point of view, the Lagrange multipliers substitute for the cohesive stresses, which are zero when $\delta_n = 0$, and locally compensate for the external loading until any interpenetration is removed.

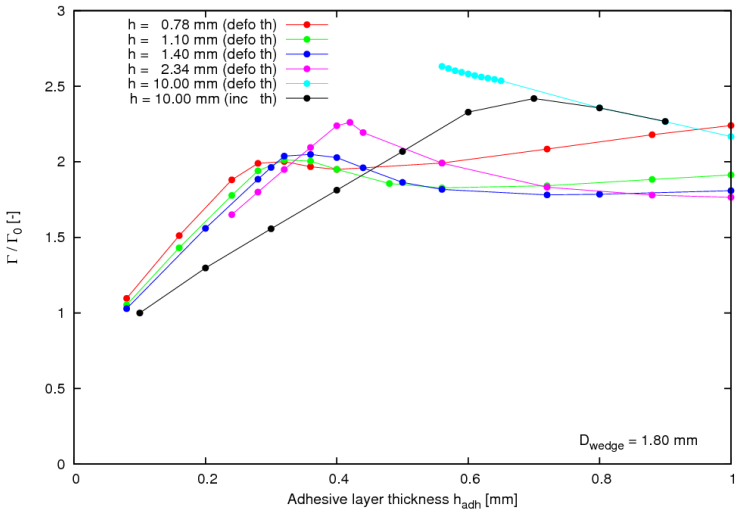

Figure 3.4: Illustration of the usefulness of using a damage-based cohesive zone formulation ("inc th" as opposed to "defo th" in the above plot)

3.3.3. The EPFM wedge-peel test specimen

A schematic representation of the wedge-peel test specimen is shown in Figure 3.5(a), along with the corresponding model in Figure 3.5(b). Well ahead of the crack tip, the specimen is not affected by the loading and remains undeformed. Far behind the wedge, it is completely unloaded and shows a uniform curvature. As a consequence, the model can be restricted to some distances, l_u and l_d, ahead of the crack tip and past the wedge, respectively. This necessitates the application of appropriate boundary conditions to substitute for the missing portions which turns out to be a complicated task and hence represents the main drawback of the steady-state formulation. The inlet section, see Figure 3.5(b), is clamped in order to impose zero deformation and to fix rigid-body modes at the same time. The outlet section, see Figure 3.5(b), should ideally be constrained so as to give a zero material derivative of the curvature. However, such conditions are difficult to formulate and to implement. It is much easier to extend the arms by a length $l_{d,ext}$ past the outlet section and let the resulting end section be free. If $l_{d,ext}$ is sufficiently large, then the outlet section is unaffected by the presence of the free end and behaves as if the arms were extending to infinity. In practice, lengths l_d and $l_{d,ext}$ are merged into a single value $l_{d,tot}$ that is increased until a significant portion of the arms past the wedge show a uniform curvature. The outlet section can then equally be placed in this portion. Similarly, the length l_u is increased until the computed crack tip opening displacement remains unchanged for a given crack length and wedge thickness. The choice of these lengths is part of the convergence study which is run for all the analyses.

For the sake of simplicity, the cohesive elements are placed either along the specimen centreline when simulating test configurations failing close to the centreline of the adhesive layer, i.e. under quasi pure mode I conditions, or along one of the adhesive/adherend interfaces when simulating test configurations failing close to one of these interfaces, i.e. under conditions showing some degree of mode mixity. Moreover, the extent of the cohesive elements is restricted to the region ahead of the crack tip, i.e. they span the length l_u. This significantly reduces the number of iterations in the solution procedure that would otherwise be required to break the cohesive elements. The disadvantage of this approach is that the crack length, a, is unknown *a priori*; and its value must be found iteratively by running multiple calculations with different values of a until the condition is satisfied that the opening displacement at the assumed crack tip is indeed equal to its critical value δ_n^c. The presence of the wedge, of thickness D_w, is taken into account by imposing the following multi-point constraint:

$$u_2^B - u_2^A = D_w \tag{3.16}$$

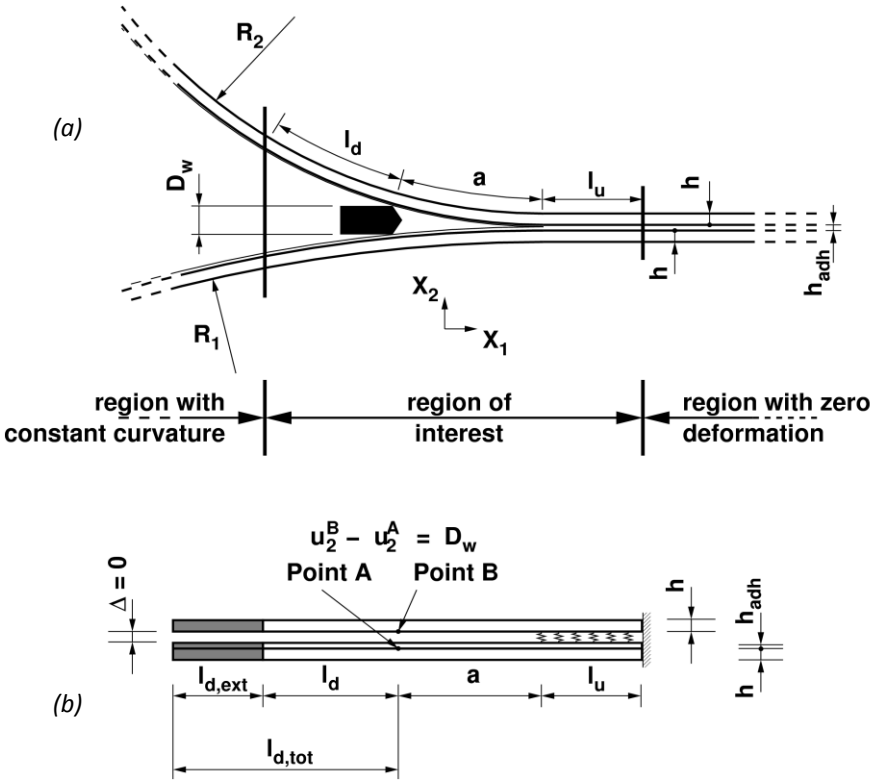

Figure 3.5: (a) A schematic representation of the wedge-peel test specimen, and, (b) corresponding boundary conditions used in the numerical-modelling studies.

where the vertical displacements u_2^A and u_2^B are taken, as an approximation, on the adhesive/adherend interfaces to avoid local strains developing in the adhesive. It should be noted that the axial component of the force imposed by the wedge, as well as the possible misalignment of points A and B in the deformed geometry, are also neglected. All of these simplifications are valid providing the thickness of the wedge, D_w, is small compared with the crack length, a. In the cases where the cohesive elements are inserted along the centreline of the specimen, only the upper half of the geometry needs to modelled due to symmetry, and the condition in Equation (3.16) becomes a simple displacement boundary condition:

$$u_2^B = \frac{1}{2} D_w \tag{3.17}$$

Figure 3.6 shows a typical mesh in the case of a symmetrical model of the wedge-peel test, in the deformed configuration, corresponding to the following specimen dimensions: $h_{adh} = 0.24$ mm and $h = 0.78$ mm.

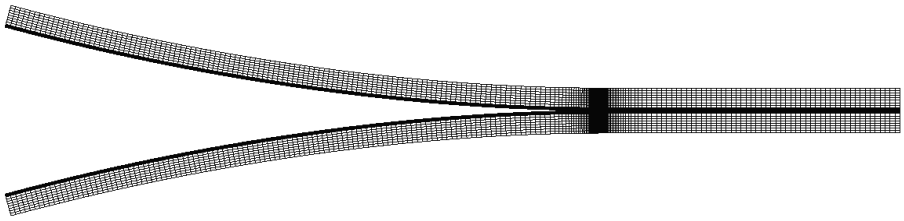

(a)

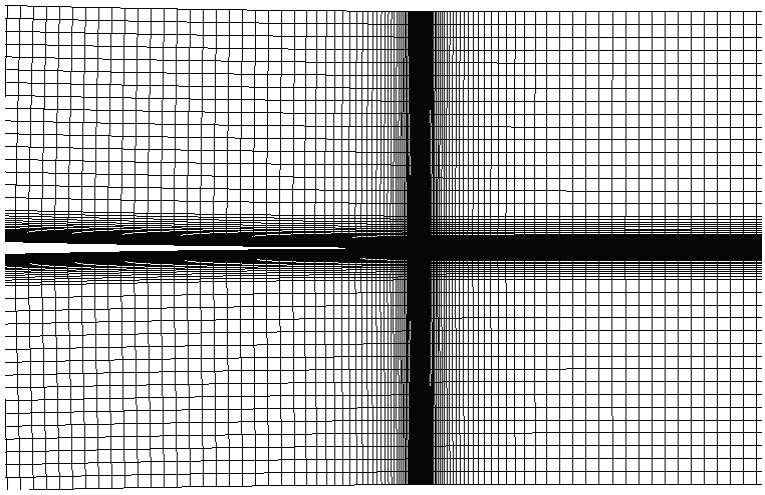

(b)

Figure 3.6: (a) A typical mesh which yields accurate results for a symmetrical model of the wedge-peel test specimen, and (b) a close-up view of the crack tip region. (For $h_{adh} = 0.24$ mm and $h = 0.78$ mm. In the case of a symmetric problem, only the upper half of the specimen is modelled.)

In order to capture the damage mechanisms at the crack tip, the mesh shows very fine elements in this region which are square in shape and 0.5 μm in dimension, i.e. about 1/500 times the thickness of the adhesive layer. When moving away from the crack tip, these elements are expanded, since such a fine size is no longer required. Hence, they become rectangular as their largest dimension is increasing by a geometrical progression factor of 1.1. Upon reaching the adherend, less local

phenomena need to be captured. Thus, their height reaches about 50 µm, which is 1/16 times the thickness of the arms and 100 times the size of the elements at crack tip, which still produces accurate results. In total, the mesh has approximately 120,000 nodes and 40,000 elements.

3.3.4. The EPFM fixed-arm peel test specimen

The geometry and boundary conditions used to simulate the fixed-arm peel test conditions are shown in Figure 3.7, and explained below. Since the rigid adherend is much thicker than the flexible adherend, and tightly fastened to the experimental set-up, it can reasonably be considered as being infinitely rigid. Therefore, it does not need to be modelled and can be substituted for by imposing zero displacements on the rigid adhesive/adherend interface. (Preliminary calculations confirmed that this assumption was reasonable.) Well ahead of the crack tip, the specimen is unaffected by the loading. Under steady-state conditions, the peel arm can be considered, to a first approximation, as being straight and parallel to the direction of the applied force over a finite length located somewhere in between the crack tip and the extremity of the peel arm. As the test proceeds further, this portion extends steadily towards the grips of the testing machine. Consequently, the model can be restricted to some distances, l_u and l_d, respectively ahead of, and past, the crack tip. To account for the segments that are discarded, the inlet section is clamped and the outlet section is tied to an external length of the arm, $l_{d,ext}$; which is introduced in the steady-state formulation and to which the external load is applied. To be rigorous, this length of the peel arm should be the true segment of the arm which makes the connection between the grips of the test machine and the zone of zero curvature, which consists of the initially unbonded segment of the peel arm supplemented with the length that was debonded before reaching steady-state conditions. However, since the complex distribution of plastic strains it encloses is unknown, it was replaced by the approximation of an elastic material free of any residual plastic strains. This illustrates once again the main drawback of the steady-state formulation, that is, the difficulty of imposing, in a simple way, appropriate boundary conditions at the frontier of the computational domain. In practice, lengths l_d and $l_{d,ext}$ are merged in a single value $l_{d,tot}$ that is chosen to be sufficiently long to obtain converged results. The boundary of the domain of interest is then interrogated in this range so as to provide an average material velocity aligned with the direction of the applied force. The procedure for determining the length l_u is similar to that employed in the model of the wedge-peel test. Also, as for the model of the wedge-peel test, the cohesive elements are introduced only over a length l_u and at the adhesive/adherend interface since all the specimens tested experimentally failed with some contribution of mode II, with the crack running in the adhesive but near one of the adhesive/adherend interfaces.

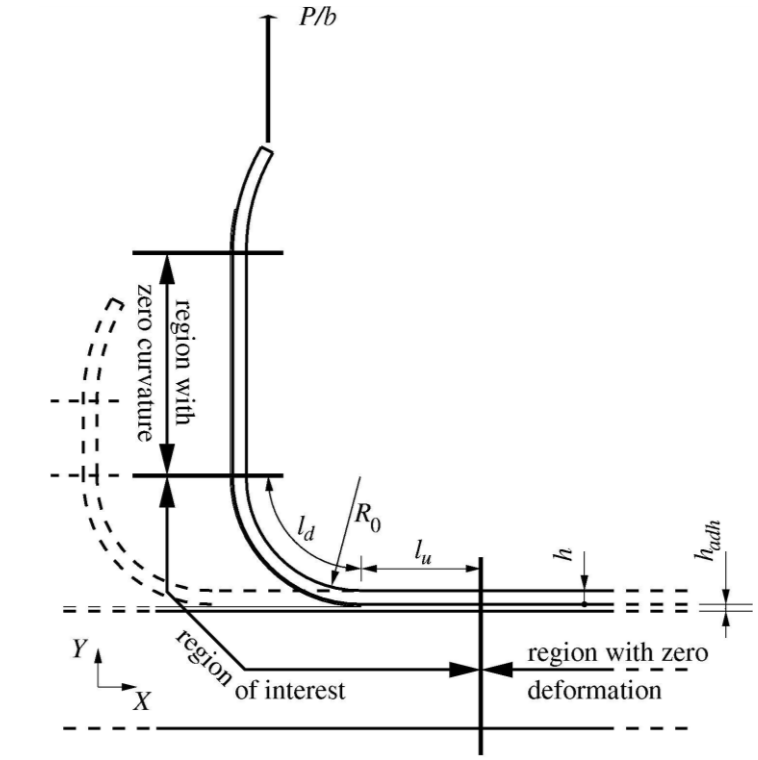

(a)

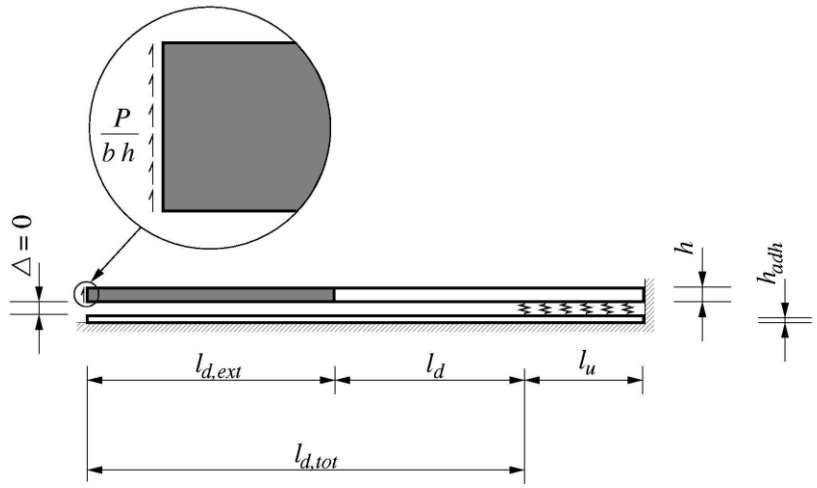

(b)

Figure 3.7: (a) Schematic representation of the fixed-arm peel test conditions and (b) corresponding boundary conditions used in the model

3.3.5. The LEFM TDCB test specimen

As may be seen in Figure 2.2, the height of the beam is not constant along a TDCB test specimen. As a consequence, the geometry of the full specimen cannot be reproduced within the present steady-state formalism. However, upon focusing on the crack tip region in the adhesive material, where the fracture process and energy dissipation mechanisms take place, steady-state conditions do prevail, since both the measured rate of crack propagation and the adhesive fracture energy, G_a, reach a plateau value. Therefore, the TDCB test is modelled using an equivalent steady-state model of the wedge-peel test characterised by the same adherend material and by values for the thicknesses of the wedge and adherend such that Equation (2.1), which normally applies to TDCB test specimens, still holds for a value of a equal to 200 mm, which was arbitrarily chosen to be in the range of values seen in actual TDCB tests. In practice, starting from an initial estimated value for the thickness of the arms, the wedge thickness is modified iteratively until the conditions for crack propagation are met with a crack length imposed equal to 200 mm. The left- and right-hand sides of Equation (2.1), are then evaluated and compared with each other. If they are equal to each other, the equivalent geometry has been found. Otherwise, the thickness of the arms needs to be modified, and the whole procedure repeated iteratively until Equation (2.1) is fulfilled. The motivation behind the definition of the equivalent wedge-peel test specimen is that, by reproducing the same relationship between applied force and adhesive fracture energy, namely Equation (2.1), as in the TDCB test specimen a similar stress-state is developed at the crack tip. This approach was validated against transient numerical simulations performed with the actual geometry of the TDCB test specimens (Wucher, 2009) which demonstrated that the effect of the particular choice of the arbitrarily-chosen crack length value was not significant.

3.3.6. Computing the adhesive fracture energy, G_a

The value of the adhesive fracture energy, G_a, is evaluated numerically from the model, see Figure 3.1(b), as the sum of the energy required to open the cohesive elements completely, Γ_0, and of the work expended (per unit area of crack advance) in the bulk of the adhesive layer, Γ_b[4], i.e.:

$$G_a = \Gamma_0 + \Gamma_b \tag{3.18}$$

[4] The notation departs from that used in Martiny et al. (2008). Γ_b is the total energy dissipated in the bulk of the adhesive layer, formerly denoted by Γ_p Martiny et al. (2008); and now Γ_p is limited to the plastic-energy dissipation only, in the bulk of the adhesive layer.

The value of Γ_0, referred to as the 'intrinsic work of fracture', is equal to the area under the traction versus separation curve. For the particular shape depicted in Figure 3.3(b), it is given by:

$$\Gamma_0 = \frac{1}{2}\delta_n^c \hat{\sigma}(1 - \lambda_1 + \lambda_2) \tag{3.19}$$

The value of Γ_0 is constant in the present CZM throughout all the modelling studies, since both δ_n^c and $\hat{\sigma}$ are kept constant. However, the work expended per unit area of crack advance in the bulk of the adhesive layer, Γ_b, may depend upon the stress-state prevailing in the adhesive and, hence, upon both the test specimen geometry and the test configuration. It is computed, under steady-state conditions, by integrating the material derivative of the strain energy density, W, over the adhesive layer and by dividing it by the material velocity:

$$\begin{aligned} \Gamma_b &= \frac{1}{\dot{a}} \int_{\Omega_{adh}} \frac{DW}{Dt} d\Omega_{adh} \\ &= \frac{1}{\dot{a}} \int_{\Omega_{adh}} S_{ij} \frac{DE_{ij}}{Dt} d\Omega_{adh} \end{aligned} \tag{3.20}$$

which, with Equations (3.1) and (3.10), becomes:

$$\Gamma_b = -\int_{\Omega_{adh}} S_{ij} \frac{\partial E_{ij}}{\partial X_1} d\Omega_{adh} \tag{3.21}$$

When using structured meshes, as shown in Figure 3.2(a), the value of $\partial E_{ij}/\partial X_1$ in Equation (3.21) can readily be approximated as $\Delta E_{ij}/\Delta X_1$, where ΔE_{ij} is the difference between the values of E_{ij} at successive integration points and ΔX_1 is the distance separating the latter. The value of Γ_b can be further split into two terms, i.e. the locked-in elastic strain-energy, Γ_e, and the plastic-energy dissipation, Γ_p:

$$\Gamma_b = \Gamma_e + \Gamma_p \tag{3.22}$$

So that Equation (3.18) now becomes:

$$G_a = \Gamma_0 + \Gamma_e + \Gamma_p \tag{3.23}$$

The elastic-energy locked-in the adhesive layer, Γ_e, results from non-uniform plastic deformation in the joint and is directly associated to the residual stresses, see the appendix in Wei and Hutchinson (1997). It may be readily evaluated, see Equation (3.22), by subtracting the plastic-energy dissipation from Γ_b. The plastic-energy dissipation, Γ_p, is ascertained by limiting the energy increments in Equation (3.21) to only the contributions from the plastic strains, $\mathrm{E}_{\mathrm{ij}}^{\mathrm{p}}$:

$$\Gamma_p = -\int_{\Omega_{adh}} S_{ij} \frac{\partial E_{ij}^p}{\partial X_1} d\Omega_{adh} \tag{3.24}$$

The term Γ_p can be broken further down, as detailed in Section 3.4.3.2, into contributions from the distinct deformation mechanisms, i.e. $\Gamma_p = \sum_i \Gamma_p^i$.

3.3.7. Programming

All the models presented in this thesis were programmed in Fortran starting from a code that was first developed by Landis et al. (2000) and later modified by Bertholet (2006). That code was capable of simulating the quasi-static steady-state failure of symmetrical test specimens made of a stack of exactly three different materials above the crack plane under the assumption of large deformation. These materials could be either elastic-plastic or elastic-viscous plastic. The failure process was represented by a cohesive zone law, with the shape depicted in Figure 3.3(b) but without the capability of elastic unloading, which was implemented as a boundary condition acting on the plane of symmetry. The meshes and the material properties were read from input text files that needed to be written either manually or with a separate Fortran code. The stiffness matrix of the finite element problem was stored in the so-called 'skyline' format and the system of linearized equations was solved with an LU factorization algorithm. There were barely any dedicated post-processing tools available.

A lot of programming work has been carried out as part of the thesis to implement the different models that were developed but also to make of this code a reliable platform open to new developments. Below is a list of the main developments that were made.

Programming environment

- A user's manual of the initial code was written.
- The source code was stored in a CVS repository making it possible (i) to track the history of all the changes that were made, and, (ii) for multiple developers to work simultaneously on the code.
- A set of test cases was created and regularly enriched. Scripts making it possible to run these test cases automatically were also written. This allowed checking regularly whether bugs were introduced in the program or whether the accuracy and the efficiency of the models were not degraded by the latest developments.

Core of the program

- The possibility of working with any number of materials in the same problem was added.
- The material behaviour laws, the cohesive zone laws, the storage and the inversion of the stiffness matrix were encapsulated in separate subroutines and fitted with generic interfaces making it possible to program easily new laws, a new matrix storage or to link with external solvers or material subroutines.
- The capability to run a small-perturbation calculation was added.
- Cohesive zone elements were implemented so that non-symmetric cracked configurations could be modelled. The elements were implemented in the large deformation context, fitted with load-carrying capabilities both in tension and in shear and given the capability to unload elastically.
- The possibility to make a calculation without a cohesive zone by tightening matching nodes across the crack plane ahead of the crack tip was added.
- The possibility to impose multi-point constraints (i.e. linear constraints with constant coefficients between an arbitrary number of degrees of freedom) was added and implemented both with Lagrange multipliers and through the elimination of degrees of freedom. These multi-point constraints were needed, for example, to tighten the matching nodes across the crack plane ahead of the crack tip when no cohesive zone was used.

Material laws

- The capability to use as material law an Abaqus UMAT was added to make it possible to benefit from UMATs developed elsewhere.
- New hardening laws, were implemented.
- New cohesive zone laws were implemented. This was done to test the effects of using a different shape.
- Failure criteria based on critical stresses or critical void volume fractions calculated from the Rice and Tracey equation were implemented.

Solution procedure

- The code was linked with the PARDISO solver which relies on a sparse matrix storage (CSR) and which can run in parallel. This greatly improved the computational efficiency of the code.
- A modified Newton-Raphson scheme and smarter convergence criteria were implemented which also improved the computational efficiency of the code.

- The possibility to restart an analysis from a previously saved solution was added.

Pre- and post-processing

- Dedicated user interfaces, through text files, were implemented to give the user the possibility to run very easily wedge-peel, fixed-arm peel or TDCB test simulations by only giving the physical parameters defining the problem, plus some parameters commanding the level of mesh refinement.
- Tools calculating automatically the energy expended in each material layer, the nodal forces, the J-integral, the residual radii of curvature, etc. were implemented.
- The output of different contour plots (stress, displacements, zones of active plasticity, triaxiality, etc.) in a format readable by the open-source viewer Gmsh was implemented.
- The output of a binary file with the minimum amount of information necessary to reconstruct a full solution was implemented to reduce the space needed to store all the results obtained in the thesis.

3.4. Application to the adhesive 'Betamate 73455'

In this Section, the above model is applied to a first adhesive, namely 'Betamate 73455'. More particularly, Section 3.4.1 describes how the values of the different material parameters needed for the modelling studies were obtained. In Section 3.4.2, the numerical predictions are compared with the experimental data to assess the validity of the model. In Section 3.4.3, the different dissipation mechanisms contributing to the adhesive fracture energy, G_a, are identified, explained and quantified. These results are then employed in Sections 3.4.4 and 3.4.5 to describe the variation of G_a as a function of a very wide range of test configurations for both the LEFM TDCB and EPFM wedge-peel test specimens. Finally, Section 3.4.6 compares the fracture behaviour of these two types of test specimen and their various test configurations, and comments on the relevance of our findings to (a) experimental results to be found in the literature, and (b) the basic meaning of the term the adhesive fracture energy, G_a.

3.4.1. Identification of the material parameters

3.4.1.1. Stress versus strain behaviour of the adherend materials

The constitutive behaviour of the mild-steel adherends used in the EPFM wedge-peel specimens is modelled using the rate-independent, isotropic J_2 elastoplastic

theory where the strain increments, $d\varepsilon_{ij}$, are evaluated as the sum of the elastic (superscript *e*) and plastic (superscript *p*) strain increments, such that:

$$d\varepsilon_{ij} = d\varepsilon_{ij}^{e} + d\varepsilon_{ij}^{p} \tag{3.25}$$

The terms on the right-hand side are given by:

$$d\varepsilon_{ij}^{e} = \frac{1+\nu}{E} d\sigma_{ij} - \frac{\nu}{E} d\sigma_{kk} \tag{3.26}$$

where E is the Young's modulus and ν is the Poisson ratio of the material, and, by:

$$d\varepsilon_{ij}^{p} = \frac{3}{2} d\bar{\varepsilon}^{p} \frac{d\sigma_{ij} - \sigma_{kk}/3}{\bar{\sigma}} \tag{3.27}$$

where $\bar{\varepsilon}^{p}$ and $\bar{\sigma}$ denote the effective plastic strain and the effective stress, respectively, which are related to each other through the hardening law. The material parameters are therefore defined by the Young's modulus of the material, E, the Poisson ratio, ν, and a hardening law. They were determined by fitting the curve in Figure 3.8(a), using the least-square method, with Equation (3.28):

$$\sigma = \begin{cases} E\varepsilon & , \quad \varepsilon < \frac{\sigma_0}{E} \\ \sigma_0 \left(\frac{E\varepsilon}{\sigma_0}\right)^{n} & , \quad \varepsilon \geq \frac{\sigma_0}{E} \end{cases} \tag{3.28}$$

The values of these parameters are given in Table 3.1 and the resulting fit is presented in Figure 3.8(a). The aluminium alloy used for the adherends for the LEFM TDCB specimens showed no signs of plastic deformation during the tests and was therefore modelled as a linear-elastic material, see Table 3.1 (Hadavinia et al., 2006).

Table 3.1: Material properties used in the model.

Material	E [GPa]	ν [-]	σ_0 [MPa]	η [-]	n [-]
Mild steel	210	0.30	124	-	0.14
Aluminium alloy	72.4	0.33	-	-	-
Epoxy adhesive	6	0.45	13	87 000	0.13

3.4.1.2. Stress versus strain behaviour of the adhesive

The stress versus strain behaviour of the adhesive is shown in Figure 3.8(b) and, since there is no significant rate dependence, the Young's modulus and hardening behaviour were determined by least-square fitting all of these curves to the following equation:

$$\sigma = \begin{cases} E\varepsilon & , \quad \varepsilon < \frac{\sigma_0}{E} \\ \sigma_0 \left[1 + \eta\left(\varepsilon - \frac{\sigma}{E}\right)\right]^n & , \quad \varepsilon \geq \frac{\sigma_0}{E} \end{cases} \tag{3.29}$$

It should be noted that Equation (3.29) makes use of the Swift hardening-law and, compared with Equation (3.28), it has an additional material parameter, η, which enables a better match to the experimental curves. Figure 3.8(b) reveals a good agreement between Equation (3.29) and the experimental measurements, and the values of the material parameters used are given in Table 3.1.

Adhesives and polymeric materials in general often exhibit different yield limits in tension and in compression, that is a pressure-dependent yield behaviour (Raghava et al., 1973). This type of behaviour, discarded in the above Equation, could have been taken into account in the model at limited additional development costs with a Drucker-Prager (1952) or Raghava (Raghava et al., 1973) yield criterion. However, this added complexity did not appear to be necessary to get accurate numerical predictions, most likely because in all the configurations being studied, the adhesive was mainly yielding in tension to the exception of the small zone of reverse plastic loading, referred to as zone B (see Section 3.4.3.2 below), which will be later shown to be of secondary importance.

3.4.1.3. Identification of the CZM parameters

The traction versus separation law characterising the fracture process in the adhesive is difficult to measure directly, since the fracture phenomena take place at a very small-scale that is difficult to isolate experimentally while imposing a stress state similar to the one occurring at a crack tip. Also, the traction versus separation law represents the overall effect of the fracture process, and is not intended to reproduce its exact details. Hence, an assumption is made about its shape, to limit the number of parameters to be identified, and the defining material parameters are determined indirectly by inverse analysis. This approach has been previously successfully adopted by Pardoen et al. (2005) and Salomonsson and Andersson (2008).

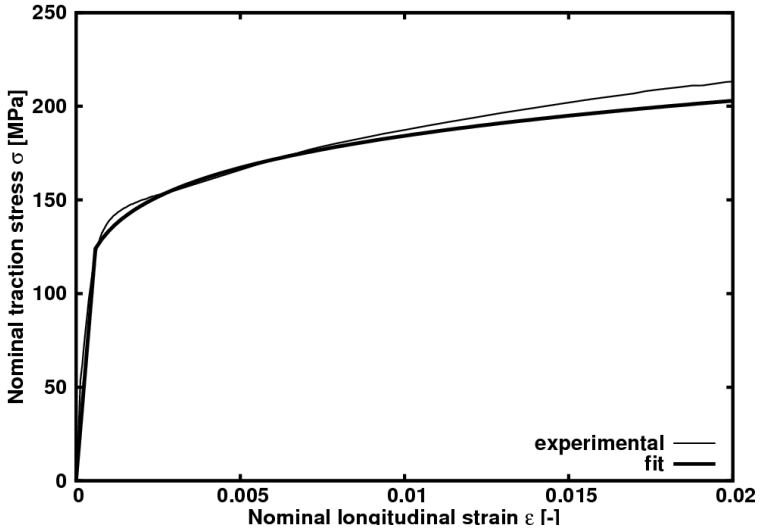

(a)

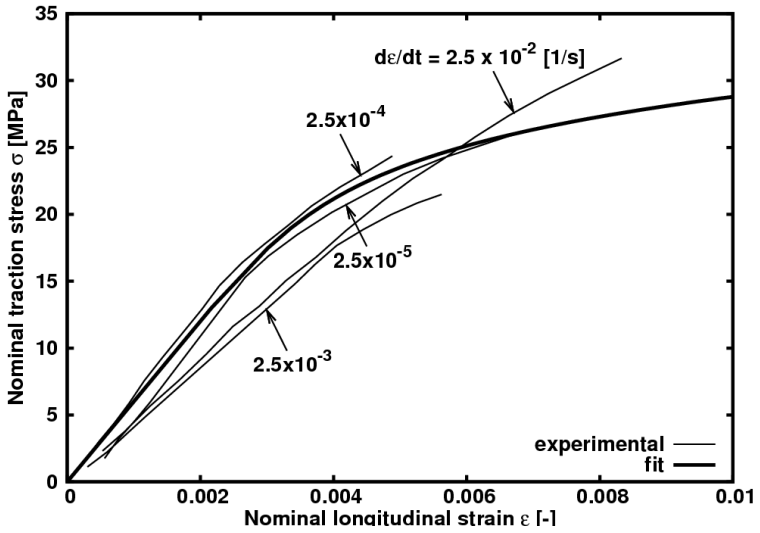

(b)

Figure 3.8: The experimental tensile stress versus strain curves and corresponding fitted models for (a) the mild-steel adherends, and (b) the adhesive used for the wedge-peel tests.

The particular shape used by Tvergaard and Hutchinson (1992) has been chosen for the present work for its simple, piece-wise linear definition. It corresponds to Figure 3.3(b) with $\lambda_1 = 0.15$ and $\lambda_2 = 0.50$. The only two remaining parameters to

be identified are δ_n^c, the critical opening displacement at which the tractions drop to zero, and, $\hat{\sigma}$, the peak stress, i.e. the 'strength' of the fracture process zone. These are assumed to be stress-state independent and, hence, will be kept constant when the two different test specimens, and all their many different test configurations, are modelled, see below. Therefore, they have been determined by minimising the overall mismatch between the numerical predictions and experimental values over the full range of test specimens and test configurations for which experimental data are readily available, and which consist of three EPFM wedge-peel and six LEFM TDCB test results, see Tables 2.1 and 2.2. When the locus of joint failure was near the centreline, the cohesive elements were placed along the centreline of the adhesive layer, and when near the adhesive/adherend interface they were located at the interface, see Table 2.2. The mismatch has been evaluated as the maximum relative error between the experimental value, X_i^{exp}, of the average radius of curvature (in the case of the wedge-peel test specimens), or of the adhesive fracture energy (in the case of the TDCB test specimens), and the corresponding numerical prediction, X_i^{num} amongst these nine test specimens/test configurations, such that:

$$\phi = \max_i \left| \frac{X_i^{num}}{X_i^{exp}} - 1 \right| \quad (i = 1,2,\ldots,9) \tag{3.30}$$

The pair of values $(\delta_n^c, \hat{\sigma})$ that minimizes ϕ was found with the assistance of the general-purpose in-house optimization software Minamo (2010), which is based on genetic algorithms. The above procedure gave a value of δ_n^c equal to 1.9 μm and a value of $\hat{\sigma}$ equal to 87 MPa, and from Equation (3.19), these yield a value for the intrinsic work of fracture, Γ_0, equal to 112 J/m^2. It is noteworthy that the sensitivity analysis showed that a variation of ±1% in δ_n^c and in $\hat{\sigma}$ resulted in a change in the numerically-predicted values of the average radius of curvature, or the adhesive fracture energy, by ±1%; and when this variation was changed to ±5% the change in the latter two quantities was ±10%. Thus, in the present work, the values of $\hat{\sigma}$ = 87 MPa and Γ_0 = 112 J/m^2 will now be kept constant for all the subsequent numerical-modelling studies.

3.4.2. Comparison with the experimental results

3.4.2.1. The EPFM wedge-peel tests

Figure 3.9(a) compares the numerically-predicted values of the average radius of curvature as a function of the thickness of the adhesive layer, h_{adh}, with the corresponding experimental values for the EPFM wedge-peel tests, which all possessed an adherend arm thickness, h, of 0.78 mm. In all these specimens failure occurred close to the centreline of the adhesive layer, i.e. under quasi pure mode I

conditions, and, therefore, the symmetric model was used in which the crack was forced to run along the centreline of the adhesive layer. The current model accurately predicts the change of the radius of curvature as a function of the adhesive layer thickness, and the numerical predictions are all within $\frac{\Delta R_a}{R_a} = 10\%$ of the experimental values.

3.4.2.2. The LEFM TDCB tests

Figure 3.9(b) shows the comparison between the experimental and predicted values of the adhesive fracture energy, G_a, as a function of the thickness of the adhesive layer, h_{adh}, for the LEFM TDCB test specimens quoted in Table 2.2. The energy dissipation in the bulk of the adhesive layer, Γ_b, varies with a change in the value of h_{adh} and is about 35 to 50% of the experimentally-measured values of G_a; whilst the intrinsic work of fracture, Γ_0, which is, of course, constant in value is responsible for the remaining contribution to the value of G_a.

In Figure 3.9(b) there are several other noteworthy features. Firstly, for the TDCB specimens where the crack propagated near the centreline of the adhesive layer, i.e. under quasi pure mode I conditions, the experiments were again modelled by forcing the crack to run along the centreline of the specimens. The corresponding numerically predicted values of G_a accurately reflect the variation of G_a with h_{adh} that was observed experimentally, namely a steady increase up to a plateau value after passing through a small local peak at an intermediate thickness of $h_{adh} \cong$ 0.40 mm. However, the numerically-predicted values all lay below the corresponding experimental values by a maximum of about 15%, which reveals that the model tends to underestimate the energy dissipation. Secondly, the TDCB specimens, where the crack propagated with some degree of mode mixity close to one of the adhesive/adherend interfaces, were modelled by forcing the crack to run exactly along one of the adhesive/adherend interfaces. The corresponding numerically-predicted values of G_a are again in excellent agreement with the experimental values. Thus, the model is also capable of predicting the observed decrease in G_a when the crack runs close to one of the adhesive/adherend interfaces. This success of the model in this respect arises from a decrease in the energy dissipation in the bulk of the adhesive layer, Γ_b, and this is associated with the zones of plastic-energy dissipation in the adhesive layer not being allowed to fully develop on both sides of the crack plane when the crack is very close to the adherend.

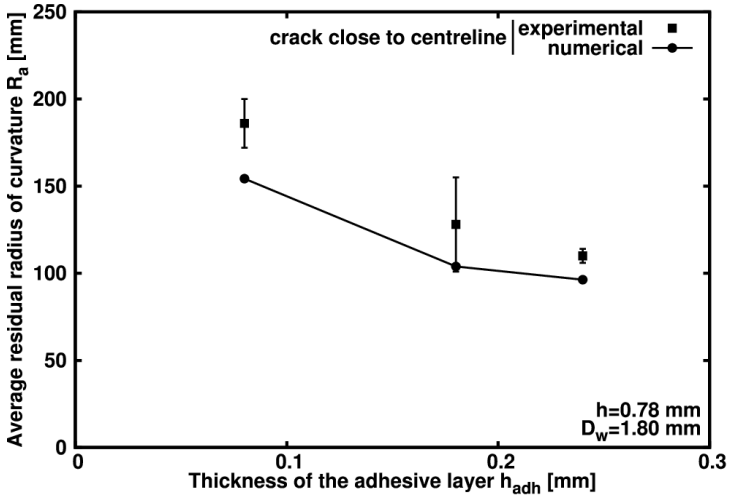

(a)

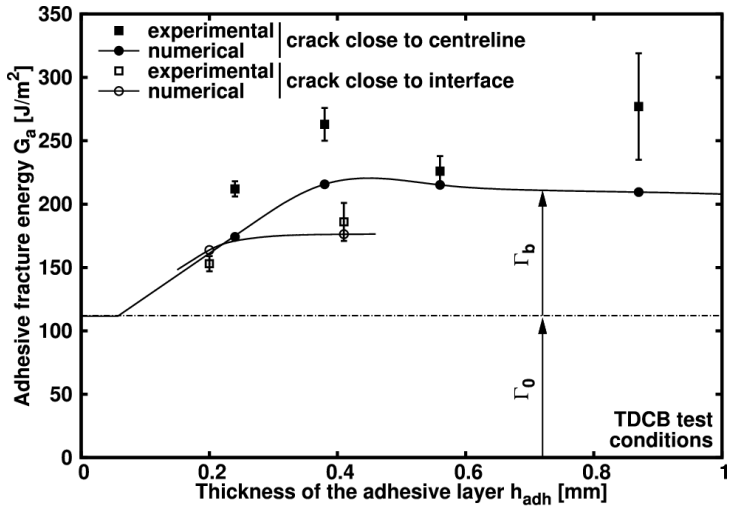

(b)

Figure 3.9: Comparison between the experimental and numerically-predicted values obtained (a) from the EPFM wedge-peel test specimen, and (b) from the LEFM TDCB test specimen.

3.4.3. Analysis of the different contributions to the adhesive fracture energy G_a

The results discussed above have shown a very good agreement between the experimental measurements and the numerical predictions for the two very different types of test specimen, and for a wide range of thicknesses of the adhesive layer. These observations validate the proposed modelling approach which will now be used (a) to explore other test configurations, and hence (b) to address the effects of constraint of the adhesive layer, imposed by the presence of the relatively high modulus adherends. In order to limit the scope of the present paper, only test configurations where the crack propagates through the adhesive layer near the centreline will be discussed.

3.4.3.1. Locked-in elastic strain energy Γ_e

Figure 3.10 shows the calculated elastic energy that is locked-in the adhesive layer, Γ_e, versus the plastic-energy dissipation, Γ_p, for both the LEFM TDCB and EPFM wedge-peel tests, and the results cover a far wider range of test configurations than was tested experimentally.

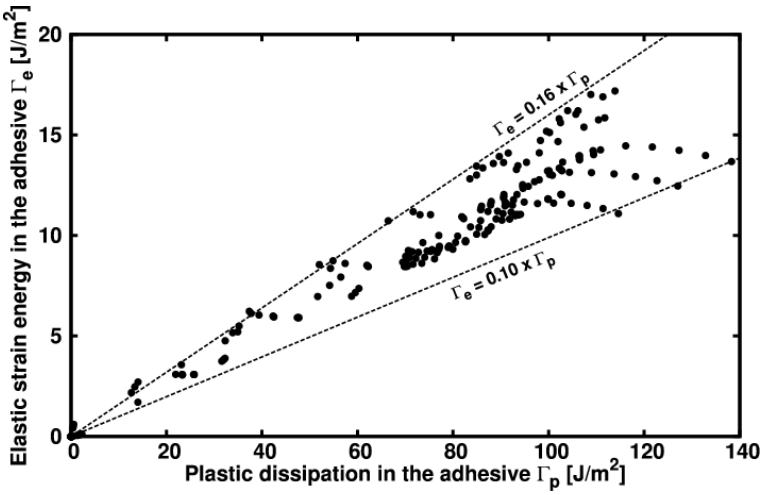

Figure 3.10: The predicted locked-in elastic energy the adhesive as a function of the plastic dissipation in the adhesive layer, for the two specimen geometries and the different test configurations.

For instance, in the modelling studies the values of the adherend thickness, h, in the wedge-peel test was varied from 0.78 mm to 32 mm and the thickness of the wedge was varied from 0.9 to 3.6 mm. The results show that Γ_e scales linearly with Γ_p. Nevertheless, the contribution from the relatively low values of Γ_e is only 16% of Γ_p (i.e. no more than about 8% of the adhesive fracture energy, $\mathrm{G_a}$)

regardless of the specimen geometry and test configuration. The plastic-energy dissipation term, Γ_p, thus dominates the contribution to G_a of the work expended per unit area of crack advance in the bulk of the adhesive layer, Γ_b, as may be seen from Equation (3.22).

3.4.3.2. Contributions to the plastic-energy dissipation Γ_p

Introduction. Figure 3.11(a) shows a typical spatial distribution of the plastic-energy dissipation within the upper half of the adhesive layer for a LEFM TDCB test specimen with an adhesive layer thickness of 0.24 mm. The contours of the regions of active plasticity where the plastic strain-rate is non-zero are shown, together with the magnitude of the associated plastic dissipation. The regions where only elastic behaviour occurs are represented in white.

Three distinct zones of plastic-energy dissipation may be identified. Zone A shows intense plastic-energy dissipation, slightly above and ahead of the crack tip and fans out towards the adhesive/adherend interface. Zone B shows much less intense plastic-energy dissipation and extends, behind the crack tip, close to the crack face. The new zone observed in the present analysis, 'Zone C', shows a maximum in the plastic-energy dissipation at the adhesive/adherend interface, approximately directly above the crack tip, and spreads out in the direction of the crack plane both towards regions located ahead and behind the crack tip. Zone C merges with Zone A at approximately the mid-distance from the crack plane. Figure 3.11(b) shows the aggregated distribution of plastic-energy dissipation in the thickness direction obtained by integrating the spatial distribution of Figure 3.11(a) along horizontal lines from far ahead of the crack tip down to the section K–K'. Plastic work is dissipated over the full thickness of the adhesive layer, although the thin layer of material located right above the crack plane does not seem to contribute significantly. Zone A and Zone C each involve a maximum in the plastic dissipation slightly above the crack plane and just below the adhesive/adherend interface, respectively. The adhesive material located in between these regions also shows significant plastic-energy dissipation, with one zone gaining in intensity as the other dies away.

The total plastic-energy dissipation, Γ_p, can be broken down by considering separately the three contributions from Zones A, B and C. Hence, Equation (3.23) becomes:

$$G_a = \Gamma_0 + \Gamma_e + \Gamma_p^A + \Gamma_p^B + \Gamma_p^C \tag{3.31}$$

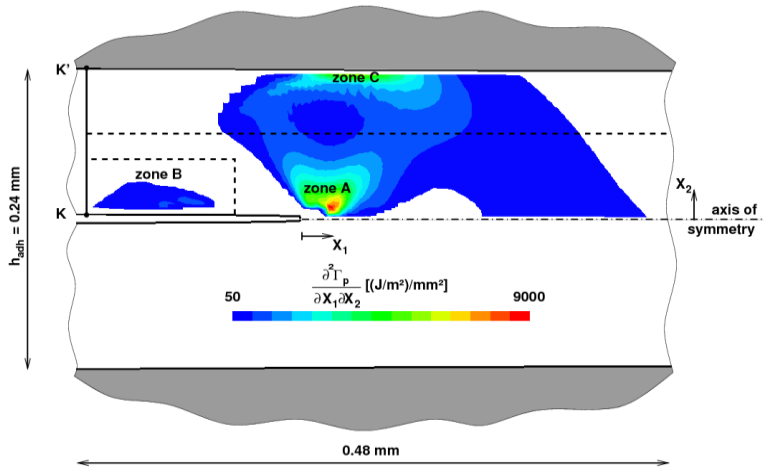

(a)

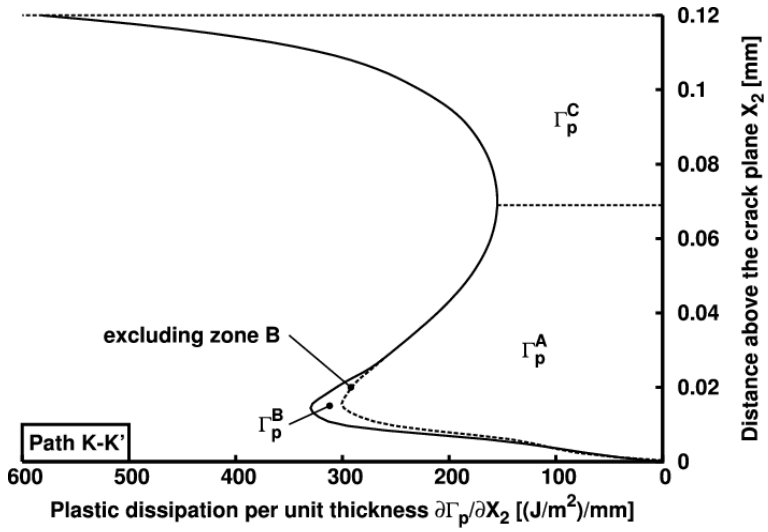

(b)

Figure 3.11: Modelling results for the adhesive layer in the LEFM TDCB test specimen: (a) spatial distribution of the plastic-energy dissipation, and (b) the resulting distribution in the thickness direction. (Results are shown for the upper symmetrical part of the specimen only.)

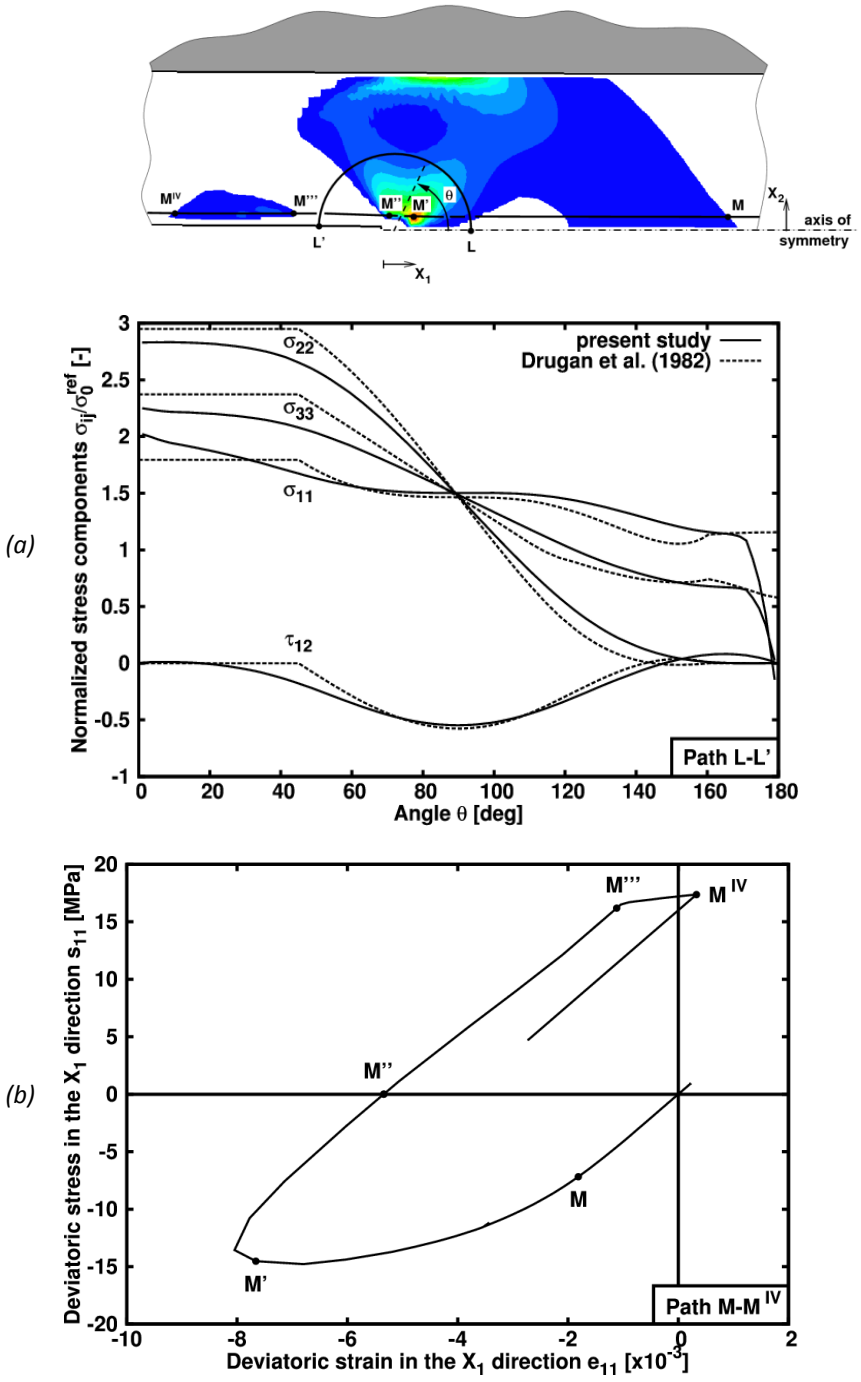

Figure 3.12: The predicted typical stress distributions responsible for the appearance of (a) Zone A, and (b) Zone B. (In (a) a comparison with the analysis by Drugan et al. (1982) is shown.)

The energy contribution from Zone B, Γ_p^B, is obtained by limiting the domain of integration in Equation (3.24) so as to encompass Zone B completely, and by excluding Zones A and C. Such a domain is illustrated by the dotted line around Zone B in Figure 3.11(a). Upon removal of the contribution of Zone B, the spatial distribution of Γ_p of Figure 3.11(b) is modified as shown by the dotted line labelled as 'excluding Zone B'. The energy contribution of Zone A, $\Gamma_{\mathrm{p}}^{\mathrm{A}}$, is then estimated by integrating the modified curve from the crack plane up to its local minimum as shown by the horizontal dotted lines in Figures 3.11(a) and 3.11(b). The energy contribution from Zone C, $\Gamma_{\mathrm{p}}^{\mathrm{C}}$, is then ascertained in a similar manner by integrating the modified curve from its local minimum up to the adhesive/adherend interface. (This approximation had to be introduced, since Zones A and C merge together and it is therefore not possible to isolate rigorously their individual contributions, which is needed in order to quantify the separate physical mechanisms of plastic-energy dissipation in the adhesive layer.)

Origin of Zone A. The stress components along the semi-circular path L–L' about the crack tip are plotted in Figure 3.12(a) and compared with the asymptotic crack-tip field obtained semi-analytically by Drugan et al. (1982) in the particular case of an elastic-ideally plastic solid under steady-state, mode I crack propagation[5]. For angles below 170 degrees, the agreement between the two predictions is excellent, which proves that the plastic dissipation in Zone A can be attributed to the crack-tip stress-field. Zone A will be therefore referred to as 'crack tip plasticity'. Moreover, as can be seen in Figure 3.11(a), Zone A spans an angular sector ranging from about 0 to 125-130 degrees immediately followed by an elastic sector, which is also in agreement with the results of Drugan et al. (1982). This phenomenon is typical of propagating cracks, since stationary cracks show plasticity at all angles, as has been established by Rice (1967).

Origin of Zone B. The existence of Zone B also agrees with the results of Drugan et al. (1982). They calculated that the elastic sector following Zone A was itself followed by a second plastic sector, ranging from 160 up to 180 degrees. They attributed this extra plastic sector to reverse plastic loading, i.e. 'reverse plasticity'. Figure 3.12(b) shows, along the streamline M–M$^{\mathrm{IV}}$ passing through Zone B, the variation of the deviatoric stress in the direction parallel to the crack plane, $s_{11} = (2\sigma_{11} - \sigma_{22} - \sigma_{33})/3$, as a function of the corresponding deviatoric strain component, $e_{11} = (2\varepsilon_{11} - \varepsilon_{22} - \varepsilon_{33})/3$. These are obtained by removing any

[5] For consistency purpose, the stresses obtained in the present study are divided by a reference value of 30 MPa which is the estimated yield stress of the adhesive material had the stress-strain curves in Figure 3.8(b) been fitted with an elastic-ideally plastic equation.

hydrostatic pressure contribution from the total stress and strain tensors. The tensorial equations of plasticity, see Equations (3.25-3.27), become scalar, i.e. the σ_{kk} term vanishes, when they are expressed in terms of the deviatoric components:

$$de_{ij} = \frac{1+\nu}{E} ds_{ij} + \frac{3}{2} ds_{ij} \frac{d\bar{\varepsilon}^p}{\bar{\sigma}} \tag{3.32}$$

which simplifies the interpretation of the stress versus strain variations. Ahead of the crack tip, the material is stretched in the X_2 direction due to the opening of the joint with a lateral contraction in the X_1 direction, due to the Poisson effect. The value of e_{11} is thus negative up to point M', see Figure 3.12(b). At the same time, s_{11} varies, first linearly with e_{11} (up to point M) and then non-linearly (up to point M') as regions of the material enter the highly stressed region around the crack tip where the material deforms plastically. Completely past the crack tip, up to point M'' in Figure 3.12(b), the material essentially unloads, and s_{11} returns to zero while e_{11} retains a non-zero negative value due to the compressive plastic strains that developed between point M and point M'. Past point M'', the magnitude of this permanent deformation is decreased as part of a stress and strain redistribution process over the full thickness of the adhesive layer and adjacent adherend. This process first proceeds elastically, up to point M''', but then develops tensile plastic-strains which gives rise to Zone B to compensate for the compressive plastic-strains that were accumulated between point M and point M'. From this process comes the phenomenon of 'reverse plastic loading'.

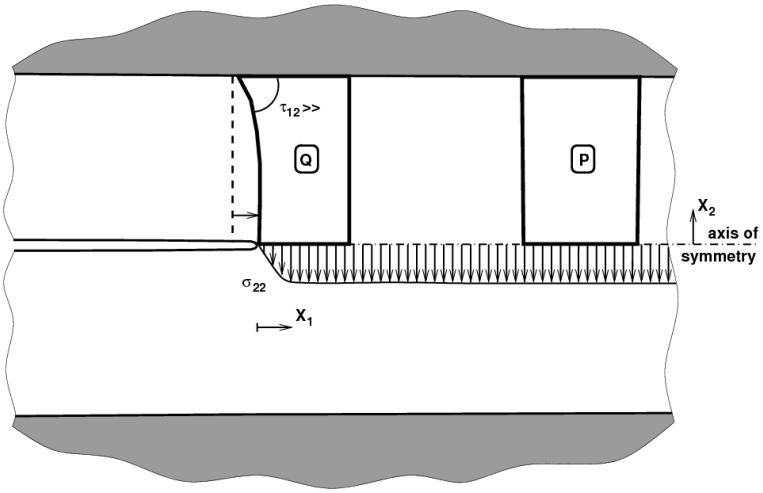

Figure 3.13: A schematic representation of the deformation mechanism responsible for the appearance of Zone C.

Origin of Zone C. Plastic-energy dissipation in Zone C arises from the relatively large shear stresses which develop at the adhesive/adherend interface, approximately directly above the crack tip. Figure 3.13 provides a schematic representation of the mechanism responsible for such plastic deformation. Namely, as a result of the opening of the adhesive joint, the material ahead of the crack tip is loaded in tension in the X_2 direction. Due to the Poisson effect, the adhesive tends to contract in the lateral, X_1 direction. Considering the material volume P in Figure 3.13, it is constrained by the material on both the left and right boundaries involving a near uniaxial deformation state. Hence, there is no possible net lateral contraction. If we now consider the material volume element Q of Figure 3.13, its left boundary is interacting with a region where unloading takes place in the direction of the opening of the joint, and is thus allowed to contract laterally. Although, this contraction is still hindered in the vicinity of the perfectly-bonded interface since the adherend is much stiffer than the adhesive. Thus, this difference in contraction in volume Q, between its upper region down to its lower region, induces relatively large shear strains and stresses in the top-left corner of the volume Q ; and these are responsible for the appearance of Zone C, as illustrated in Figure 3.13.

3.4.4. Parametric modelling of the adhesive fracture energy for the LEFM TDCB test

3.4.4.1. Effect of the thickness of the adhesive layer, h_{adh}

Introduction. Figure 3.14(a) shows the numerically-predicted values of the adhesive fracture energy, G_a, as a function of the thickness of the adhesive layer, h_{adh}, for the LEFM TDCB test, with the crack running along the centreline of the adhesive layer. Three distinct regimes (denoted by I, II and III) are identified. In Regime I, for very thin layers below h_{adh}≅0.05 mm, the value of G_a is constant and is at its lowest value. In Regime II for thicker layers, up to h_{adh}≅0.45 mm, the value of G_a increases first linearly and then reaches a peak. In Regime III, for h_{adh}>0.45 mm, the adhesive fracture energy decreases somewhat at first and then reaches a plateau value with a magnitude significantly larger than the lowest value which is exhibited for very thin adhesive layers. In previous experimental studies, Regime I has been observed by Chai (1986, 1988), and Regimes II and III by Bascom et al. (1975), Kinloch and Shaw (1981) and Chai (1986).

Figure 3.14(b) shows the actual plastic-energy dissipation in each of the three zones (i.e. Zones A, B and C, see Figure 3.11) which, when all added to the value of Γ_0, give most of the adhesive fracture energy, G_a. The plastic-energy dissipation associated with Zone B is negligible. Therefore, the present discussions will focus on the contributions arising from Zones A and C to explain the results shown in

Figure 3.14(a). In Regime I, these contributions are zero, so G_a is constant and equal to Γ_0, see Equation (3.18). In Regime II, both Γ_p^A and Γ_p^C increase with increasing thickness of the adhesive layer, hence the value of G_a increases. Finally, in Regime III, Γ_p^A becomes constant, whilst Γ_p^C reverts to zero, which explains why G_a decreases very steadily with increasing h_{adh} and reaches a plateau value which is significantly higher than Γ_0.

(a)

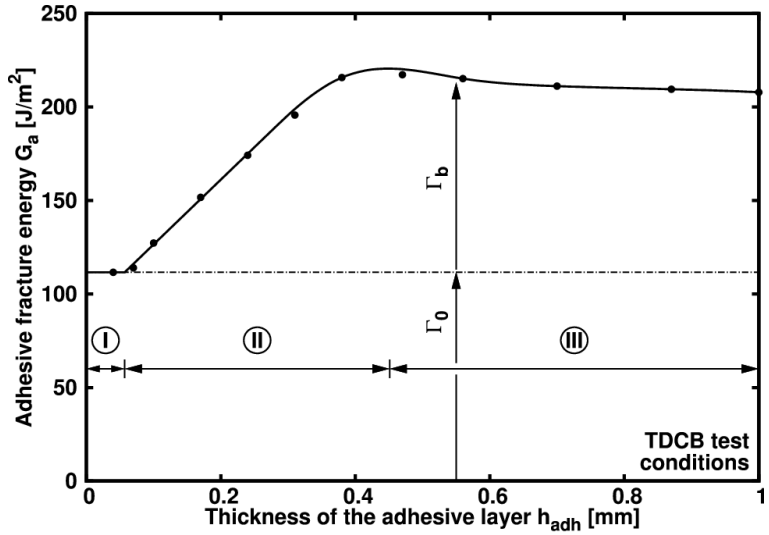

(b)

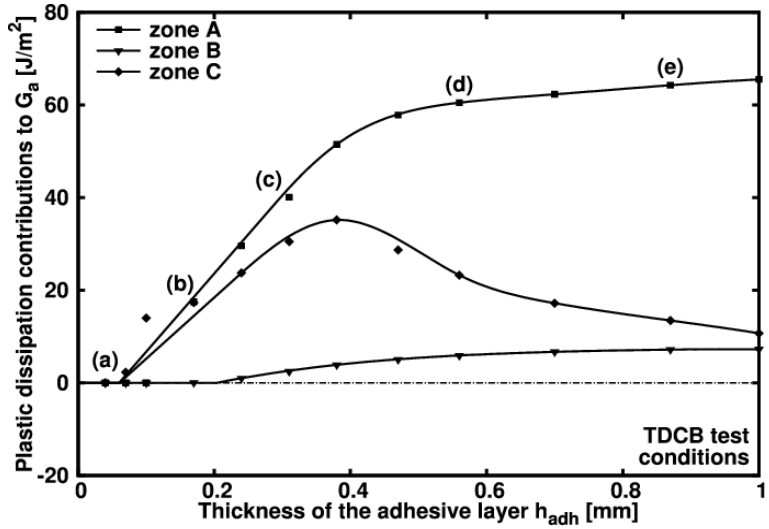

Figure 3.14: The predicted (a) adhesive fracture energy, G_a, as a function of the thickness of the adhesive layer, h_{adh}, for the LEFM TDCB test specimen, and (b) contributions from Zones A, B and C to the plastic-energy dissipation to the value of G_a, again as a function of h_{adh}.

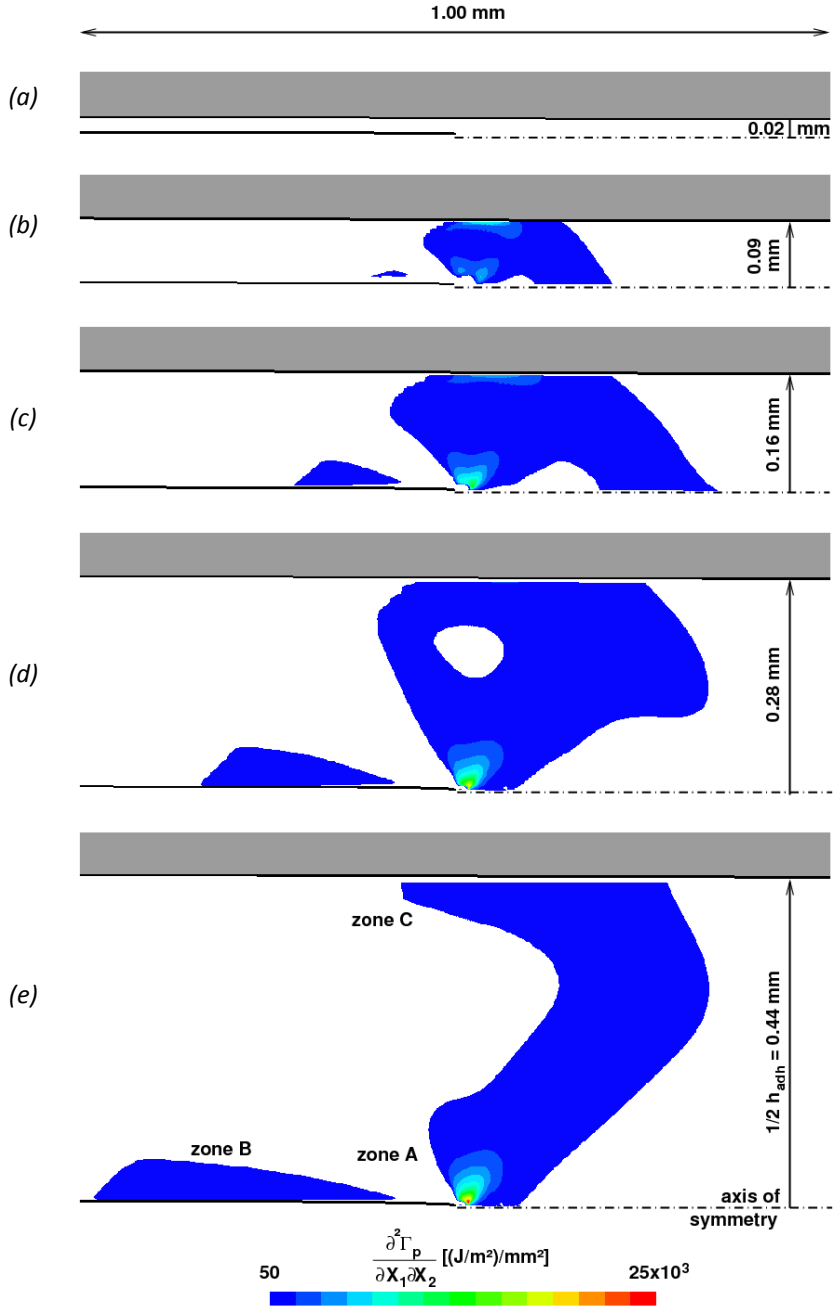

Figure 3.15: The predicted spatial distribution of the plastic-energy dissipation within for the LEFM TDCB test specimens, with an adhesive layer thickness, h_{adh}, of: (a) 0.04 mm, (b) 0.17 mm, (c) 0.31 mm, (d) 0.56 mm, and, (e) 0.87 mm. (Results are shown for the upper part of the specimens only.)

Considering the separate role of the three zones of plasticity, Figure 3.15 shows the spatial distribution of the plastic dissipation in the adhesive for the data points labelled from (a) to (e) in Figure 3.14(b). In Regime I, see point (a), there is no plastic-energy dissipation. In Regime II, see points (b) and (c), Zones A and C are merged and, together, span the full thickness of the adhesive layer. As the adhesive layer thickness is increased, they have more material available in which to develop, with their dimensions scaling with h_{adh}. This is associated with an increase in the plastic-energy dissipation terms, Γ_p^A and Γ_p^C. These observations agree with the explanation of Kinloch and Shaw (1981) for Regime II. Namely, that the adhesive layer is fully plastic across its height and the value of G_a increases with increasing thickness, since there is now more adhesive material in which plastic-energy dissipation may occur. Looking in more detail at points (b) and (c) in Figure 3.15, the intensity of the plastic dissipation in Zone A increases as the layer becomes thicker, whilst that in Zone C decreases. This effect explains why Γ_p^A and Γ_p^C are not directly proportional to h_{adh}, and why the increase in Γ_p^A is slightly larger than for Γ_p^C. In Regime III, see points (d) and (e), Zones A and C start separating. As a consequence, their dimensions do not scale with h_{adh} anymore. In particular, the extent of Zone A stabilises so that the value of Γ_p^A levels out while Zone C and, hence, Γ_p^C tends to vanish. Once more, these observations agree with the explanation suggested by Kinloch and Shaw (1981) for Regime III, who concluded that the adhesive layer is not fully plastic in Regime III.

From the above, several noteworthy points arise. Firstly, in the present work, and in the previous work of Kinloch and Shaw (1981), all the criteria for the TDCB test to meet the requirements of following the principles of LEFM are readily met: clearly the use of the relatively thick, high yield-stress aluminium-alloy adherends in the TDCB adhesive joint basically ensures that such requirements are satisfied. Secondly, considering some suitable 'intrinsic' length scale to compare with the range of h_{adh} values that were employed, which typically were between 0.2 to 0.9 mm, then the size of the plastic zone in a bulk specimen of the adhesive has been suggested as the most obvious such parameter. Indeed, the previous work has shown that the peak in the value of G_a occurs when the thickness of the adhesive layer becomes approximately equal to twice the radius of the plastic zone in a bulk specimen under plane-stress conditions. That is, when:

$$h_{adh} = \frac{1}{\pi}\frac{EG_{Ic}}{\sigma_t} \tag{3.33}$$

where E is the Young's modulus, G_{Ic} is the adhesive fracture energy for a bulk sample and, σ_t is the yield stress in tension. Now the value of G_{Ic} may be estimated from Figure 3.14(a) to be about 205 J/m^2, i.e. the value of G_a that would be

expected for very thick adhesive layers. Therefore, taking σ_t to be equal to 30 MPa, then Equation (3.33) gives a thickness for the adhesive layer at the peak value of G_a to be about 0.45 mm. Indeed, this is in very good agreement with the experimental value of h_{adh} for the position of the peak, see Figure 3.14(a). Finally, the present work provides a better insight into the explanation offered by Kinloch and Shaw (1981) for the decrease in the value of G_a that follows this peak. They suggested that it resulted from a lower degree of constraint imposed by the adherends and, hence, a smaller plastic zone in the plane ahead of the crack tip. However, whilst there is an important role of the degree of constraint, the present study suggests that the explanation is more complex than envisaged by Kinloch and Shaw (1981).

Constraint effects. When constrained between the two high-modulus adherends, the adhesive is not allowed to deform freely, as it would in a bulk sample. Indeed, it deforms less due to the far higher stiffness of the adherends, which introduces an additional constraint effect. Obviously, the thicker the adhesive layer, then lower is the degree of constraint on the crack plane and, in particular, at the crack tip. Taking the opening angle of the cohesive zone at the crack tip, θ, as a measure of the deformation at the crack tip, see Figure 3.16, the corresponding constraint factor, f, may be defined as:

$$f = 1 - \frac{\theta}{\theta_b} \tag{3.34}$$

where θ_b is the predicted value of θ in a bulk specimen under small-scale yielding conditions. It follows from Equation (3.34) that f is equal to 0 in a bulk specimen where the adhesive deforms freely, and that it progressively tends to 1 as the adhesive layer is forced to follow the more rigid deformations of the adherends, see Figures 3.16(a) and 3.16(b). In Figure 3.17 the values of the constraint factor, f, have been calculated from Equation (3.34), corresponding to the tests that were modelled in Figure 3.14. It is of interest to note that, as for the data shown in Figure 3.14, again three regimes may be distinguished.

Firstly, considering the effects of constraint on the development of Zone A, then for very thin adhesive layers, the constraint factor is very high and nearly constant. According to the definition of f, this means that the adhesive is subject to a very high degree of triaxial stresses. Thus, plastic deformation in the adhesive is severely inhibited to such an extent that the term Γ_p is equal to zero. With increasing thickness of the adhesive layer, the value of f decreases rapidly and, therefore, plastic deformation can more readily develop and Γ_p^A increases rapidly. For a thickness of the adhesive layer of 0.6 mm, and above, the constraint factor attains a minimum, plateau value. Hence, the extent of plastic deformation in Zone A is

now uninhibited by the presence of the adherends, and the value of Γ_p^A also attains a plateau value.

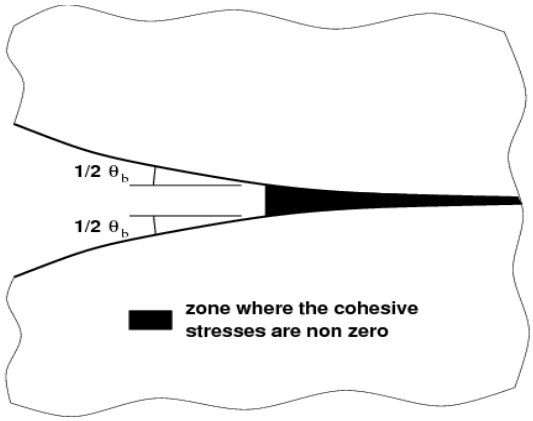

(a)

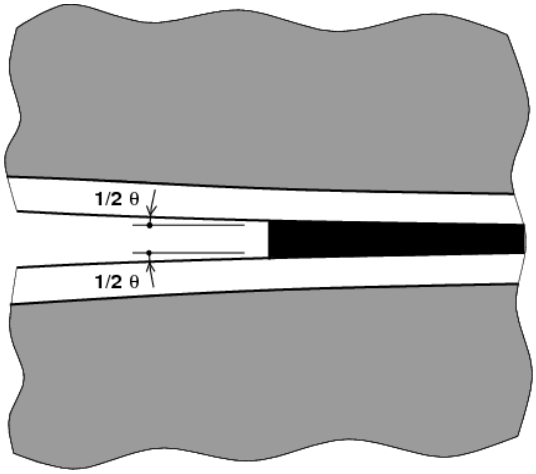

(b)

Figure 3.16: A schematic description of the opening angle of the cohesive zone at crack tip (a) in bulk conditions, and (b) when the presence of the high-modulus adherends limits the deformation in the adhesive.

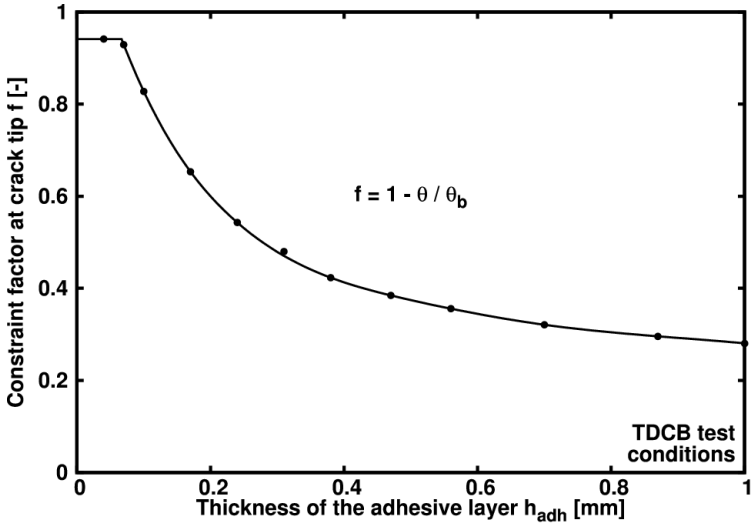

Figure 3.17: The predicted constraint factor at the crack tip, f, as a function of the thickness of the adhesive layer, h_{adh}, for the LEFM TDCB test specimen.

Secondly, considering the effects of constraint on the development of Zone C, the gradient of the constraint from the crack tip to the adhesive/adherend interface must be taken into account. This aspect was discussed in Section 3.4.3.2, where it was shown that this gradient is responsible for the appearance of Zone C, since the adhesive is allowed to contract in the direction parallel to the crack plane to a greater extent near the crack tip than at the adhesive/adherend interface. For very thin layers, i.e. $h_{adh} \leq 0.05$ mm, this gradient of constraint is small, since the constraint is very high both at the crack tip and at the adherend/adhesive interface. As a consequence, Zone C does not develop, see Figure 3.15(a), and the associated plastic-energy dissipation, Γ_p^C, is zero, see Figure 3.14(b). For thicker layers, $h_{adh} > 0.05$ mm, the constraint decreases somewhat at the crack tip and remains high at the adhesive/adherend interface due to the nearby presence of the high-modulus adherend. This creates a significant gradient of constraint which causes the appearance of Zone C, see Figure 3.15(b-e), and the corresponding energy contribution, Γ_p^C, to the adhesive fracture energy, see Figure 3.14(b). However, for thicknesses of the adhesive layer above 0.25 mm, this gradient of constraint decreases since the distance from the crack tip to the adhesive/adherend interface increases whilst the constraint at the crack tip attains a plateau. As a consequence, Zone C progressively vanishes, see Figure 3.15(b-e), and Γ_p^C returns to zero for relatively thick adhesive layers, see Figure 3.14(b).

The above explanations refine the analysis of Kinloch and Shaw (1981) and illustrate the importance of considering the distribution of the degree of constraint within the adhesive layer, as opposed to focusing on a single value taken at a particular location.

3.4.4.2. Effect of the choice of adherend material

Figure 3.18(a) shows the variation of the adhesive fracture energy, G_a, as a function of the thickness of the adhesive layer, h_{adh}, as numerically predicted for the LEFM TDCB test, but now employing mild-steel adherends instead of aluminium-alloy adherends; and again with the crack propagating along the centreline of the adhesive layer. Figure 3.18(a) also shows the modelling results of Figure 3.14(a) that were obtained for the TDCB test specimens with aluminium-alloy adherends. When using mild-steel adherends, the value of G_a is predicted to rise more slowly, and to reach a higher peak value, with the peak value now being about 20 J/m^2 higher and occurring at $h_{adh}\cong$0.6 mm. After this peak value has been attained, the value of G_a again decreases in Regime III for the TDCB test specimen using the mild-steel adherends, but always remains consistently somewhat higher by about 20 J/m^2 compared with the values of G_a for the TDCB specimen employing the aluminium-alloy adherends.

Figure 3.18(b) shows that the constraint factor at the crack tip, f, is higher when the mild-steel adherends are employed for the TDCB test specimen. Although the effect is relatively small, this observation is valid regardless of the thickness of the adhesive layer, but is especially marked for h_{adh} values below 0.6 mm. The fundamental reasons for these predictions are that (a) the modulus of mild steel is approximately three times higher than that for the aluminium alloy (see Table 3.1), and (b) the adherend has a greater impact on the degree of constraint at the crack tip when h_{adh} is small. Now, it should be recalled that a higher degree of constraint leads to a lower extent of plastic-energy dissipation. Thus, these observations explain why, when the mild-steel adherend is used as opposed to the aluminium alloy, the values of Γ_b and, hence, the adhesive fracture energy, G_a, (a) increase more slowly in Regime II, and (b) attain a somewhat similar peak value but at a higher thickness of the adhesive layer.

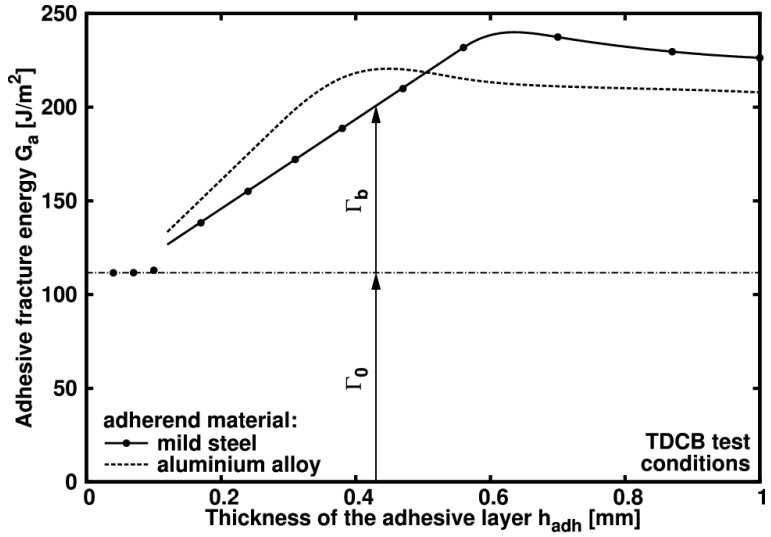

(a)

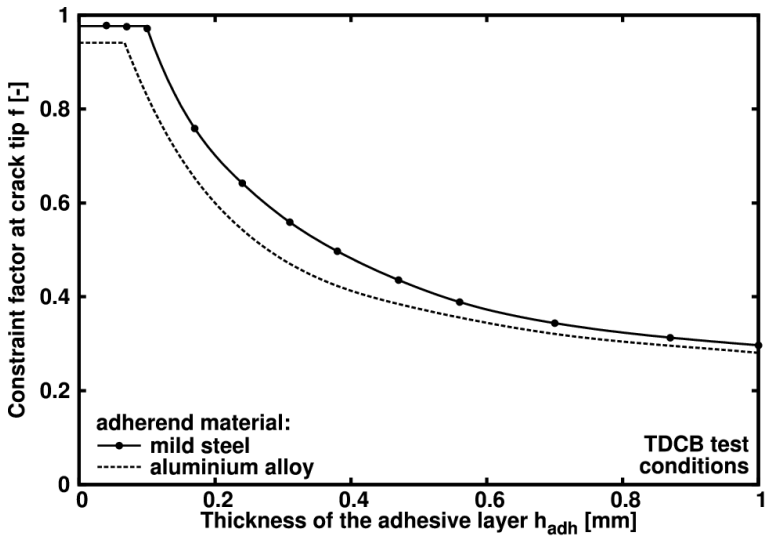

(b)

Figure 3.18: The predicted (a) adhesive fracture energy, G_a, as a function of the thickness of the adhesive layer, h_{adh}, and (b) constraint factor at the crack tip as a function of the thickness of the adhesive layer, h_{adh}. (For the LEFM TDCB test specimen when using mild-steel or aluminium-alloy adherends.)

3.4.5. Parametric modelling of the adhesive fracture energy, for the EPFM wedge-peel test

3.4.5.1. Effect of the thickness of the adhesive layer, h_{adh}

Figure 3.19 shows the numerically-predicted values of the adhesive fracture energy, G_a, as a function of the adhesive layer thickness, h_{adh}, for the EPFM wedge-peel test geometry using mild-steel adherends of different thicknesses, h, with the crack always running along the centreline of the adhesive layer. Figure 3.19 also shows the values of G_a, from Figure 3.18(a), that were predicted for the TDCB test, also employing mild-steel adherends. For the EPFM wedge-peel tests, with the exception of the results for an adherend thickness of 0.78 m, see below, all the predicted relationships follow a similar variation of G_a as a function of the thickness of the adhesive layer, h_{adh}, as was observed for the TDCB test. Namely, the value of G_a first increases linearly and then decreases, after reaching a peak, to a plateau value. The rationale for this behaviour arises from the reasons discussed in Section 3.4.4.1 for the LEFM TDCB specimens. That is, the values of Γ_b and, hence, G_a first increase with increasing h_{adh}, as there is more material available for plastic dissipation. They then decrease in value as the gradient of constraint from the crack plane to the adhesive/adherend interface decreases, which leads to plastic Zone C disappearing.

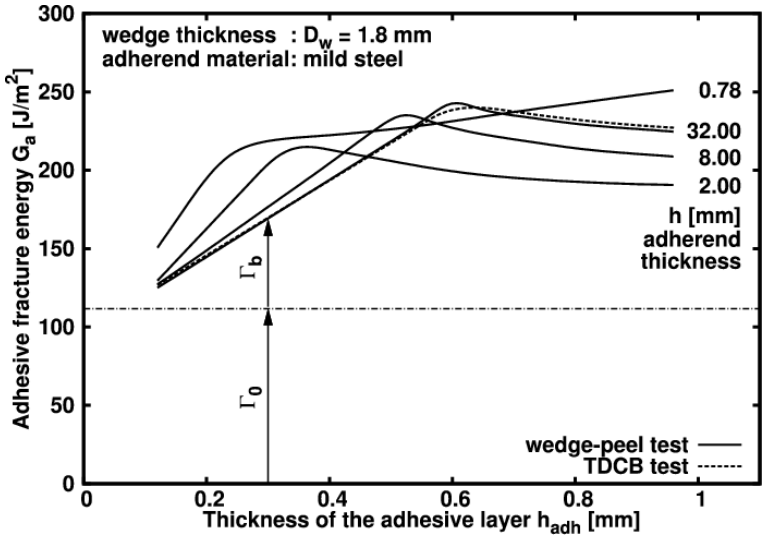

Figure 3.19: The predicted adhesive fracture energy, G_a, as a function of the thickness of the adhesive layer, h_{adh}, for the EPFM wedge-peel test specimen, for different adherend thicknesses, h

Considering the results for the EPFM wedge peel tests for an adherend thickness of 0.78 mm, then bending of the adhesive-coated adherend arms starts to become very significant when using such very thin arms for the adherends. The relatively large degree of bending that occurs induces extra stresses in the adhesive layer which, in turn, magnify the plastic dissipation in Zones A and B, since these are located where the bending stresses are the largest in the adhesive layer, see Figure 3.11(a). As the thickness of the adhesive layer is increased, the bending stresses become larger, since the adhesive layer increasingly contributes to the flexural stiffness of the arms. Hence, the plastic dissipation in Zones A and B steadily increases with increasing thickness of the adhesive layer, instead of reaching a plateau value. Thus, the G_a versus h_{adh} relationship corresponding to $h = 0.78$ mm does not show any peak, even though Zone C disappears, but the value of G_a keeps steadily increasing for thicker adhesive layers. Indeed, the wedge-peel test using arms of a thickness of 0.78 mm is predicted to give values of G_a higher by as much as 50 J/m^2 compared with the results from the other wedge-peel test configurations and with the numerically-predicted values for the TDCB test. However, as will be shown below in Section 3.4.5.4, when such bending effects are taken into account in the present model the results shown in Figure 3.19 for the wedge-peel test employing an adherend thickness of 0.78 mm follow a similar trend to the other results shown in Figure 3.19.

3.4.5.2. Effect of the thickness of the adherend, h

Ignoring, for the reasons discussed above, the results for the wedge-peel test employing adherend arms with a thickness of 0.78 mm, then Figure 3.19 shows that, as the thickness of the arms, h, is increased, the value of G_a (a) rises more slowly as the thickness of the adhesive layer is increased, and (b) reaches a higher peak value, which occurs when the adhesive layer is somewhat thicker. This modification of the G_a versus h_{adh} relationship is similar to that associated with using a relatively high-modulus adherend material in the LEFM TDCB test, see Figure 3.18(a). These common observations arise since, in both types of test specimen, as the stiffness of the adherend is increased the constraint in the adhesive becomes larger, which delays the development of plastic deformation to thicker adhesive layers. Figure 3.19 also shows (see the dashed line) that, as the thickness of adherend is increased, the G_a versus h_{adh} relationship for the EPFM wedge-peel tests is predicted to converge with that for the LEFM TDCB test. This feature is illustrated even more clearly in Figure 3.20, which shows the values of G_a as a function of the adherend thickness, h, for different representative thicknesses of the adhesive layer, h_{adh}, predicted for the EPFM wedge-peel test. Figure 3.20 also shows that, depending on whether the thickness of the adhesive layer, h_{adh}, corresponds to before, or after, the peak value seen in G_a, the value of G_a

predicted for the wedge-peel test decreases, or increases, by a maximum of about 30 J/m^2 as the value of h is changed, before finally attaining the LEFM TDCB value at an adhesive layer thickness, h_{adh}, of about 20 mm.

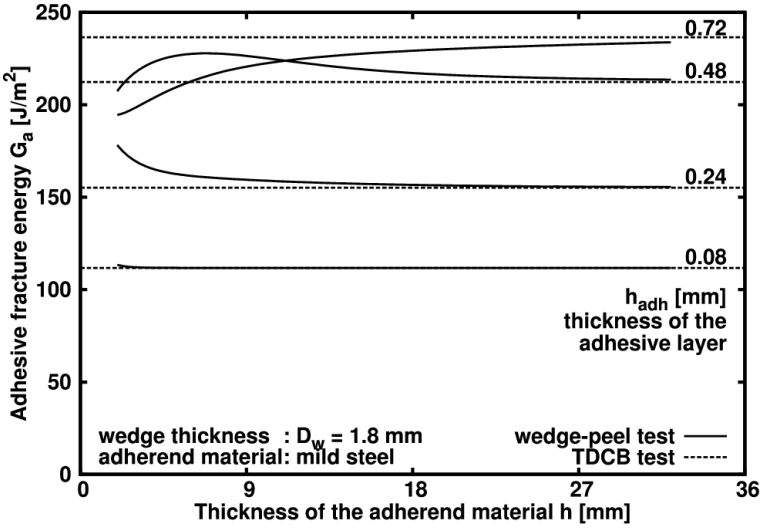

Figure 3.20: The predicted adhesive fracture energy, G_a, as a function of the thickness of the adherend arms, h, for the different EPFM wedge-peel test configurations.

3.4.5.3. Effect of the thickness of the wedge, D_w

Figure 3.21 shows the effect of the thickness of the wedge, D_w, on the G_a versus h_{adh} relationship for the wedge-peel test. Significant effects of the wedge thickness are only observed for specimens where a major contribution from the bending in the adhesive occurs, i.e. for an adherend thickness, $h = 0.78$ mm. Here a thicker wedge induces more bending in the adhesive-coated adherends. This magnifies the associated plastic-energy dissipation in the adhesive layer, and so induces an increase in the value of the adhesive fracture energy, G_a, in proportion to the initial amount of bending.

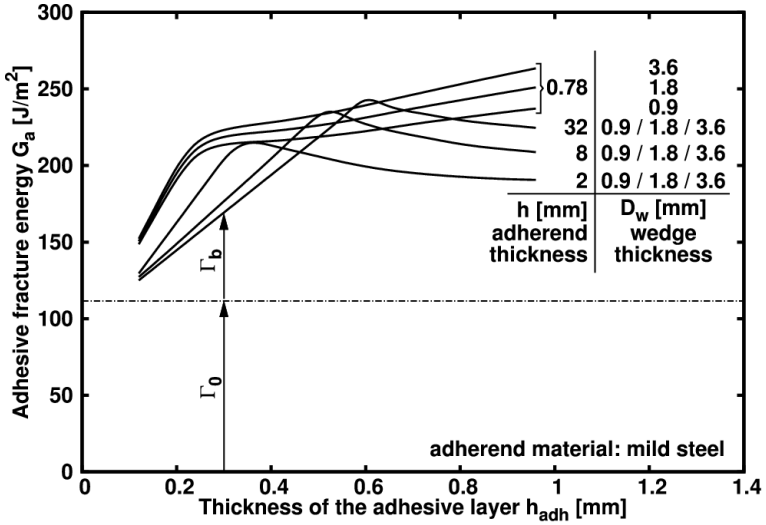

Figure 3.21: The predicted values of the adhesive fracture energy, G_a, as a function of the thickness of the adhesive layer, h_{adh}, for the EPFM wedge-peel test specimen, for different test configurations with varying adherend, h, and wedge, D_w, thicknesses.

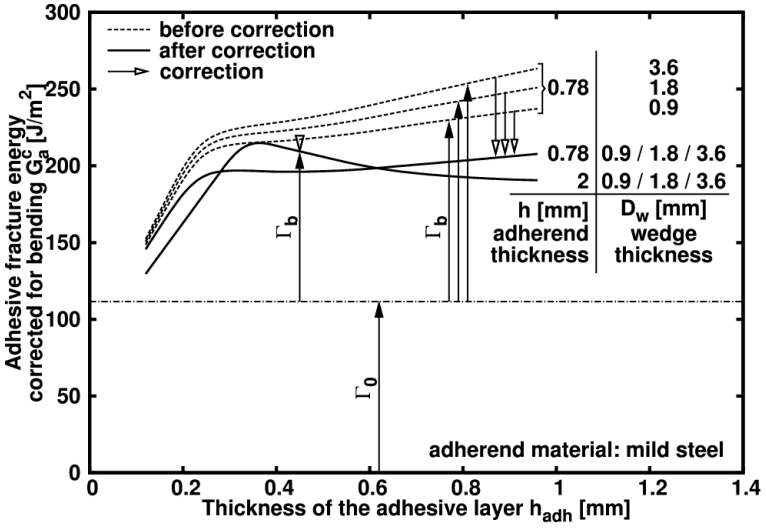

Figure 3.22: The predicted adhesive fracture energy, G_a, corrected for bending in the adhesive layer, as a function of the thickness of the adhesive layer, h_{adh}, for different EPFM wedge-peel test configurations, with varying adherend, h, and wedge, D_w, thicknesses.

3.4.5.4. Adhesive bending corrections

Figure 3.22 shows the values of G_a corresponding to $h = 0.78$ mm and $h = 2$ mm, from Figure 3.19, before and after a correction has been applied for the extra plastic-energy dissipated in the adhesive layer as a result of any bending of the adhesive-coated adherend arms. This correction was evaluated numerically, as an approximation[6], as the energy expended in the adhesive should the specimens be cut along the crack plane prior to being forced to follow the exact same deformation of the arms as seen in the wedge-peel test. The correction is insignificant for adherend arms with a thicknesses of 2 mm, and above, and is only significant for values of $h = 0.78$ mm. Further, Figure 3.22 reveals that, after correcting for this extra plastic-energy dissipation associated with bending in the adhesive layer for the wedge-peel test with $h = 0.78$ mm, then firstly the effect of the wedge thickness, D_w, vanishes. Secondly, the adhesive fracture energy, G_a, as a function of the thickness of the adhesive layer, h_{adh}, relationship for the $h = 0.78$ mm wedge-peel test is now in good agreement with the behaviour predicted for such tests with thicker adherend arms.

3.4.6. Concluding comments on the constraint effects

Figure 3.23 shows the numerically-predicted values of the adhesive fracture energy, G_a, as a function of the adhesive layer thickness, h_{adh}, for the LEFM TDCB and EPFM wedge-peel test configurations discussed in Sections 3.4.4 and 3.4.5. (For the wedge-peel test specimen with adherend arms of h = 0.78 mm, the values have been corrected for bending, as discussed above.) Figure 3.23 also includes the G_a values that were obtained experimentally from the TDCB test specimens using aluminium-alloy adherends, which failed close to the centreline of the adhesive layer; see also Figure 3.9(b) and Table 2.2. Several noteworthy points arise. Firstly, there is an extensive body of literature which establishes the dependence of G_a, as a function of h_{adh}, see for example Kinloch (1987). The same trends are, as expected, seen in the present work both from (a) the experimental studies, see Figures 3.9(a) and 3.9(b) and Table 2.2, and (b) the predicted modelling studies, see Figures 3.9(a) and 3.9(b), Figures 3.14 and 3.14(b), Figure 3.18(a), Figure 3.19 and Figures 3.21 to 3.23. Secondly, as commented previously, for the TDCB test, the numerical values of G_a predict quite well the variation of G_a with h_{adh}, that was observed experimentally, namely a steady increase up to a plateau value after passing through a small local peak at an intermediate thickness of $h_{adh} \cong 0.40$ mm. Thirdly, from Figure 3.23, all the numerically-predicted values of G_a , for a given

[6] The adhesive behaves plastically and, hence, non-linearly at crack tip so that the principle of superposition does not apply. The total energy cannot therefore rigorously be evaluated as the sum of the energy expended in bending in the absence of a crack tip and at the crack tip in the absence of bending.

value of h_{adh}, vary by only about $\pm$20 J/m^2 (i.e. a coefficient of variation of about $\pm$10%) for the two types of test specimen and the various test configurations. Fourthly, Figure 3.23 reveals that this variation is of the same order of magnitude as the scatter measured when determining the values of G_a experimentally. Therefore, fifthly, the modelling studies predict no statistically significant differences will be observed in the experimentally-measured G_a values, for a given value of the thickness of the adhesive layer, h_{adh}, associated with the different test specimens and other aspects of the test configurations.

The above conclusions support the hypothesis of considering the measured value of the adhesive fracture energy, G_a, as a 'characteristic material property' of the adhesive joint, for a given thickness of the adhesive layer h_{adh}. Indeed, the independence of the value of G_a upon the type of test specimen, or upon the choice of adherend material, when the locus of joint is cohesive through the adhesive layer, has been previously observed experimentally for a relatively tough adhesive by Blackman et al. (2003c) and by Kawashita et al. (2008).

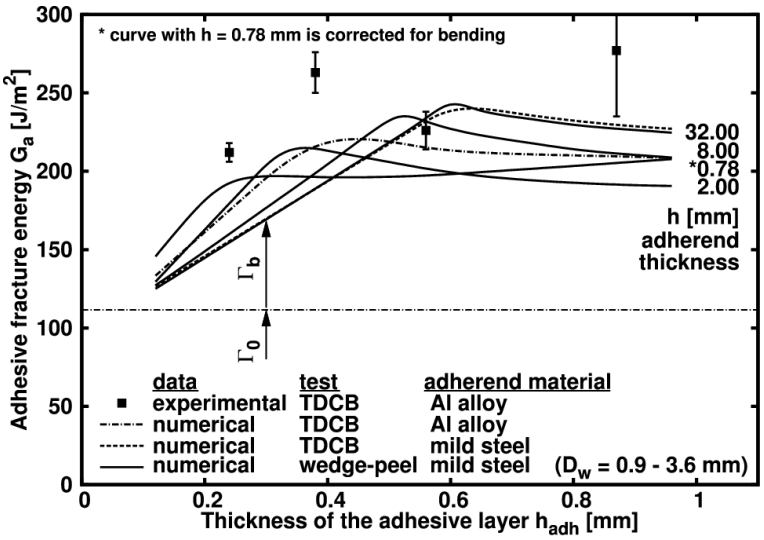

Figure 3.23: The predicted adhesive fracture energy, G_a, as a function of the thickness of the adhesive layer, h_{adh}, for the different test specimens and test configurations; and compared with the experimental values obtained from the LEFM TDCB test specimens using aluminium-alloy adherends

3.5. Application to the adhesive 'ESP 110'

Since the AACZ model was shown in Section 3.4 to give, for a first particular adhesive 'Betamate 73455' and with constant material parameter values, quite accurate numerical predictions over a large range of specimens geometries and types of tests, the goal that is pursued in the present Section is to see whether:

- that model model can give equally good predictions on a quite different adhesive, namely the adhesive 'ESP 110', exhibiting adhesive fracture energies roughly ten times larger;
- the understanding gained in the previous Section about the dissipation mechanisms affecting the adhesive fracture energy are of general nature and can be of any use to the other adhesive being considered here.

3.5.1. Identification of the material parameters

For the model to be representative of the adhesive/adherend system under consideration, suitable values for the material parameters must be identified. These parameters characterize the bulk behaviour of both the adhesive and adherend materials, and the local fracture process within the adhesive. As noted in Section 3.4.1, the bulk behaviour of the materials is modelled using isotropic J_2 theory of plasticity. The corresponding material parameters consist of the elastic properties (i.e. the Young's modulus, E, and Poisson's ratio, ν), a mathematical expression for the hardening law and the associated coefficients. With the exception of Poisson's ratio, they are all derived by least-square fitting, in the small-strain range (i.e. $\varepsilon < 3\%$), the tensile stress versus strain curves presented in Chapter 2. The aluminum-alloy, 5754-O, curves are fitted separately for each sheet material thickness, with the following equation which makes use of the empirical hardening law of Ludwik:

$$\sigma = \begin{cases} E\varepsilon & (\varepsilon \le \sigma_0 / E) \\ \sigma_0 + h(\varepsilon - \dfrac{\sigma}{E})^n & (\varepsilon > \sigma_0 / E) \end{cases} . \tag{3.35}$$

The resulting fits are presented in Figure 3.24(a) and show good agreement with the experimental data, which supports the choice made for the expression for the hardening law. The tensile curves for the adhesive are fitted using the following equation:

$$\sigma = \begin{cases} E\varepsilon & (\varepsilon \le \sigma_0 / E) \\ \sigma_0 + h(\varepsilon - \dfrac{\sigma}{E})^n + k(\varepsilon - \dfrac{\sigma}{E}) & (\varepsilon > \sigma_0 / E) \end{cases} \tag{3.36}$$

Here, an additional term was added to Ludwik's hardening law in order to better match the experimental data, see Figure 3.24(b). The value of the Poisson's ratio could not be determined experimentally, since lateral contractions of the traction specimens were not measured in the tests. Therefore, it is taken to be equal to 0.40 and 0.33 for the adhesive and both aluminum alloys, respectively. These are typical values for such materials. All the bulk material properties are summarized in Table 3.2. It should be noted that the value of σ_0 for the adhesive is not representative of the yield stress of the material. It should be viewed as any other coefficient of the flow-law: its value is determined so as to give the best fit from a purely mathematical (i.e. a least-square regression analysis) point of view and it has no real physical meaning. The yield stress of the material which denotes the appearance of a significant amount of plastic deformation is best captured by the 0.2% yield limit which is equal to 36.7 MPa.

Table 3.2: Bulk material properties obtained by fitting the experimental stress versus strain curves

Material	***E* [GPa]**	***ν* [-]**	**σ_0 [MPa]**	***h* [MPa]**	***n* [-]**	***k* [MPa]**
AA 5754-O (1.00mm)	74.7	0.33	114	87.5	0.290	N/A
AA 5754-O (1.45mm)	79.5	0.33	112	107	0.257	N/A
ESP110	5.72	0.40	5	655	0.470	-1800

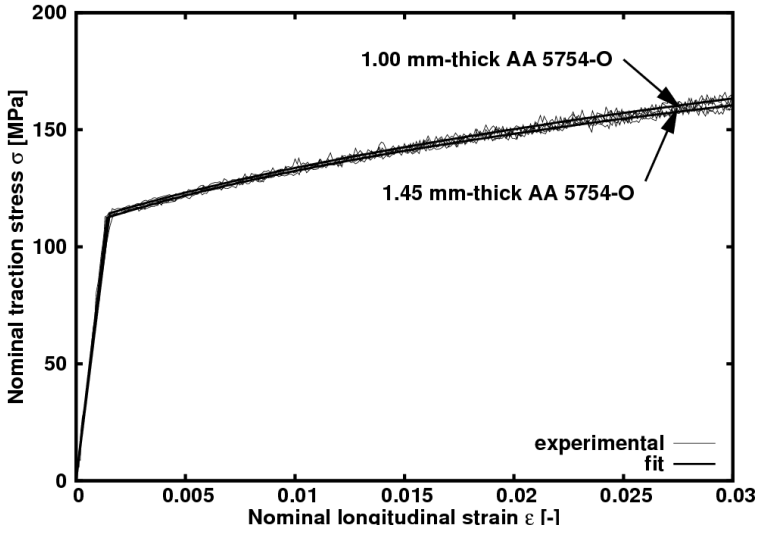

(a)

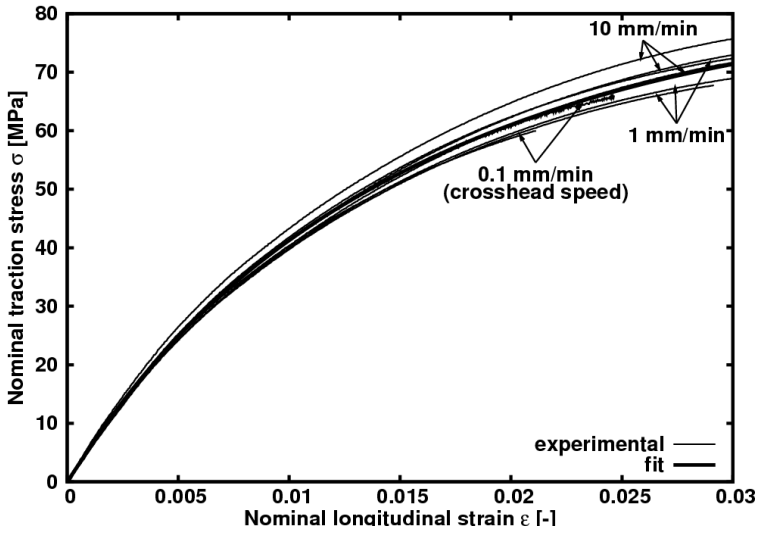

(b)

Figure 3.24: The experimental tensile stress versus strain curves and corresponding fitted models for (a) the adhesive 'ESP 110', and (b) the aluminium adherends used for the peel tests.

The local fracture process is modelled employing a cohesive zone described by two parameters: the critical opening displacement δ_c and the peak stress $\hat{\sigma}$. Currently, there is no clear method for inferring these microscopic scale parameters directly from experimental results, although some researchers have tried to address this issue either by developing specific bulk specimens (Ivankovic et al., 2004) or by

developing measurement techniques directly applicable to joint specimens (Andersson and Stigh, 2004). Hence, in the present work, these two parameters are determined by using an inverse analysis. Namely, their values are tuned to provide the best match with experimentally-measured, macroscopic, measurements obtained from a 'reference' test configuration. Three experimental values (a, R_1 and R_2) obtained from wedge-peel tests, with h_{adh} = 0.25 mm and h = 1.45 mm, were chosen as the reference test values to be used to ascertain these two parameters needed in the cohesive zone. (The peel test data are preferred to the TDCB test data because peel test are more widely used in industry. The wedge-peel test data are preferred to the fixed-arm peel test data to ascertain, and so fix, the values of these two parameters, since (i) an individual, single, test yields three (a,R_1,R_2) instead of two (P/b, R_0) experimental values, and (ii) because it is expected that the scatter is more likely to be reduced when using more numerous experimental-input values. Amongst the available wedge-peel test data, this particular specimen geometry was chosen (i) for its central position in terms of adhesive layer and adherend thickness, and (ii) because the corresponding experimental values show minimal scatter.) It should be noted that, by relying on only a single test configuration and a single specimen geometry to determine the values for these two parameters needed in the cohesive zone, it is intended to critically assess the predictions of the model when departing from these reference conditions, i.e. to examine the use of these values for the two parameters in modelling the other configurations of the wedge-peel test, as well as the fixed-arm peel tests.

From a numerical point of view, the two dimensional space of values (i.e. $\delta_c, \hat{\sigma}$) is coarsely spanned by letting each parameter vary in a range where the optimum is expected to be found. For each pair of values, the model of the wedge-peel test is used to predict the crack length and radii of curvature for the reference specimen geometry. The resulting discrepancy between numerical predictions and experimental values is evaluated quantitatively as an average, non-dimensional difference:

$$\phi = \frac{1}{3}\left(\left| \frac{a^{pred}}{a^{mes}} - 1 \right| + \left| \frac{R_1^{pred}}{R_1^{mes}} - 1 \right| + \left| \frac{R_2^{pred}}{R_2^{mes}} - 1 \right| \right) \tag{3.37}$$

where the superscripts *mes* and *pred* denote average experimental values and numerical predictions, respectively. Amongst all the pairs of parameters (i.e. $\delta_c, \hat{\sigma}$) envisaged, the one leading to the smallest discrepancy indicator is retained. The values of δ_c and $\hat{\sigma}$ are then perturbed and the model re-run iteratively until no further benefit can be achieved.

This optimization loop yielded the following values for the cohesive zone parameters:

$$\delta_c = 12.7\ 10^{-3}\ \text{mm} \qquad \text{and} \qquad \hat{\sigma} = 99\ \text{MPa}$$

which corresponds to an intrinsic work of fracture, Γ_0:

$$\Gamma_0 = 845\ \text{J/m}^2 .$$

When compared with the reference data, the numerical predictions all lie within the experimental scatter and show an average difference of $\pm$4.25%. More details on the comparison between the experimental data and numerical predictions will be given in the next Section.

3.5.2. Numerical results

3.5.2.1. Wedge-peel test

The model of the wedge-peel test was run for the three geometrical configurations which were tested experimentally and which were shown to fail under predominantly mode I conditions with some contribution of mode II. The corresponding results are presented, and compared with the experimental values, in Figures 3.25(a–c).

Overall the agreement is excellent, not only for the reference test (i.e. the wedge-pee test with h_{adh} = 0.25 mm and h = 1.45 mm) used for the identification of the two cohesive zone parameters $\hat{\sigma}$ and δ_c, but also for the other specimen configurations. The largest discrepancy is found for the wedge-peel test where h_{adh} = 0.40 mm and h = 1.45 mm, and is of the order of 10% for the difference between the predicted and measured crack lengths. For this particular wedge-peel test configuration, the model does seem to underestimate slightly the energy required to fracture the adhesive, since the predicted values for both the radius of curvature on the crack side and the crack length are somewhat larger than the experimental values.

Predicted values for the adhesive fracture energy, G_a, deduced from the wedge-peel test are given in Figure 3.25(d). They reveal no significant dependence upon the thickness of either the adherend or the adhesive. This observation may be explained by the fact that the main contribution to G_a comes from the local fracture process, i.e. Γ_0 which is the intrinsic work of fracture and is associated with the cohesive zone and which was assumed, in the model, to be a constant. (It should be noted that, for the present adhesive and loading configurations, a model based on a single row of cohesive elements for the entire adhesive layer, such as

proposed by Yang and co-workers (Yang et al., 1999), might therefore be sufficient to properly reproduce the experimental results.)

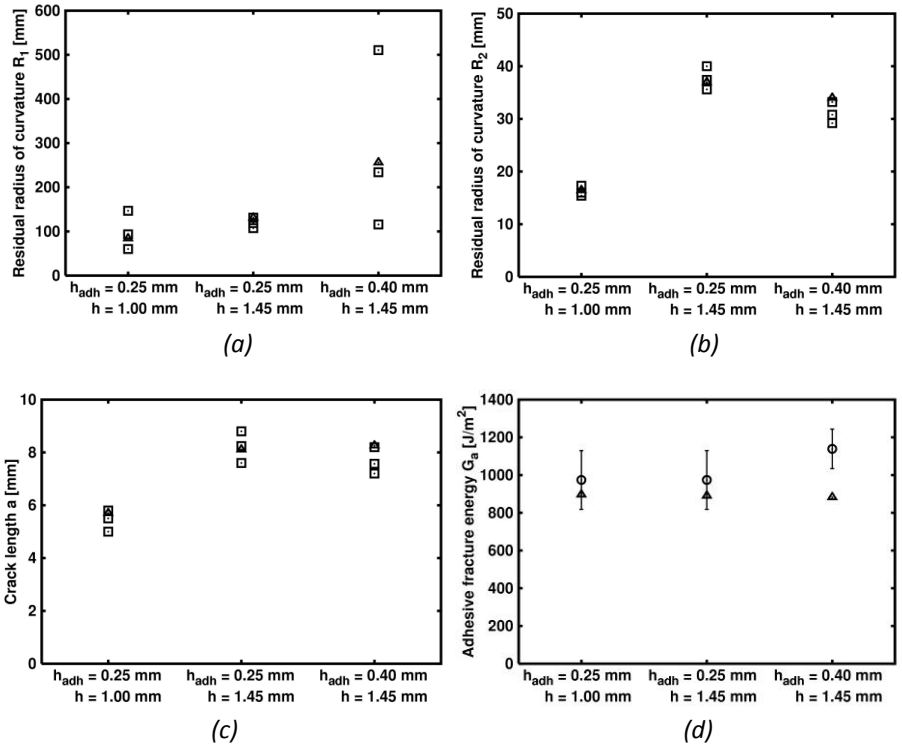

Figure 3.25: Comparison between experimental (□), if available, and numerical (△) values obtained for the wedge-peel test with D_w = 1.5 mm in terms of (a) the residual radius of curvature on the adhesive side, (b) the residual radius of curvature on the crack side, (c) the crack length and (d) the adhesive fracture energy. (In Figure 3.25(d) the values of G_a so determined are compared with the experimental LEFM TDCB values (○).)

For the sake of completeness, Figure 3.25(d) also includes values of G_a obtained by Kawashita et al. (2008) from linear-elastic fracture-mechanics (LEFM) tests using a tapered-double cantilever-beam (TDCB) method. In these experiments, the failure was quasi pure mode I since the locus of joint failure was cohesive through the centre of the adhesive layer. Good agreement may be seen between the LEFM TDCB values for G_a and the numerically-determined wedge-peel values for G_a, especially for the specimens with h_{adh} = 0.25 mm. This observation further supports

the idea that the value of the adhesive fracture energy, G_a, is independent upon the test configuration. However, the predicted value of G_a from the wedge-peel test for h_{adh} = 0.40 mm appears to be somewhat lower than the LEFM value. This observation may arise from the observation that the locus of joint failure was close to an adhesive/adherend interface for the wedge-peel test but in the centre of the adhesive layer for the LEFM TDCB test.

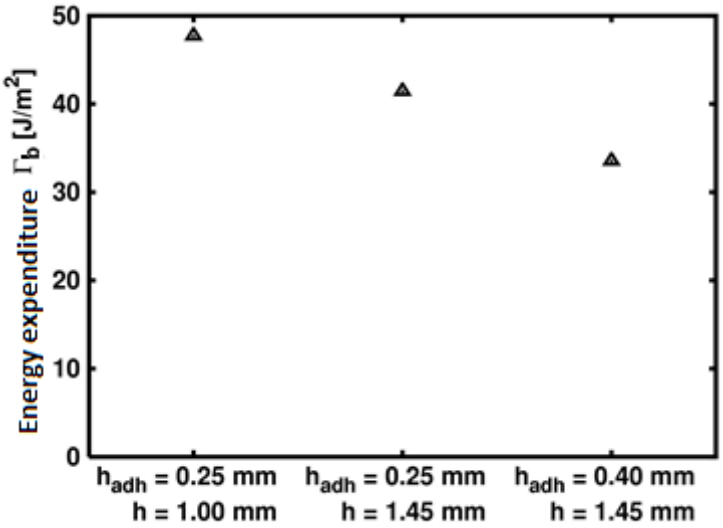

Figure 3.26: Energy expenditure in the bulk adhesive as predicted by the model of the wedge-peel test with D_w = 1.5 mm

Now, the energy expenditure in the bulk adhesive, Γ_b, in the adhesive layer appears, therefore, to only have a second-order effect on the value of the adhesive fracture energy, G_a. The evolution of Γ_b as a function of the specimen geometry in the wedge-peel test is plotted in Figure 3.26. To help understand this evolution, the zones of active plasticity in the adhesive layer are plotted in Figure 3.27 since plastic dissipation is expected from the results of the previous Section to be the main contributor to Γ_b.

They are defined as the regions where plastic dissipation occurs above the initial 0.2% yield strength of the material, which mathematically may be stated by:

$$\begin{cases} \dot{p} > 0 \\ \overline{\sigma} > \sigma_0^{0.2\%} \end{cases} \tag{3.38}$$

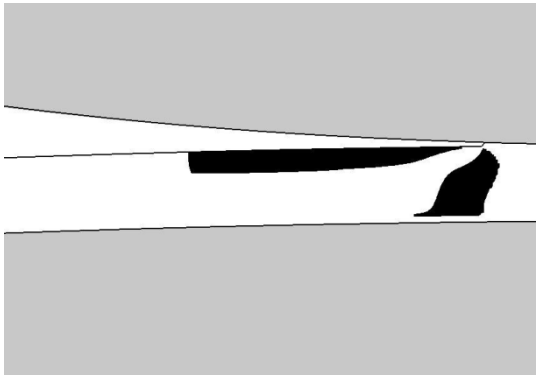

(a)

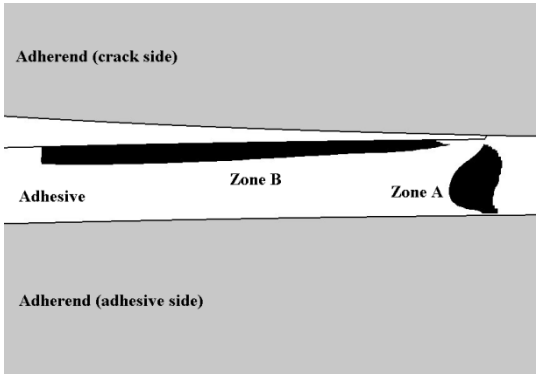

(b)

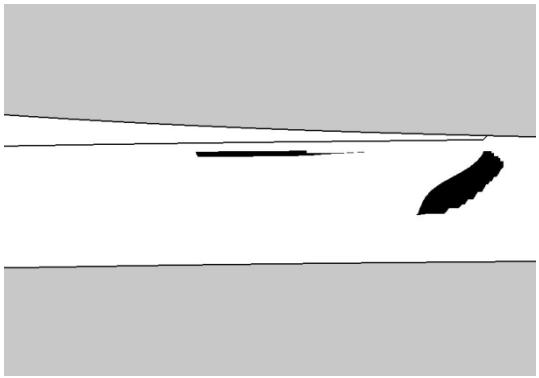

(c)

Figure 3.27: Zones of active plasticity in the adhesive obtained in the wedge-peel test with (a) h_{adh} = 0.25 mm and h = 1.00 mm, (b) h_{adh} = 0.25 mm and h = 1.45 mm, and (c) h_{adh} = 0.40 mm and h = 1.45 mm

They give a simpler, binary view of the plastic dissipation in the adhesive compared to the plots in Figure 3.15. Firstly, considering Figure 3.27(b) which corresponds to h_{adh} = 0.25 mm and h = 1.45 mm, the zones A and B identified in the previous Section are recovered. Secondly, considering Figure 3.27(a), which is for h_{adh} = 0.25 mm and h = 1.00 mm, an explanation can now be offered for the corresponding increase in Γ_b, see Figure 3.26: zone C seems to appear and to merge with zone A. Thirdly, Figure 3.27(c) shows that much less plastic dissipation occurs in the adhesive layer of this wedge-peel test configuration, as reflected in the lower values of Γ_b, see Figure 3.26. Compared with Figure 3.27(b), Zone A shrinks towards the crack tip and does not now extend over the full thickness of the adhesive layer which would tend to show, based on the results of the previous Section, that we are past the peak associated with zone C vanishing.

3.5.2.2. Fixed-arm peel test

The model of the fixed-arm peel test was run employing the specimen geometry, with h_{adh} = 0.40 mm, and the peel angles used in the experiments, as described previously. The predicted peel force per unit width, P/b, is obtained directly from the present model. The maximum curvature, $1/R_0$, of the peel arm is also obtained from the present numerical model, employing the smoothing and fitting methodology suggested by Kawashita et al. (2005), based on the position, in the deformed geometry, of the nodes located at the edge of the peel arm.

The numerically-predicted results for the peel strength, P/b, and radius of curvature of the peel arm, R_o, are compared with their experimental counterparts in Figures 3.28(a–b), and the numerically-predicted values are generally lower than the experimental measurements. In terms of the peel force, this discrepancy is negligible for a peel angle of 135^o but increases with decreasing peel angles to reach a 12% difference at a 45^o peel angle; whereas the values of R_0 are all about 25–35% below the experimental values, regardless of the peel angle. These differences are considered to arise from an artifact caused by the assumption made in the modelling concerning the segment of the peel arm transmitting the force to the steady-state window of interest. (It will be recalled that it was assumed that this external arm was behaving elastically, while it was recognized it had actually undergone some plastic deformation. It is thus less compliant in the model than it should be and induces, for a given peel force, a larger bending moment at the crack tip. As a consequence, the predicted peel force and minimum radius of curvature of the peel arm are predicted to be relatively low in value). For increasing values of the peel angle, the bending moment-to-peel force ratio at steady-state crack growth increases. Thus, the differences between the experimental and numerically predicted values are decreased for the peel force, but more pronounced for the bending moment or, equivalently, the minimum radius of curvature analysis. These

observations clearly demand an improvement in the way the boundary conditions are applied in the present model.

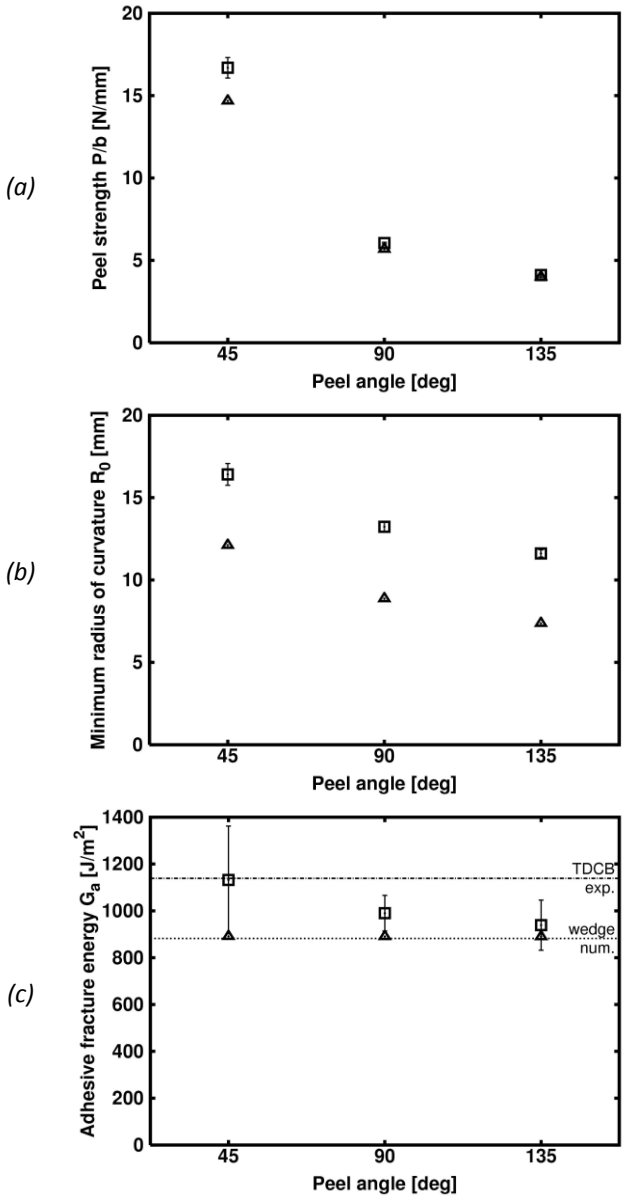

Figure 3.28: Comparison between experimental (□), or analytical in the case of the adhesive fracture energy, Ga, and numerical (△) values obtained in the fixed-arm peel test, for specimens with hadh = 0.40 mm and h = 1.00 mm, in terms of (a) the peel strength,(b) the minimum radius of curvature and (c) the adhesive fracture energy.

Now considering the adhesive fracture energy, G_a, it was derived numerically from Equations (3.18) and (3.20) by integrating from the inlet section, where the strain energy is zero, down to the outlet section where the peel arm shows zero curvature. These numerically-predicted G_a values obtained from the present work are compared in Figure 3.28(c) with the corresponding values of G_a which were calculated from the measured peel force per unit width, *P/b*, using the analytical model (Kinloch et al., 1994; Georgiou et al., 2003). The agreement between the two approaches is encouraging. Especially, since it should be noted that the analytical model does make several approximations, but is relatively easy to apply in order to derive values of G_a. Indeed, it appears that the numerically-predicted values do give values of G_a which are independent of the peel angle, whilst the analytically-derived values do show a small dependence of G_a upon the peel angle. Figure 3.28(c) also includes, as horizontal lines, corresponding to G_a values obtained experimentally from the LEFM TDCB (with h_{adh} = 0.40 mm) specimens and numerically from the model of the wedge-peel test (with h_{adh} = 0.40 mm and h = 1.45 mm), see Figure 3.25(d). Now, the numerically-predicted values of the G_a from the fixed-arm peel test are also in good agreement with the wedge-peel test values shown earlier in Figure 3.25(d). However, the values of G_a from the model proposed in the present work from both the wedge-peel and fixed-arm tests are somewhat lower than the values ascertained using the LEFM TDCB test specimen. It is difficult to state whether this is simply due to the predicted values from these two peel test configurations obviously being dependent upon the assumptions of the present model and/or from the accuracy of the fitted input data. Alternatively, the observation that the LEFM TDCB tests failed under quasi pure mode I conditions by crack growth through the centre of the adhesive layer, whereas the fixed-arm and wedge-peel tests failed with some contribution of mode II by a cohesive fracture through the adhesive layer, but near one adhesive/adherend interface, might be of significance.

Notwithstanding, the accuracy of the present model applied to the problem of elastic-plastic peel test configurations should not be underestimated. The values of adhesive fracture energy, G_a, deduced from the numerical simulations proposed in the present paper, from all the various elastic-plastic peel test configurations, lie in the range of about 900 $\pm$ 50 J/m^2; whilst the values from a previous analytical model (Kawashita et al., 2008) and a node-release finite-element analysis model (Hadavinia et al., 2006), for a cohesive fracture of this adhesive, all lie in the range of about 1100 $\pm$ 250 J/m^2. Thus, there is very good agreement between the different modelling methods. These values are clearly also in good agreement with the corresponding value from the well-established LEFM TDCB method of 1140 $\pm$ 170 J/m^2, for h_{adh} = 0.40 mm.

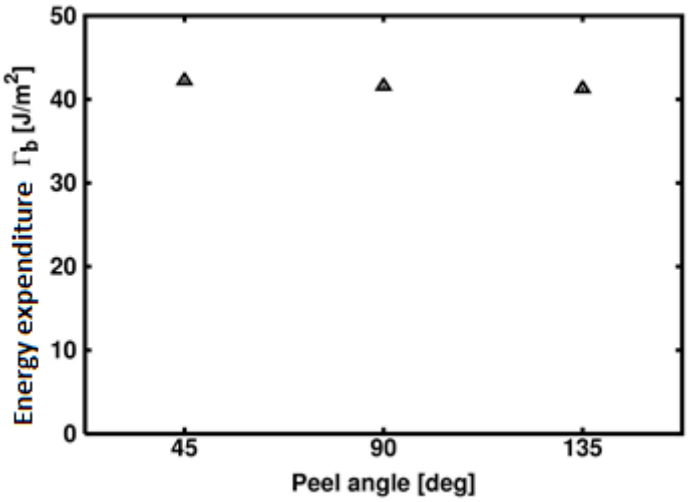

Figure 3.29: Energy expenditure in the bulk adhesive as predicted by the model of the fixed-arm peel test, for specimens with hadh = 0.40 mm and h = 1.00 mm

As far as the plastic dissipation, Γ_b, in the adhesive layer is concerned, again it is found to have a second-order effect on the value of the adhesive fracture energy, G_a. The evolution of Γ_b as a function of the peel angle in the fixed-arm peel test, for specimens with h_{adh} = 0.40 mm and h = 1.00 mm, is plotted in Figure 3.29. The different values of Γ_b are in excellent agreement, no matter the peel angle. Therefore, the value of the adhesive fracture energy, G_a, is, in the case of the fixed-arm peel test, independent of the peel angle. The only contribution to the overall energy expenditure that is significantly affected by the peel angle is the plastic dissipation in the flexible arm which, as reminder, is not included here in the calculation of G_a. These results are in agreement with the findings made, among others, by Guiu and Shanahan (2002).

The zones of active plasticity in the 0.40 mm thick adhesive layer are plotted in Figure 3.30 for the fixed-arm peel test for the three peel angles considered. These zones all appear to be very similar, as would be expected since the predicted Γ_b values are not significantly different. Nevertheless, it should be noted that the assumption that Mode II (in-plane shear) does not play a significant role certainly reduces the possibility of any extra plastic dissipation which might be dependent on the peel angle. Further, comparing Figure 3.30 with Figure 3.27, where the latter figure shows the zones of active plasticity under wedge-peel test conditions, then two important effects may be observed. Firstly, Zone B becomes non-existent in

the fixed-arm peel test because the adhesive adheres to an infinitely rigid foundation that does not bend. Secondly, on the other hand, considering Zone A, the bending stresses occurring in the adhesive layer in wedge-peel test tend to push Zone A past the crack tip and so reduce its extent.

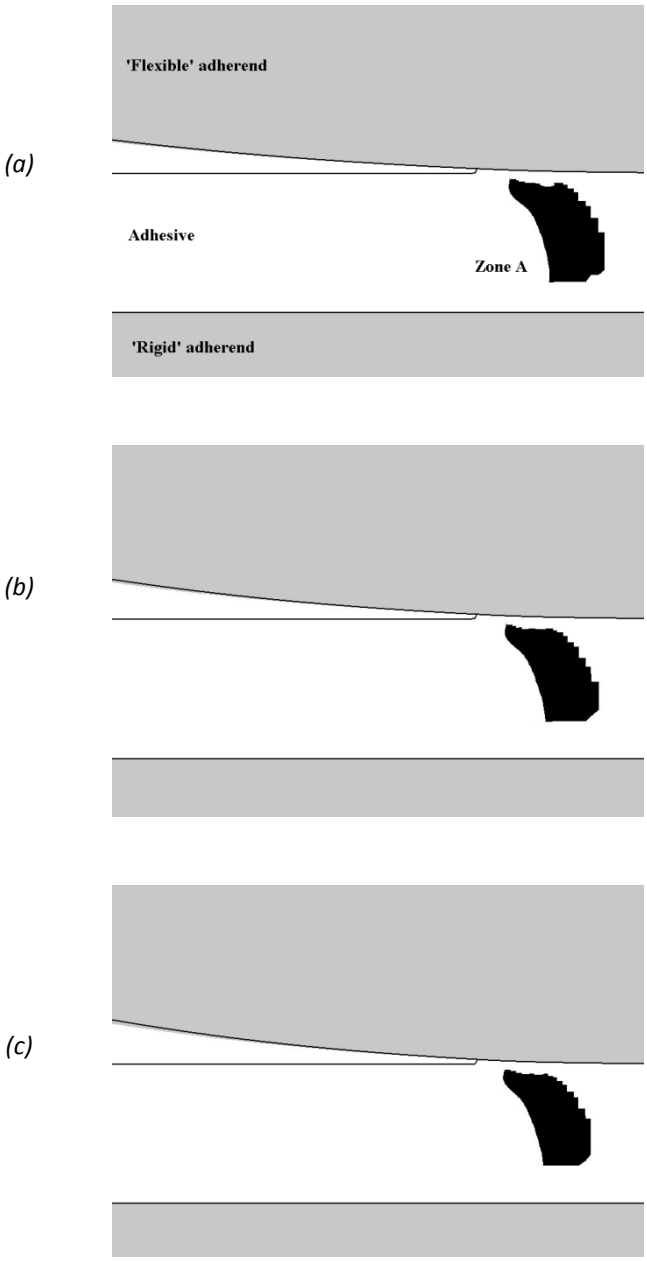

Figure 3.30: Zones of active plasticity in the adhesive obtained in the fixed-arm peel test with a peel angle of (a) 45 degrees, (b) 90 degrees and (c) 135 degrees

3.5.2.3. Tapered double cantilever beam test

Figure 3.31 shows a comparison between the experimental values of the adhesive fracture energy that were measured from the LEFM TDCB test specimens made using the adhesive 'ESP 110' (see Table 2.5) and the numerical predictions that were obtained with the model. Although the agreement is reasonably good for the range of adhesive layer thickness as used for Figure 3.25, the numerical predictions largely underestimate the experimental values of G_a as the thickness of the adhesive layer is increased above that range. Figure 3.31 also shows that as the energy, Γ_0, expended in the cohesive zone is kept constant, the energy expenditure in the adhesive, Γ_b, which is added to Γ_0 to give the adhesive fracture energy, G_a, hardly increases with the adhesive layer thickness, h_{adh}. Thus, the numerical predictions cannot follow the increase in G_a that is observed experimentally.

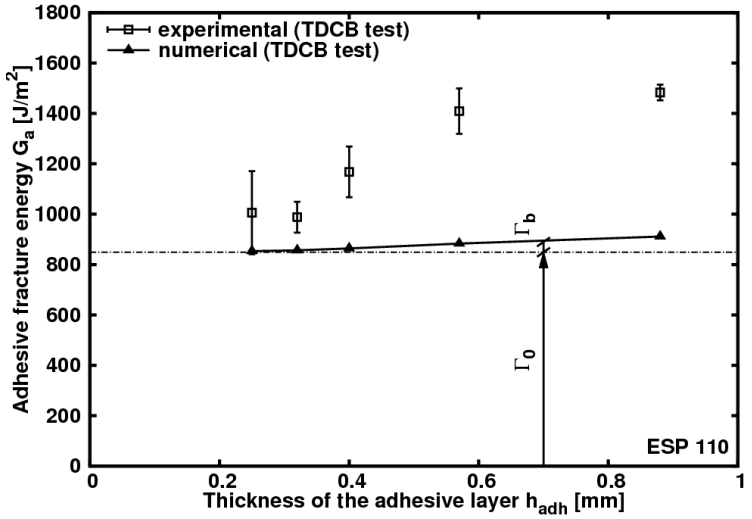

Figure 3.31: Comparison between the experimental data and the numerical predictions for the adhesive 'ESP 110' obtained from the TDCB test

The explanation for these observations may be found in Figure 3.32 which was reproduced from Tvergaard and Hutchinson (1992) who calculated the steady-state toughness of elastic-plastic solids. As in the present model, they employed continuum elements with an embedded cohesive zone model with zero thickness. Figure 3.32 shows that, with the material parameters used here of $\hat{\sigma}/\sigma_{0.2}\sim 3$, $\Gamma_0\sim 800$ J/m² and $n\sim 0.2$, the energy expenditure in the bulk of the adhesive, Γ_b, that can be expected is of the order of $0.2\ \Gamma_0\sim 160$ J/m² as observed in Figure 3.31. In other words, for the hardening exponent characterising the adhesive 'ESP 110',

the value of the peak stress, $\hat{\sigma}$, that was used is not high enough to generate sufficient plastic dissipation in the adhesive. Thus, the increase in the adhesive fracture energy that is observed experimentally from $h_{adh} = 0.32$ to 0.88 mm cannot be predicted from the AACZ model with the cohesive zone parameters values identified above.

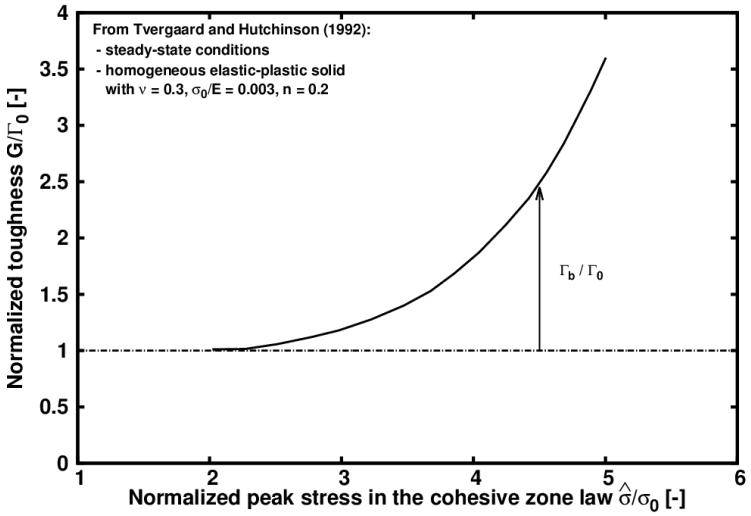

Figure 3.32: The normalized steady-state toughness of an homogeneous elastic-plastic solid predicted by Tvergaard and Hutchinson (1992), as a function of the peak stress in the cohesive zone law

An attempt was made to see whether by using larger values of $\hat{\sigma}$, it was possible to reproduce the experimental results for $h_{adh} = 0.32$ to 0.88 mm. The value of $\hat{\sigma}$ was progressively increased and the value of Γ_0 adapted accordingly for the model to reproduce exactly the experimentally measured value of the adhesive fracture energy at an adhesive layer thickness of $h_{adh} = 0.32$ mm. Each of these pair of values $(\hat{\sigma}, \Gamma_0)$ were then used in the model to calculate the adhesive fracture energy at an adhesive layer thickness of $h_{adh} = 0.88$ mm. The resulting change of the adhesive fracture energy as a function of the peak stress $\hat{\sigma}$ is shown in Figure 3.33. It can be seen that it is not possible with the present AACZ model to reproduce numerically the increase in the adhesive fracture energy that is measured experimentally, regardless of the value of $\hat{\sigma}$ selected. Indeed, as $\hat{\sigma}$ is increased, Γ_b does increase but the value of Γ_0 decreases at the same time so as to be consistent with the value of G_a at $h_{adh} = 0.32$ mm. Hence, overall, the value of G_a at $h_{adh} = 0.88$ mm is not significantly increased.

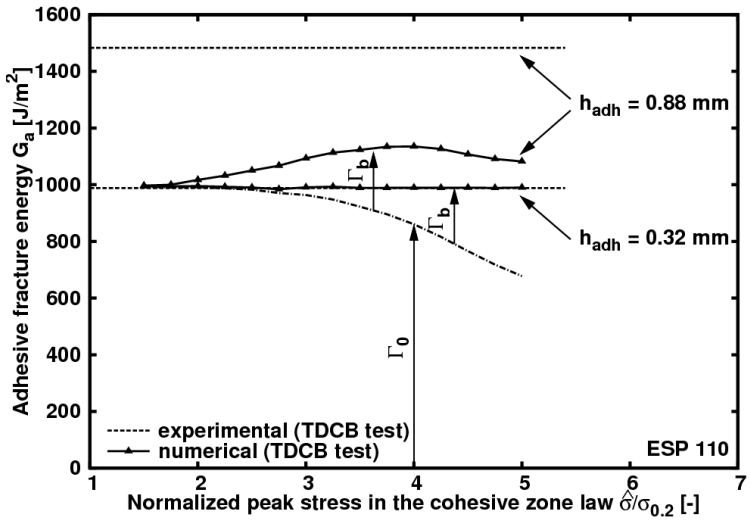

Figure 3.33: The values of the adhesive fracture energy predicted at an adhesive layer thickness equal to $h_{adh} = 0.88$ mm when letting the peak stress in the cohesive zone vary and modifying the value of Γ_0 accordingly to reproduce numerically the value of the adhesive fracture energy that was measured experimentally at an adhesive layer thickness of $h_{adh} = 0.32$ mm

3.5.3. Concluding comments

The AACZ model, used with constant cohesive zone parameters to model the adhesive 'ESP 110', shows a great potential for giving accurate numerical predictions as the type of test or the thickness of the adherends are modified, providing the thickness of the adhesive layer is reasonably kept unchanged. However, it fails to predict accurately, the effect of an increase of the thickness of the adhesive layer to the contrary of what was observed in Section 3.4 with the adhesive 'Betamate 73455'. The reason behind is that the energy expenditure in the bulk adhesive, Γ_b, which is the only term in the model that can render an increase of the adhesive fracture energy as a function of the adhesive layer thickness was only yielding a negligible contribution. The magnitude of this contribution could be increased significantly by increasing the peak stress, $\hat{\sigma}$, in the cohesive elements but, even then, Γ_b was not varying sufficiently with the thickness of the adhesive layer to match with the experimental results.

3.6. Conclusions on the AACZ model

Regardless of the adhesive material being considered, the AACZ model appears to be yielding accurate numerical predictions, with constant cohesive zone parameters, as long as the thickness of the adhesive layer remains reasonably the same. More particularly, it is capable of reproducing the effect of the type of test, of the adherend material and of the adherend thickness.

The AACZ model is also capable of reproducing reasonably well the effect of the thickness of the adhesive layer over a large range of thicknesses but not with all adhesives. More particularly, for given elastic-plastic properties of the bulk adhesive, there seems to be a limit to the maximum increase of the adhesive fracture energy that can be reproduced by the AACZ model. As a consequence, the AACZ model seems to be better suited for low-toughness adhesives such as the adhesive 'Betamate 73455' than for rubber-modified expoy-based systems such as the adhesive 'ESP 110'.

For the latter systems, it is expected that the limiting factor comes from keeping the cohesive zone parameters constant. Indeed, it is anticipated that the damage mechanisms responsible for fracture are dependent upon the stress triaxiality level, and hence require a constraint dependent value of Γ_0 as already discussed in the literature in the context of ductile failure of metals, e.g. Tvergaard and Hutchinson (1996), Siegmund and Brocks (1998), Pardoen et al. (1999), and recently by McAuliffe et al. (2011) for adhesive bonds.

Chapter 4
The MPS model

4.1. About the model

4.1.1. Fundamentals

It was shown in Chapter 3 that for the tougher 'ESP 110' adhesive the use of the AACZ model employing constant material parameters is only successful at predicting the variation of adhesive fracture energy, G_a, as a function of the adhesive thickness, h_{adh}, for relatively narrow ranges of h_{adh} values. A tentative explanation for that limitation is that the damage mechanisms represented by the cohesive zone actually depend upon the thickness of the adhesive layer through the level of constraint ahead of the crack tip and, more particularly, the stress triaxiality as already illustrated in the case of metals (Siegmund and Brocks, 1999; Pardoen at al., 2004). A possible solution would be to modify the cohesive zone parameter values as a function of the stress triaxiality as suggested by Cooper et al. (2012). However, this requires performing multiple experiments to get the dependence of the cohesive zone parameters upon the stress triaxiality (Cooper et al., 2012). Therefore, a better solution is to explore a model that would inherently take into account the effect of the level of constraint. The first attempt that was made consisted in considering that the failure was occurring by the initiation and subsequent growth of cavities. This mechanism was modelled with an uncoupled damage approach, considering different criteria for the initiation of voids and the Rice and Tracey (1969) equation for their subsequent growth. The numerical results obtained with that methodology showed that the initiation of the voids was dominating the fracture process. It was hence decided to explore in the present Chapter the initiation of voids by the debonding, the cleavage or the cavitation of the second-phase particles as the condition for failure and to test that approach against three different adhesives.

The particular failure criterion that is used requires the maximum principal stress to reach a critical value, σ_c, at a critical distance, r_c, ahead of the crack tip: the values of σ_c and r_c being characteristic and constant for a given adhesive. The present model will hence be referred to as the MPS model (Maximum Principal Stress). The ideas behind that formulation are: (i) that void nucleation occurs when the maximum principal stress in the particle or at its boundary reaches a critical value (a criterion commonly found in the metals community; see Pardoen and Pineau, 2007), and, (ii) that the latter occurs when the remote or macroscopic maximum principal stress itself is above a value equal to σ_c at distance, equal to r_c, with respect to the size of the particle[7]. This model belongs to the theory of critical distances, following the terminology of Taylor (2008), that has been widely used under different variants both for metals and adhesives. Of relevance to the present model are the work of Ritchie et al. (1973), who suggested that the fracture of brittle metals by cleavage occurs when the opening stress reaches a critical value at a given distance ahead of the crack tip, as well as the later work of Clarke and McGregor (1993) and Crocombe et al. (1995) who used more or less successfully different stress components or invariants, at a certain distance or averaged over a certain distance, to predict the onset of failure from either non-cracked or cracked adhesive joints.

The present study focuses on conditions of quasi-static, steady-state crack propagation in the adhesive. To calculate efficiently, from the computational point-of-view, the stresses ahead of a crack propagating under steady-state conditions, the dedicated 2D plane-strain, large deformation, quasi-static, steady-state finite element code already presented in Chapter 3 was used. Plane-strain conditions were chosen due to the large width-to-thickness ratios exhibited by the specimens being studied. A formulation accounting for large deformation was necessary because of the large rotations that the peel arms of the wedge-peel test specimens could show. Inertia effects were neglected based on the low loading rates being considered in the present study. Finally, a steady-state formulation was chosen, for the sake of computational efficiency, since it makes it possible to search directly, in an iterative process, for the steady-state solution and hence use optimal meshes, tuned for the steady-state solution of interest. In contrast, traditional transient schemes require propagating the crack over a sufficiently large number of time-steps, or equivalently, over a sufficiently large distance with respect to the thickness of the adhesive layer, until steady-state conditions are attained and, hence, rely on very refined meshes over the full range of crack tip locations that is

[7] It turned out in the simulation results that by imposing the maximum principal stress to be equal to σ_c at a distance to the crack tip equal to r_c, the maximum principal stress was actually larger than or equal to σ_c over the full distance r_c.

spanned which are much more computationally expensive. For the sake of completeness, it should however be mentioned the steady-state formulation suffers from a drawback which is that the definition of appropriate boundary conditions at the frontier of the computational domain is more complicated than in a transient formulation as already discussed in Chapter 3.

4.1.2. The wedge-peel test

The wedge-peel test was modelled as described previously in Chapter 3 to within the three differences or particularities listed below.

Firstly, the position of the crack was imposed, as an approximation, to be along the centreline of the specimens to simulate the tests conducted on the adhesives 'Betamate 73455' and 'Betamate 1493' in which the crack was running close to the centreline of the specimens, under quasi pure mode 1 conditions. To simulate the tests conducted on the adhesive 'ESP 110', in which the crack was running close to one of the adhesive/adherend interfaces with some amount of mode II, the crack position was located at a distance of 25 µm (i.e. 5-10% of the adhesive layer thickness) to the adhesive/adherend interface. (Note, for comparison purposes, that Kawashita et al. (2008) measured a residual adhesive thickness of 65 µm on similar specimens tested in the fixed-arm peel test.)

Secondly, to the contrary of the model described in Chapter 3, the present model does not include any cohesive zone. As a consequence, the nodes facing each other on both sides of the crack plane were rigidly tied together ahead of the crack tip by imposing the following multi-point constraints:

$$\begin{cases} u_1^J - u_1^I = 0 \\ u_2^J - u_2^I = 0 \end{cases} \tag{4.1}$$

When imposing the position of the crack to lie along the centreline of the specimen, the problem becomes symmetric and the size of the problem can be reduced by modelling only the upper symmetrical half of the specimen. In that case, the nodes tightening conditions given in Equation (4.1) becomes the simple displacement boundary condition given in Equation (4.2) below:

$$u_2^J = 0 \tag{4.2}$$

Thirdly, once found, the solution to the finite-element problem could be post-processed to calculate the adhesive fracture energy. The adhesive fracture energy, G_a, was numerically evaluated as the total external work per unit area of crack

advance, G_t, minus the total energy expended in the substrates per unit area of crack advance, G_s:

$$G_a = G_t - G_s \tag{4.3}$$

The total external work per unit area advance itself was obtained by multiplying the nodal forces imposed by the wedge by the local material velocity divided by the crack velocity $\dot{a}$:

$$G_t = F_i^A \frac{v_i^A}{\dot{a}} + F_i^B \frac{v_i^B}{\dot{a}} \tag{4.4}$$

which, making use of Equation (3.2) and realizing that the multi-point constraint in Equation (3.16) only introduces vertical forces, becomes:

$$G_t = -\left(F_2^A \left.\frac{\partial u_2}{\partial X_1}\right|_A + F_2^B \left.\frac{\partial u_2}{\partial X_1}\right|_B \right) \tag{4.5}$$

whereas the total energy expended in the substrates per unit area of crack advance, G_s, was obtained by integrating the material derivative of the strain energy density divided by the crack velocity $\dot{a}$, over the full thickness of both substrates (denoted by "s" in the formulae below), from the right boundary (located at $X_1 = X_1^u$) which is stress free down to location where $X_1 = X_1^d$ located anywhere in the portion of $l_{d,ext}$ where steady-state conditions prevail:

$$\begin{aligned} G_s &= \frac{1}{\dot{a}} \int_{X_1^d}^{X_1^u} \int_s \frac{DW}{Dt} dX_2 dX_1 \\ &= \frac{1}{\dot{a}} \int_{X_1^d}^{X_1^u} \int_s S_{ij} \left(\frac{\partial E_{ij}}{\partial t} + V_k \frac{\partial E_{ij}}{\partial X_k} \right) dX_2 dX_1 \end{aligned} \tag{4.6}$$

which, making use of the condition for steady-state regime ($\partial/\partial t = 0$) as well as of Equation (3.1), becomes:

$$G_s = -\int_{X_1^d}^{X_1^u} \int_s S_{ij} \frac{\partial E_{ij}}{\partial X_1} dX_2 dX_1 \tag{4.7}$$

The accuracy of the numerical predictions was verified, for every configuration that was simulated in the present study, by conducting rigorous convergence studies. More particularly, the lengths l_u and $l_{d,tot}$ were successively made longer and the element sizes made smaller until the variations observed in the predicted values of the crack length, the residual radius of curvature and the adhesive fracture energy became negligible. These studies showed that the element size at crack tip generally needed to be equal to 1/40 r_c or, depending on the thickness of the

adhesive layer, equal to 1/40 – 1/800 h_{adh} to get accurate results. Considering that the meshes that were used, then they were given element sizes that were progressively increased away from the crack tip with the aforementioned values resulted in meshes containing from 75 000 to 300 000 nodes which required total computational times ranging between 5 minutes and 20 minutes on 8 processors.

4.1.3. The TDCB test

Steady-state conditions do not rigorously apply to the TDCB test specimens, since the thickness of the arms at a right angle from the crack tip is constantly changing as the crack propagates. Nevertheless, as already explained in Chapter 3, the TDCB test can be modelled with an equivalent wedge-peel test which was done here. The details of the model and the post-processing operations are thus essentially the same as described in Section 4.1.2 for the wedge-peel test specimens, with the exception that for all the TDCB tests the crack location was along the centreline of the specimens.

4.1.4. Identification of the material parameters of the model

The different material properties that the model requires are: (i) the bulk elastic-plastic properties of the adherends (i.e. the Young's modulus, E_s, the Poisson ratio, υ_s, and the hardening law), the bulk elastic-plastic properties of the adhesive (i.e. the Young's modulus, E, the Poisson ratio, υ, and the hardening law) and the failure criterion for the adhesive (i.e. the maximum principal stress, σ_c, and the critical distance, r_c).

The aluminium-alloy grade (2014A) that was used to prepare the TDCB test specimens for the three adhesives was modelled as purely elastic, since no sign of plastic deformation could be observed in the actual tests (i.e. the adherends all returned to their initial shape after unloading). The values of its Young's modulus and Poisson ratio, taken from Hadavinia et al. (2006), are summarised in Table 4.1. The bulk elastic-plastic properties of all the other materials, also summarised in Table 4.1, were directly measured, with the exception of the Poisson ratio which was estimated from the literature.

The tensile stress-strain curve of the mild-steel that was used to prepare the wedge-peel test specimens for the adhesives 'Betamate 73455' and 'Betamate 1493' were already fitted in Section 3.4.1.1 with the following equation:

$$\sigma = \begin{cases} E\varepsilon & , \quad \varepsilon < \frac{\sigma_0}{E} \\ \sigma_0 \left(\frac{E\varepsilon}{\sigma_0}\right)^n & , \quad \varepsilon \geq \frac{\sigma_0}{E} \end{cases} \tag{4.8}$$

which includes a power-law type of hardening. The tensile stress-strain curves of the aluminium-alloy grade (5754-O) that was used to prepare the wedge-peel test specimens for the adhesive 'ESP 110' were already fitted in Section 3.5.1. with the following equation:

$$\sigma = \begin{cases} E\varepsilon & , \quad \varepsilon < \frac{\sigma_0}{E} \\ \sigma_0 \left[1 + \eta\left(\varepsilon - \frac{\sigma}{E}\right)\right]^n & , \quad \varepsilon \geq \frac{\sigma_0}{E} \end{cases} \tag{4.9}$$

which includes the Swift hardening law. The tensile stress-strain curves of the adhesive 'Betamate 73455' and of the adhesive 'ESP 110', were all also fitted with Equation (4.9) for consistency. The resulting fits, plotted in Figures 4.1 and 4.2, respectively, show reasonable agreement.

Table 4.1. Elastic(-plastic) properties used in the model

Material	Hardening law	E [GPa]	ν [-]	σ_0 [MPa]	η [-]	n [-]	$\sigma_{0.2}$ [MPa]
AA 2014A	-	72.4	0.33	-	-	-	-
AA 5754-O (1 mm)	Eq. (15)	74.7	0.33	114	87.5	0.29	-
AA 5754-O (1.45 mm)	Eq. (15)	79.5	0.33	112	107	0.257	-
Mild steel	Eq. (14)	210	0.30	124	-	0.14	-
Betamate 73455	Eq. (15)	6	0.45	13	87000	0.13	25.4
ESP 110	Eq. (15)	5.72	0.40	5.34	210000	0.32	36.9
Betamate 1493	Eq. (15)	1.8	0.45	20.4	19200	0.092	28.5

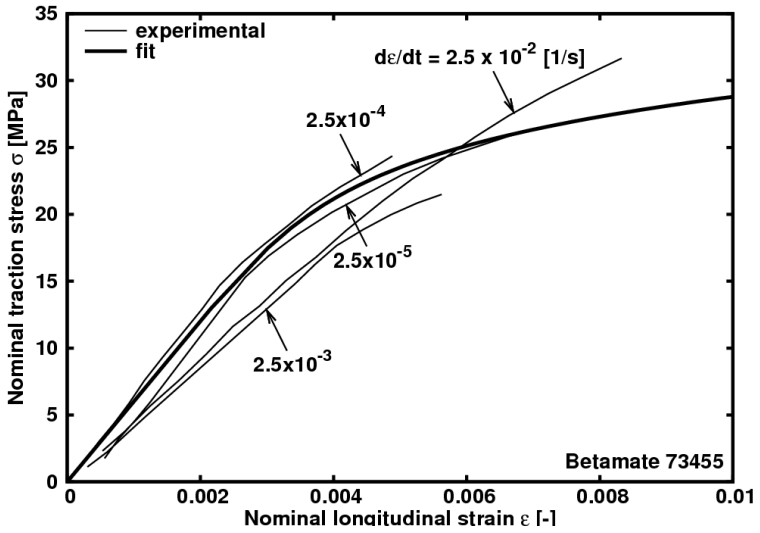

Figure 4.1: The experimental tensile stress versus strain curves and corresponding fitted model for the adhesive 'Betamate 73455'

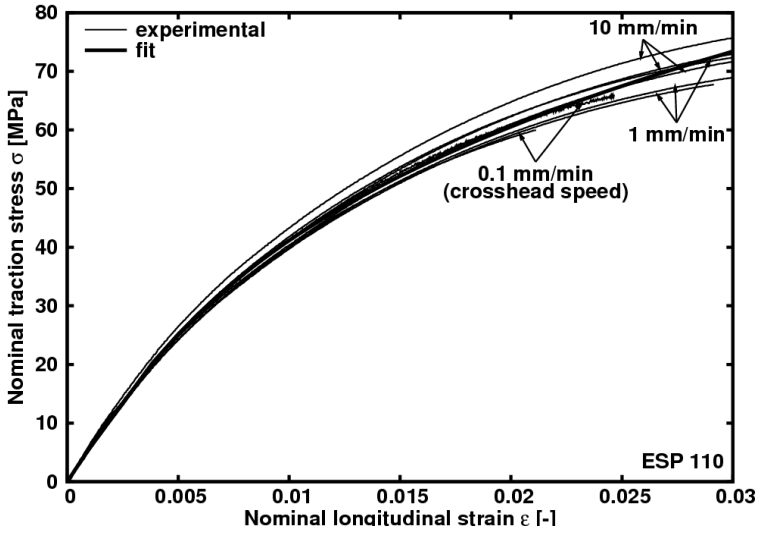

Figure 4.2: The experimental tensile stress versus strain curves and corresponding fitted model for the adhesive 'ESP 110'

The tensile stress-strain curves of the adhesive 'Betamate 1493' were not spanning the full range of strains that was expected to be spanned in the adhesive joints simulations due to the higher toughness values exhibited by the adhesive. Therefore, the compression stress-strain curve was fitted instead, also with Equation (4.9), and the resulting fit was scaled down, before being used in the model, to match with the tensile stress-strain curves[8]. Figure 4.3 shows the fit of the compression curve as well as the curve, scaled down to match with the tensile stress-strain curves, which was used in the model. Both show reasonable agreement. It should be mentioned that, owing to the large magnitude of the strains being considered for the adhesive 'Betamate 1493', the experimental data had to be translated from the nominal strain and stress measures to the Green-Lagrange strain measure and the second Piola-Kirchhoff stress measure before being fitted to match with the strain and stress measures used in the finite element code. The resulting fit was then back-translated to the nominal strain and stress measures before being plotted in Figure 4.3. It should also be mentioned that an attempt was made to fit the tensile stress-strain curves with a rate-dependent equation and to use the resulting fit in the model but this did not yield any significant worthwhile improvement in agreement between the numerical predictions and the experimental data.

As already discussed in Section 3.4.1 for the AACZ model, the differences observed in the yield behaviour of the adhesive in tension and in compression could have been taken into account in the model at the cost of some extra developments. However, this did not turn out to be necessary in view of the good agreement between numerical predictions and experimental data. The reason behind is supposed to be that in all the configurations being considered, the adhesive mainly yields in tension.

It should be noted that the value of σ_0 in Equation (4.9) which is reported in Table 4.1 is not representative of the yield stress of the adhesives, to the contrary of the value of σ_0 in Equation (4.8). It should be viewed in a similar manner as any other coefficient of the flow-law: its value is determined so as to give the best fit from a purely mathematical (i.e. a least-square regression analysis) point of view and it has no real physical meaning. To get comparable values of the yield stress between stress-strain curves fitted with Equation (4.8), that will serve as reference to conduct a parametric study later in the thesis, and Equation (4.9) it is advised to

[8] It is expected that the adhesive also shows some rehardening capabilities in tension at large strains. It thus seems reasonable to scale down the compression stress-strain curve, which shows some rehardening, to extrapolate the tensile stress-strain curves above the failure strain that was reached with the bulk tensile test specimens.

consider the value of σ_0 for the stress-strain curves fitted with Equation (4.8) and the 0.2% yield limit for the stress-strain curves fitted with Equation (4.9). The values of this 0.2% limit are reported for the three adhesives in Table 4.1 and, as would be expected, are more representative of the expected values of the yield stress than the values of σ_0 as can be seen in Figures 4.1, 4.2 and 4.3.

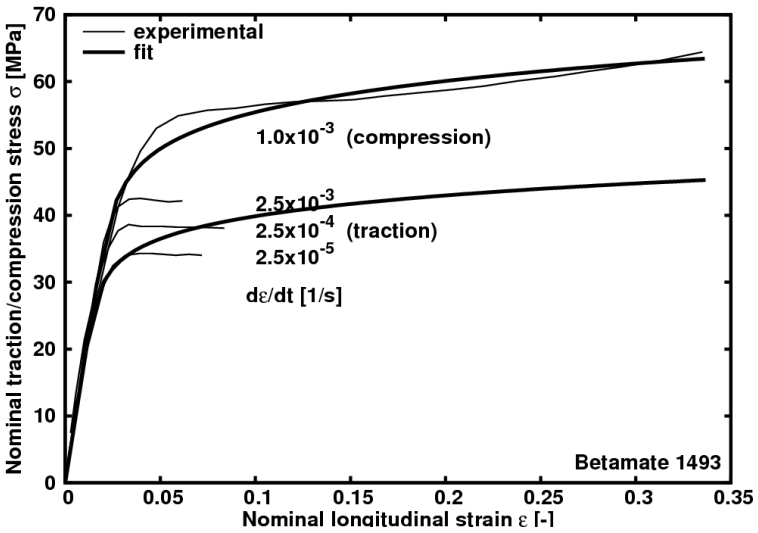

Figure 4.3: The experimental tensile and compression stress versus strain curves and corresponding fitted models for the adhesive 'Betamate 1493'

The material properties, r_c and σ_c, which constitute the failure criterion were identified, for each adhesive, by inverse analysis: their values were chosen so as to get the best possible agreement between the numerical predictions and the experimental data. Essentially, the EPFM wedge-peel and LEFM TDCB test configurations that were tested experimentally were simulated to reproduce the experimental measurements that had been obtained. In the wedge-peel test simulations, the crack length was chosen firstly so as to reproduce the minimum residual radius of curvature that had been measured and secondly so as to reproduce the maximum residual radius of curvature that had been measured. Similarly, in the TDCB test simulations, the load (or the wedge thickness in the equivalent wedge-peel test specimen) was chosen firstly to reproduce the minimum adhesive fracture energy that had been measured and secondly to reproduce the maximum adhesive fracture energy that had been measured. All the corresponding evolutions of the maximum principal stress as a function as the distance ahead of the crack tip were then plotted and the points (r_c, σ_c) were

searched for those that would be located between all the pairs of minimum and maximum curves pertaining to the different experimental (i.e. wedge-peel and TDCB) configurations tested. Figure 4.4 gives a simplified illustration of this procedure for the particular case of the adhesive 'ESP 110' in the sense that only two pairs of minimum and maximum curves are plotted: one for the TDCB test configuration corresponding to $h_{adh} = 0.32$ mm and one for the wedge-peel test configuration corresponding to $h_{adh} = 0.25$ mm and $h = 1$ mm.

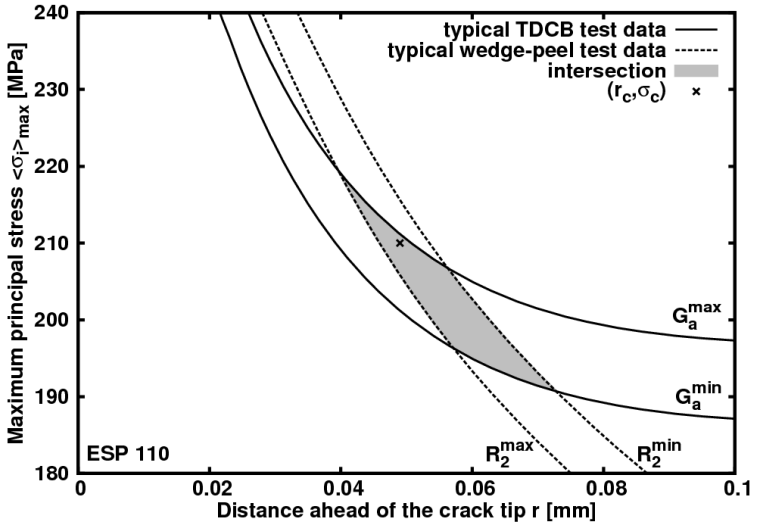

Figure 4.4: A schematic representation, for the particular case of the adhesive ESP 110, of the procedure that is followed to identify the material parameters (r_c, σ_c) *entering the failure criterion*

The values of r_c and σ_c obtained from this procedure are given in Table 4.2 with their range of uncertainty. For the adhesive 'ESP 110', there was a finite region of the (r_c, σ_c) space that was located between all the available pairs of minimum and maximum curves and the dimensions of this region determine the uncertainty on the values of r_c and σ_c. For the two other adhesives (i.e. 'Betamate 73455' and 'Betamate 1493'), it was not possible to find a finite region of the (r_c, σ_c) space that was located between all the available pairs of minimum and maximum curves. What could be found were different disconnected regions of the (r_c, σ_c) space that were located between most of the available pairs of minimum and maximum curves, with the exception of a few pairs that were different for each of these disconnected regions. The dimensions and the distance between these regions determine the uncertainty on the values of r_c and σ_c that is reported in Table 4.2.

Table 4.2. Failure properties used in the model

Material	r_c [µm]	σ_c [MPa]	$\sigma_c/\sigma_{0.2}$ $[-]$	G_a^{ref} [J/m²]	Particle size [µm]	Particle spacing [µm]
Betamate 73455	18 ± 3	98 ± 0.4	3.86	9.7	10-200	20-200
ESP 110	49 ± 3	210 ± 3.3	5.69	61.6	30-100	50-100
Betamate 1493	6.8 ± 1	141 ± 1.0	4.95	15.4	5-15	200

4.1.5. Physical interpretation of the parameters of the failure criterion

Table 4.2 reports, along with the values of r_c, the size of the second-phase particles and the spacing between them that were identified from the micrographs presented in Chapter 2. It can be seen that the value of r_c correlates relatively well with the average size of the particles. This fact is very obvious for the adhesives 'ESP 110' and 'Betamate 1493', for which r_c lies in the middle of the range of particle sizes, but is somewhat less striking for the adhesive 'Betamate 73455'. However, from Figure 4.5 (reproduced from Figure 2.7(b)), it clearly appears that there are many more silica particles of 10-20 µm in size than bigger particles so it is reasonable to assume that the average size of the particles is about 20 µm and that the value of r_c also correlates well with this average for the adhesive 'Betamate 73455'. To further support this observation, multiple micrographs should be obtained on different specimens and statistical image analyses should be performed but this was beyond the scope of the present study. Nevertheless, from a conceptual point of view, this observation is in full agreement with the physical motivation of the model. Indeed, it clearly makes sense that the (macroscopic) maximum principal stress needs to reach the critical value for void nucleation over a distance at least equal to the size of the particle for the void nucleation to be effective. (As a reminder, it turned out that imposing the maximum principal stress to be equal to σ_c at a critical distance was equivalent to imposing to be larger than or equal to σ_c over that distance.)

As far as the values of the maximum principal stress reported in Table 4.2 are concerned, they are supposed to generate a sufficient maximum principal stress in the particles (or at their interface) for them to fracture, debond or cavitate the second-phase particle. Table 4.2 shows that the maximum principal stress for the adhesive 'Betamate 1493' is larger than for the adhesive 'Betamate 73455' for particles of the same material, namely silica particles, which can be explained by the fact that these particles are smaller in the adhesive 'Betamate 1493' (see Pardoen and Pineau, 2007). Further, Table 4.2 shows that the maximum principal stress for the adhesive 'ESP 110' is itself larger than for the adhesive 'Betamate 1493' for particles of different materials, namely aluminium and rubber particles. This observation could be explained by the fact they these particles have a higher adhesion to the epoxy matrix and/or contain less defects and/or are more ductile, and hence require a larger macroscopic stress to debond or to cavitate.

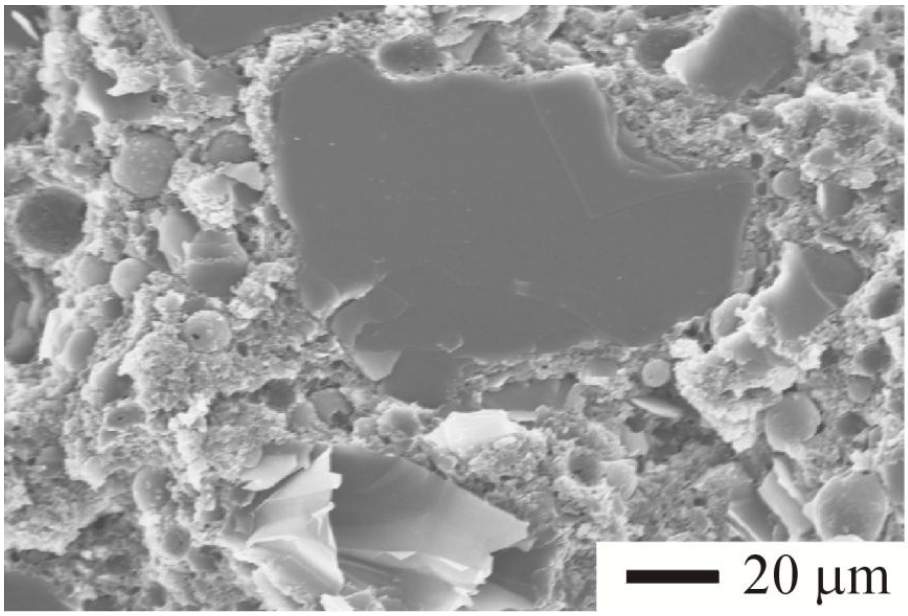

Figure 4.5: Typical fracture surface of the adhesive Betamate

The above interpretations support the idea of the failure criterion being suitable to predict the fracture, debonding or cavitation of a second-phase particle located at crack tip. The physical motivation behind that criterion being also suitable for the prediction of crack propagation is that: (i) statistically, there will always be, along the crack front, at least one second-phase particle very close to the crack tip, and, (ii) the fracture, debonding or cavitation of this second-phase particle will instantly

induce a locally unstable crack growth over a finite distance large enough for the crack tip to reach the next second-phase particle, as observed for example on the fracture surfaces of the adhesive 'Betamate 1493' (see Section 2.3.4).

4.2. Comparison between experimental data and numerical predictions

All the different experimental configurations were simulated in Section 4.1.4 by iteratively modifying the crack length (in the EPFM wedge-peel test simulations) or the wedge thickness (in the equivalent wedge-peel test simulations meant to represent the LEFM TDCB tests) until the predicted values of the residual radius of curvature or the predicted values of the adhesive fracture energy were perfectly matching, for each experimental configuration, with the minimum and maximum values that had been measured experimentally. All these simulations were now re-run in the present Section, but this time by iteratively modifying the crack length (in the wedge-peel test simulations) or the wedge thickness (in the equivalent wedge-peel test simulations representing the TDCB tests) until the failure criterion was satisfied, that is until the predicted value of the maximum principal stress at a distance ahead of the crack tip equal to r_c was equal to σ_c, the values of r_c and σ_c being taken from Table 4.2 at the centre of the uncertainty intervals. The value of the corresponding residual radius, R_a or R_2, of curvature for the wedge-peel test and the adhesive fracture energy, G_a, for both test configurations was then deduced from the simulations. The idea was to evaluate what would be the discrepancy between the numerical predictions and experimental data and, hence, assess the accuracy of the model when used with values of the material parameter which were held constant for a given adhesive, i.e. a single pair of constant values of r_c and σ_c for a given adhesive.

4.2.1. Adhesive 'Betamate 73455'

Figure 4.6(a) shows a comparison between the experimental values of the average radius of curvature that were measured from the wedge-peel test specimens made using the adhesive 'Betamate 73455' and the numerical predictions obtained with the model when forcing the crack to run along the centreline of the specimens (pure mode I conditions). The overall agreement is very good. Taking into account the experimental scatter, all the numerical predictions are within ±10% of the experimental values. Further, the general trend that is observed experimentally as a function of the thickness of the adhesive layer, i.e. a decrease of the radius of curvature, is well reproduced numerically. The only shortcoming of the numerical results is that the radius of curvature is a little underestimated (or, equivalently, the adhesive fracture energy is a little overestimated) for the cases with $h_{adh} = 0.18$ mm and $h_{adh} = 0.24$ mm. These observations could be attributed, as will be shown later for the adhesive 'Betamate 1493', to the fact that the crack was

forced to run exactly along the centreline of the specimens in the simulations, whereas it always ran a little way from the centreline in the experiments.

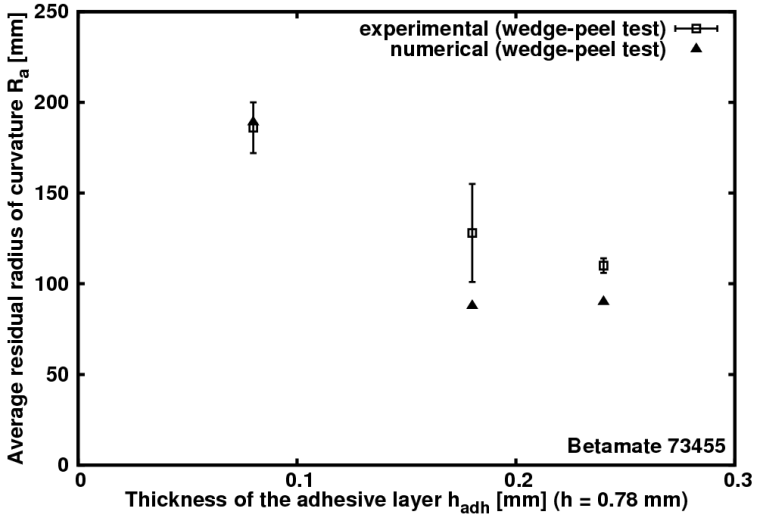

(a)

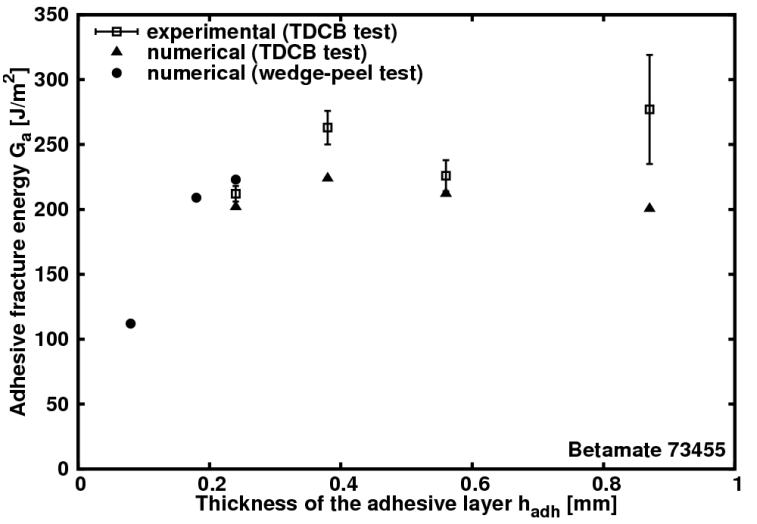

(b)

Figure 4.6: Comparison between the experimental data and the numerical predictions for the adhesive 'Betamate 73455' obtained (a) in the wedge-peel test, and, (b) in the TDCB test

Figure 4.6(b) shows a comparison between the experimental values of the adhesive fracture energy that were measured on the TDCB test specimens made using the adhesive 'Betamate 73455' and the numerical predictions obtained with the model when forcing the crack to run along the centreline of the specimens (pure mode I conditions). The overall agreement is again very good. Taking into account the experimental scatter, all numerical predictions are within ±10% of the experimental values. Further, the general trend that is observed experimentally for the values of G_a as a function of the thickness, h_{adh}, of the adhesive layer is reproduced numerically. The only shortcoming of the numerical results is that, unlike the wedge-peel test results, the model now underestimates the adhesive fracture energy for the thicker values of h_{adh} and even seems to predict a steady decrease of the adhesive fracture energy for $h_{adh} \geq 0.4$ mm which does not seem to be the case in the experiments.

Figure 4.6(b) also shows the numerically predicted values of the adhesive fracture energy that were obtained from the numerical simulations of the EPFM wedge-peel test in Figure 4.6(a). Although there are no experimental data for comparison purposes (the complexity of the wedge-peel test makes it difficult to get an experimental value for G_a through the use of an accurate analytical expression), they can directly be compared to the numerically predicted and measured values of G_a for the LEFM TDCB test. Indeed, the values agree very well with each other where they overlap at an adhesive layer thickness of $h_{adh} = 0.24$ mm, and all the predictions indicate a significant decrease of the adhesive fracture energy with a decreasing adhesive layer thickness. This latter observation further agrees with the experimental data commonly found in the literature (see e.g. Chai, 1986; Kinloch and Shaw, 1981).

It can be concluded from the above results that the proposed model is suitable to predict the steady-state failure of adhesive joints made using the adhesive 'Betamate 73455' with thicknesses of the adhesive layer ranging from 0.1 to 1 mm with constant values of the material parameters r_c and σ_c (see Table 4.2).

4.2.2. Adhesive 'ESP 110'

Figure 4.7(a) shows a comparison between the experimental values of the radius of curvature that were measured on the adherend closest to the crack plane of the EPFM wedge-peel test specimens made using the adhesive 'ESP 110' and the numerical predictions obtained with the model when forcing the crack to run 25 µm below one of the adhesive/adherend interfaces (and evaluating the radius of curvature on the free surface of the closest adherend to that crack plane). This failure path matches that seen in the experimental studies and comes with some contribution of mode II. The overall agreement between the experimental results

and the theoretical predictions is excellent. Indeed, all the numerical predictions based upon the critical stress/distance model lie within the experimental error bars.

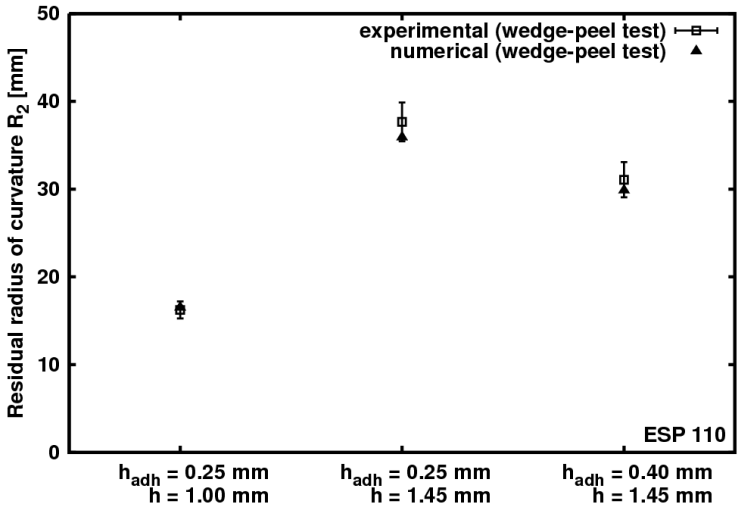

(a)

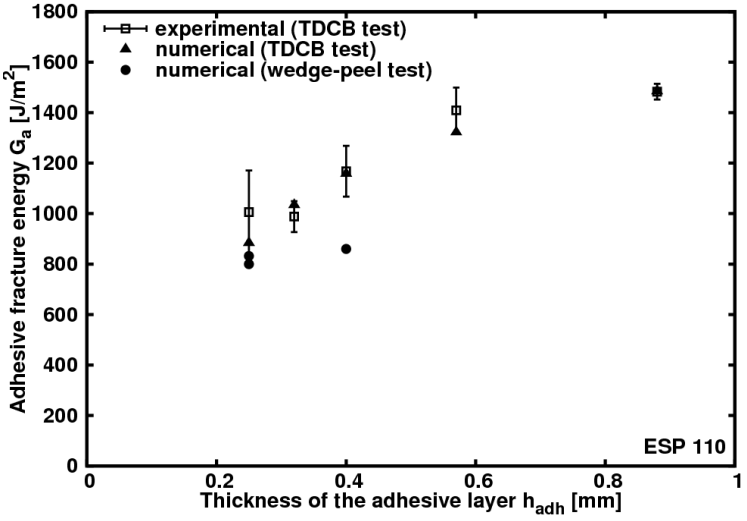

(b)

Figure 4.7: Comparison between the experimental data and the numerical predictions for the adhesive 'ESP 110' obtained (a) in the wedge-peel test, and, (b) in the TDCB test

Figure 4.7(b) shows a comparison between the experimental values of the adhesive fracture energy that were measured on the LEFM TDCB test specimens made using the adhesive 'ESP 110' and the numerical predictions obtained with the model when forcing the crack to run along the centreline of the specimens (pure mode I conditions), this being the failure path observed for these joints. The overall agreement is again excellent: all numerical predictions lie within the experimental error bars.

Figure 4.7(b) also shows the numerically-predicted values of the adhesive fracture energy that were obtained from the simulations of the EPFM wedge-peel test in Figure 4.7(a). For an adhesive layer thickness of $h_{adh} = 0.25$ mm, these values agree well with both the numerical predictions and the experimental data from the LEFM TDCB tests. For an adhesive layer of $h_{adh} = 0.40$ mm, the value of G_a that is obtained from the numerical simulation of the wedge-peel test specimens is significantly lower than the one obtained either experimentally or numerically with the TDCB test specimens. The reason for this is that the crack was running with some contribution of mode II close to one of the adhesive/adherend interfaces in the simulation of the wedge-peel test specimens, unlike that observed for the TDCB test specimens where the crack runs close to the centre of the adhesive layer, i.e. under quasi pure mode I conditions. To support this suggestion it should be noted that Kawashita et al. (2008) have shown experimentally, for this same type of adhesive, that the former locus of joint failure results in a lower value of the adhesive fracture energy due to the geometrical constraint on the plastic zone extension. (Also of relevance is the fact that this effect is more prominent at larger values of h_{adh}, as shown both experimentally and theoretically on the adhesive 'Betamate 73455' in Section 3.4.2.2.)

It can be concluded from the above results that the proposed model is suitable to predict the steady-state failure of adhesive joints made using the adhesive 'ESP 110' with thicknesses of the adhesive layer ranging from 0.1 to 1 mm with constant values of the material parameters r_c and σ_c (see Table 4.2).

4.2.3. Adhesive 'Betamate 1493'

Figure 4.8(a) shows a comparison between the experimental values of the average radius of curvature that were measured on the wedge-peel test specimens made using the adhesive 'Betamate 1493' and the numerical predictions obtained with the model when forcing the crack to run along the centreline of the specimens (pure mode I conditions). For an adhesive layer thickness equal to $h_{adh} = 0.05$ mm, the agreement is excellent. However, for an adhesive layer thickness equal to $h_{adh} = 0.18$ mm, the numerically-predicted value is only about 50% of the corresponding experimental value meaning, as for the adhesive 'Betamate 73455'

(see Section 4.2.1), that the model tends to overestimate the adhesive fracture energy for relatively thick adhesive layers. As already suggested above, a possible explanation for that is that the crack was forced to run along the centreline of the specimens in the simulations whereas it always ran a little way from the centreline in the experiments. To verify this explanation, a simulation was rerun, for an adhesive layer thickness equal to $h_{adh} = 0.18$ mm, by forcing the crack to run closer to one of the adhesive/adherend interfaces, namely at a distance of 15 μm below an adhesive/adherend interface. The resulting value of the average residual radius of curvature is represented in Figure 4.8(a). As can be seen in Figure 4.8(a), the experimental value now lies between the two numerical predictions, which supports the above explanation since the model will obviously be able to reproduce accurately the experimental measurement by forcing the crack to run somewhere between the centreline of the specimen and a distance of 15 μm from one of the adhesive/adherend interfaces. A significant amount of energy is dissipated through plasticity in the adhesive and the fracture energy is thus very sensitive, as will be shown in the sequel, to the amount of material that is made available for plastic dissipation between the crack plane and the adhesive/adherend interfaces and to the distance between the two.

Figure 4.8(b) shows a comparison between the experimental values of the adhesive fracture energy that were measured on the TDCB test specimens made using the adhesive 'Betamate 1493' and the numerical predictions obtained with the model when forcing the crack to run along the centreline of the specimens (pure mode I conditions). The overall agreement is here excellent: all numerical predictions lie within the experimental error bars.

Figure 4.8(b) also shows the numerically predicted values of the adhesive fracture energy that were obtained from the numerical simulations of the wedge-peel test in Figure 4.8(a). Although there are no experimental data that they can directly be compared with, these numerical values do agree with those obtained by modelling the TDCB test specimens, as well as with the experimental results from the TDCB test. For example, the values of G_a from the two very different test configurations agree very well with each other at an adhesive layer thickness of $h_{adh} = 0.20$ mm, where values of G_a from both tests are available, and the results from both test configurations predict a significant decrease of the adhesive fracture energy with an increasing thickness of the adhesive layer thickness, as reported previously and as discussed above.

It can be concluded from the above results that the proposed model is suitable to predict the steady-state failure of adhesive joints made using the adhesive

'Betamate 1493' with thicknesses of the adhesive layer ranging from 0.1 to 1 mm with constant values of the material parameters r_c and σ_c (see Table 4.2).

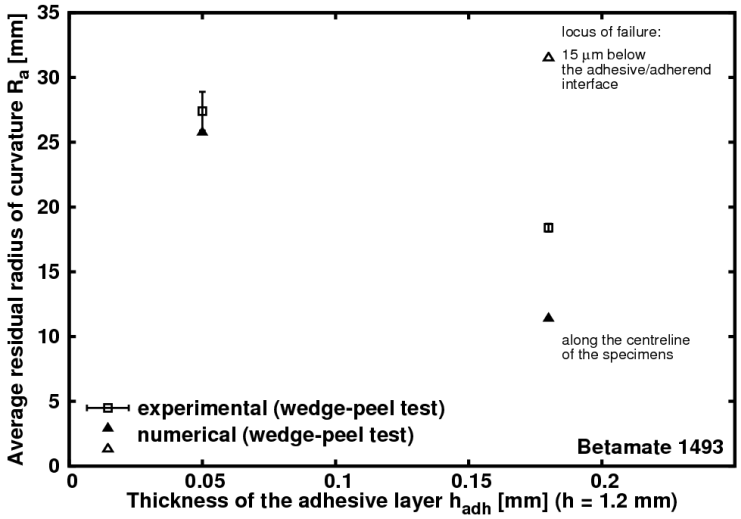

(a)

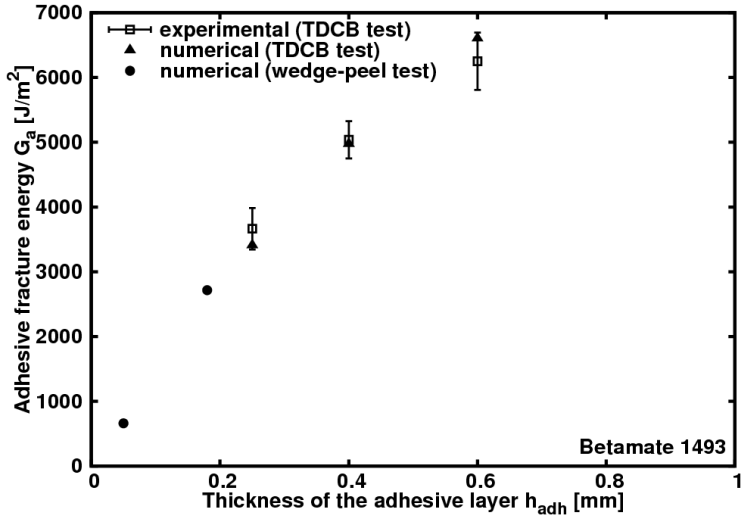

(b)

Figure 4.8: Comparison between the experimental data and the numerical predictions for the adhesive 'Betamate 1493' obtained (a) in the wedge-peel test, and, (b) in the TDCB test

4.3. Parametric study

The purpose of the present Section is to conduct a parametric study on the relationship of the adhesive fracture energy to the adhesive layer thickness that may be predicted by the critical stress/distance model for different material parameters. To limit the scope, this study was concerned with (i) only the LEFM TDCB test, since this is an ISO Standard test method, (ii) only pure mode I loading conditions, (iii) only using Equation (4.8) for describing the hardening law for the adhesive, since this equation only involves one parameter, and (iv) only critical stress/distance material parameters ranging over the values found for the three adhesives considered in the present study, since these adhesives do represent a very wide range of epoxy-based structural adhesives. To extend the applicability of this parametric study, the results were made non-dimensional.

4.3.1. Dimensional analysis

Within the context described above, a total of eleven dimensional parameters define a particular TDCB test configuration that is being modelled. These eleven quantities consist of: (i) three parameters which define the geometry of the test (i.e. the taper parameter, m, the crack length, a, and the thickness of the adhesive layer, h_{adh}), (ii) two parameters which describe the material behaviour of the adherends, which is assumed to be linear elastic (i.e. the Young's modulus, E_s, and the Poisson ratio, ν_s), (iii) four parameters which describe the elastic-plastic behaviour of the adhesive which is modelled according to Equation (4.8), assuming von Mises plasticity and isotropic hardening (i.e. the Young's modulus, E, the Poisson ratio, ν, the initial yield stress, σ_0, and the hardening exponent, n), and, (iv) two parameters which form the failure criterion (i.e. the maximum principal stress, σ_c, and the critical distance, r_c).

In the general case, the adhesive fracture energy is, with the present model, a function of these eleven parameters:

$$G_a = f(m, a, h_{adh}, E_s, \nu_s, E, \nu, \sigma_0, n, \sigma_c, r_c) \tag{4.10}$$

Equation (4.10) can be made non-dimensional by normalising the thickness of the adhesive layer by r_c, the only length scale that is intrinsic to the adhesive, and by normalising the Young's modulus of the adhesive by the Young's modulus of the adherends:

$$\frac{G_a}{G_a^{ref}} = g\left(a \cdot m, \frac{h_{adh}}{r_c}, \nu_s, \frac{E}{E_s}, \nu, \frac{\sigma_0}{E}, n, \frac{\sigma_c}{\sigma_0}, r_c \cdot m\right) \tag{4.11}$$

where G_a^{ref} is a reference adhesive fracture energy which was taken equal to the mode I fracture energy in plane strain, in an infinite linear-elastic solid possessing,

under the assumption of small strains, a maximum principal stress equal to σ_0 at a distance r_c ahead of the crack tip and which, from the near-tip fields calculated by Irwin (1957), is therefore given by:

$$G_a^{ref} = \frac{1-\nu^2}{E} 2\pi r_c \sigma_0^2 \tag{4.12}$$

The values of G_a^{ref} for the three adhesives considered in Section 4.2 were calculated using Equation (4.12) with the value of $\sigma_{0.2}$ (since, as already mentioned, it is more comparable to the value of σ_0 considered here) and are reported, along with the values of $\sigma_c/\sigma_{0.2}$, in Table 4.2 for reference.

In the Sections below the value of G_a/G_a^{ref} as a function of all the dimensionless groups appearing in the right-hand side of Equation (4.11) are studied; with the exception of $(a \cdot m)$ and ν_s since they describe the details of the conditions of the test while the focus of the study is the adhesive, and also with the exception of ν since most epoxy adhesives have very similar values of Poisson ratios.

4.3.2. Effect of the thickness of the adhesive layer

Figure 4.9 shows the evolution of the normalised adhesive fracture energy as a function of the normalised thickness of the adhesive layer for a particular configuration that is representative of the results that can be obtained in the most general case.

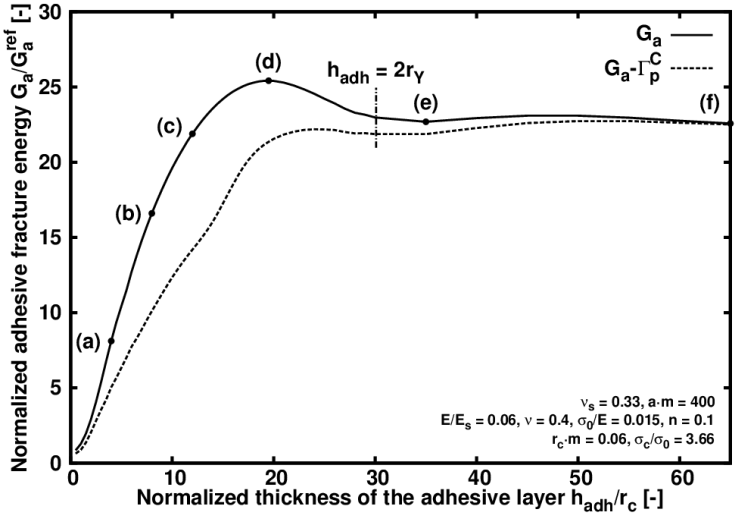

Figure 4.9: The predicted normalized adhesive fracture energy as a function of the normalized thickness of the adhesive layer for a typical case

As the thickness of the adhesive layer increases, the adhesive fracture energy first increases, reaches a maximum and then decreases to a more or less constant plateau, a trend that is commonly observed experimentally (see e.g. Chai, 1986; Kinloch and Shaw, 1981). To gain a better understanding of this curve, and because it is expected that most of the contribution to the value of the adhesive fracture energy comes from the plastic dissipation in the adhesive, Γ_p, the spatial distributions of the plastic dissipation in the adhesive, $\partial^2\Gamma_p/\partial X_1\partial X_2$, for the points labelled from (a) to (f) in Figure 4.9 were ascertained as described in Section 3.4.3.2 and are plotted in Figure 4.10. As can be seen in Figure 4.10(e), three different zones of plastic dissipation, already identified by c, generally develop in the adhesive: zone A, which represents the crack tip plasticity, zone B, which is due to a phenomenon referred to as reverse plastic loading, and zone C, which can be attributed to the shear stresses which act at the adhesive/adherend interface resulting from the restraining effect of the adherend and the consecutive through-the-thickness gradient of the E_{11} strains (see Figure 3.13.). As the thickness of the adhesive layer is increased from (a) to (c), the pattern of plastic dissipation essentially scales, and the adhesive fracture energy increases linearly as can be seen in Figure 4.9. For adhesive layer thicknesses above values of about 10 r_c, i.e. from (d) to (f), the patterns of plastic dissipation in zones A and B tend to stabilise while the plastic dissipation in zone C progressively vanishes so that, as can be seen in Figure 4.9, the adhesive fracture energy reaches a maximum and then decreases to a plateau value once there is no more plastic dissipation in zone C.

A more quantitative description of this evolution can be obtained by evaluating the approximate plastic dissipation in zones A, B and C, respectively denoted by Γ_p^A, Γ_p^B and Γ_p^C, following the methodology suggested in Section 3.4.3.2, and plotting the evolution of these quantities with the adhesive layer thickness, which is shown in Figure 4.11. Indeed, the latter clearly confirms that the plastic dissipation in zones A and B monotonically increases with the adhesive layer thickness. This is because there is more material available for plastic dissipation. The plastic dissipation in zones A and B reaches a plateau value. Whereas the plastic dissipation in zone C after first increases, since there is more material available for plastic dissipation, but then rapidly disappears after reaching a peak value since the crack tip is has moved too far away from the adhesive/adherend interface to build up significant shearing and plastic dissipation there.

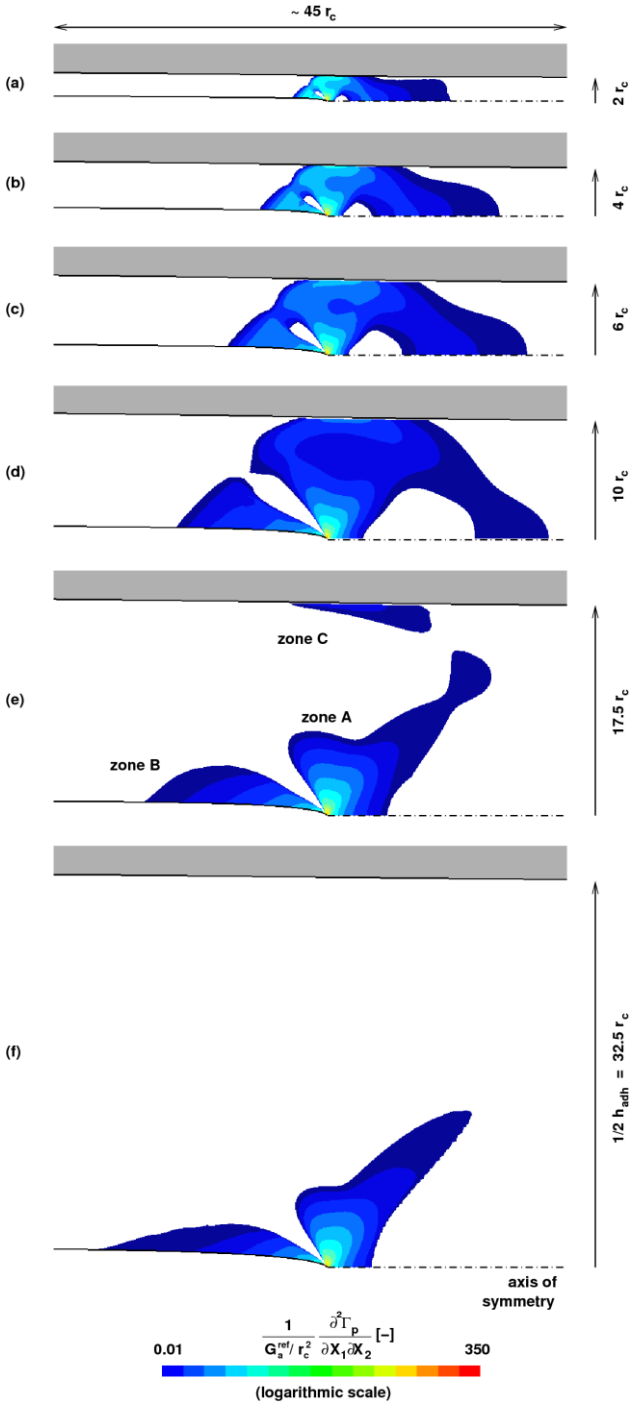

Figure 4.10: The predicted spatial distribution of the normalized plastic-energy dissipation for different adhesive layer thicknesses

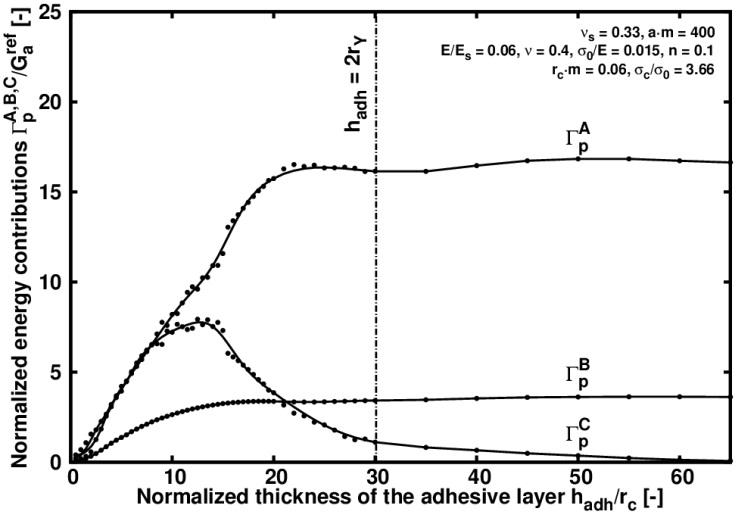

Figure 4.11: The predicted normalized plastic dissipation contributions to the adhesive fracture energy as a function of the normalized thickness of the adhesive layer for a typical case

By subtracting an approximate value of the plastic dissipation in zone C, Γ_p^C (as shown in Figure 4.11), from the adhesive fracture energy (as shown in Figure 4.9), it can quantitatively be verified that zone C is at the origin of the peak observed in the evolution of G_a/G_a^{ref} with h_{adh}/r_c, see Figure 4.9. It can also be seen in Figure 4.11 that the plastic dissipation in zones A and B reach their plateau values when the thickness of the adhesive layer is sufficiently large for the full height of the plastic zone under small-scale yielding conditions to develop on both sides of the crack plane, i.e. when:

$$h_{adh} \sim 2r_Y \tag{4.13}$$

with (Kinloch and Shaw, 1981):

$$r_Y = \frac{1}{3\pi}\frac{EG_a^{SSY}}{(1-\nu^2)\sigma_0^2} \tag{4.14}$$

so that, together with Equation (4.12), Equation (4.13) becomes:

$$\frac{h_{adh}}{r_c} \sim \frac{2r_Y}{r_c} = \frac{4}{3}\frac{G_a^{SSY}}{G_a^{ref}} \tag{4.15}$$

where G_a^{SSY} is the adhesive fracture energy under small-scale yielding conditions that was taken, as an approximation, equal to the plateau value of $G_a(h_{adh}/r_c = 65)$ in Figure 4.9.

4.3.3. Effect of the critical value of the maximum principal stress

Figure 4.12 shows the evolution of the normalised adhesive fracture energy as a function of the normalized thickness of the adhesive layer for different values of σ_c/σ_0 equal to 2.23, 3.43, 3.59 and 3.66. This last value has been chosen for comparative purposes to be the same as that used in Section 4.3.2, whereas the other values of σ_c/σ_0 were chosen to produce the same degree of offset between the successive curves at an adhesive layer thickness $h_{adh}/r_c = 65$. Figure 4.12 also shows the locations on these curves where $h_{adh} = 2r_Y$ and the energy values that are obtained by subtracting the plastic dissipation in zone C from the adhesive fracture energy to verify one more time that zone C is at the origin of the peak in the G_a versus h_{adh} curves.

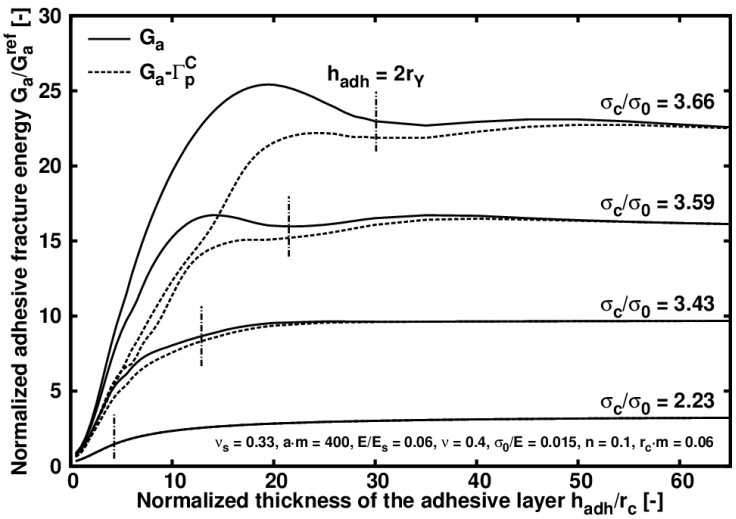

Figure 4.12: The predicted normalized adhesive fracture energy as a function of the normalized thickness of the adhesive layer for different values of the critical stress

As the critical value of the maximum principal stress is increased, the level of the stresses ahead of the crack tip increases and, as a consequence, (i) the adhesive

fracture energy is larger, (ii) the effect of zone C, i.e. the intensity of the peak, increases since the gradient of the strains through the thickness of the adhesive layer responsible for the shearing at the adhesive/adherend interface becomes larger, and, (iii) the peak (if present) and plateau values of the adhesive fracture energy occur at relatively larger thicknesses of the adhesive layer. Consequently, these results clearly demonstrate that not all adhesives will show a peak in the adhesive fracture energy as a function of the thickness of the adhesive layer; more particularly, those showing only limited plastic dissipation will not exhibit a peak. The value of the thickness of the adhesive layer at which the adhesive fracture energy reaches a plateau also correlates relatively well with the predictions from Equation (4.15), although this equation seems to give values that somewhat underestimate the position of the peak as the value of σ_c/σ_0 is decreased.

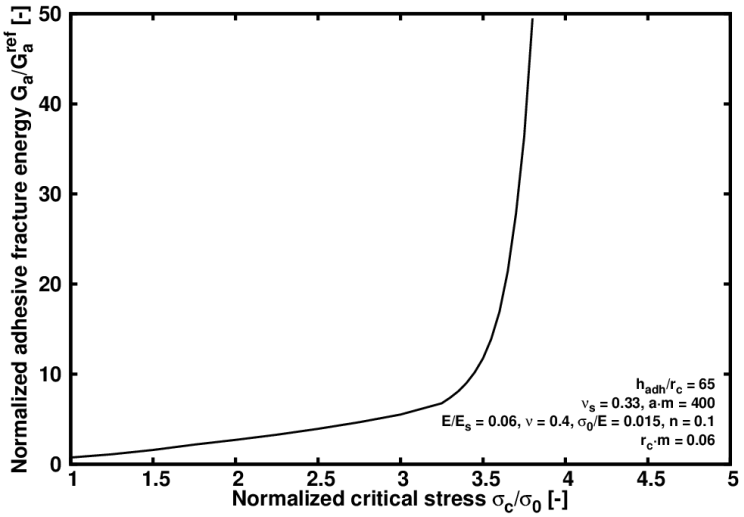

Figure 4.13: The predicted normalized adhesive fracture energy as a function of the critical stress for large adhesive layer thicknesses

Figure 4.13 shows the evolution of the plateau value of the adhesive fracture energy at relatively large thicknesses of the adhesive layer ($h_{adh}/r_c = 65$) as a function of the critical maximum principal stress. It can be seen that the adhesive fracture energy increases monotonically with the maximum principal stress, first linearly, when only limited plastic dissipation develops, and then exponentially starting from $\sigma_c/\sigma_0 \sim 3.25$. This result agrees very well with those obtained by Tvergaard and Hutchinson (1992) under steady-state conditions in infinite elastic-plastic solids. Although, they employed a different type of model, in which a

cohesive zone model served as failure criterion, the value of σ_c corresponding in that case to the peak stress in the cohesive zone law. This an important result which shows the continuity of the present model with the AACZ model discussed in Chapter 3.

4.3.4. Effect of the critical distance

The different simulations that were run to produce the curves in Figure 4.12 were re-run by successively using a value of $r_c \cdot m = 0.03$ and 0.09, instead of 0.06, to match the range of values spanned by the three adhesives considered in Section 4.2. The resulting values of the normalized adhesive fracture energy as a function of the normalized thickness of the adhesive did not show any significant effect of the value of $r_c \cdot m$. This means that the value of the adhesive fracture energy scales relatively well with the value of r_c and that the geometrical details of the TDCB test specimens (i.e. the reference crack length, a, in the equivalent wedge-peel test model and the taper parameter m) are not of significance (as long as the value of r_c remains small compared to the dimensions of the adherends).

4.3.5. Effect of the hardening exponent

Figure 4.14 shows the evolution of the normalised adhesive fracture energy as a function of the normalized thickness of the adhesive layer for different values of the hardening exponent equal to 0.05, 0.1 (as in Figure 4.12) and 0.2. Also, Figure 4.14 shows the effect of different values of the maximum principal stress which, for comparative purposes, gives the same adhesive fracture energy values at an adhesive layer thickness of $h_{adh}/r_c = 65$, i.e. as in Figure 4.12.

Figure 4.14 first shows that, as expected, as the hardening exponent is increased, a higher maximum principal stress value is required to produce the same extent of plastic dissipation and, hence, the same value of the adhesive fracture energy at an adhesive layer thickness of $h_{adh}/r_c = 65$. Figure 4.15 shows in more detail the change of the adhesive fracture energy, at an adhesive layer thickness of $h_{adh}/r_c = 65$, as a function of the maximum principal stress for different values of the hardening exponent. It can be seen that below $\sigma_c/\sigma_0 \sim 3$, where the adhesive fracture energy increases linearly, the effect of the hardening exponent is negligible, since there is only limited plastic dissipation. For values of σ_c/σ_0 above 3, the adhesive fracture energy starts increasing exponentially at a larger value of the maximum principal stress, and more smoothly, as the hardening exponent is increased, since the adhesive is now capable of accommodating larger stresses with smaller strains and less plastic dissipation. This result is again in very good agreement with those obtained by Tvergaard and Hutchinson (1992).

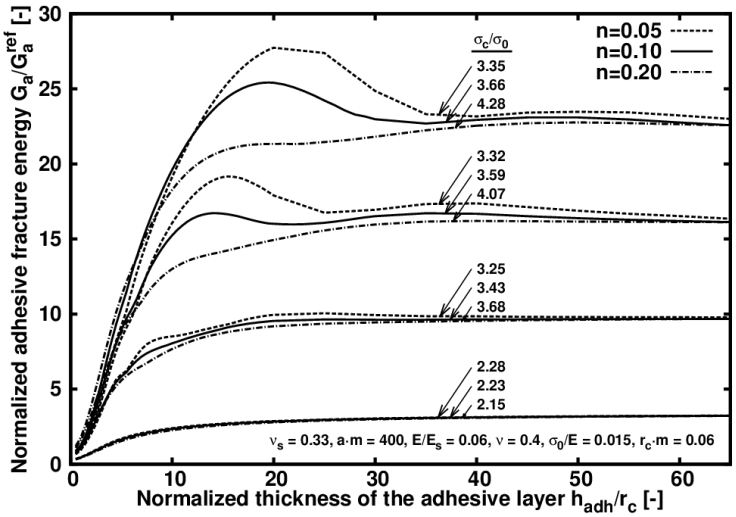

Figure 4.14: The predicted normalized adhesive fracture energy as a function of the normalized thickness of the adhesive layer for different values of the critical stress and of the hardening exponent

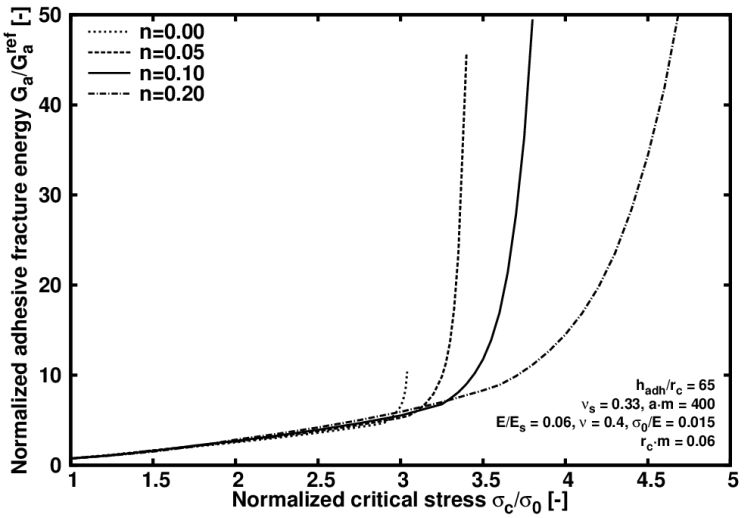

Figure 4.15: The predicted normalized adhesive fracture energy as a function of the critical stress for large adhesive layer thicknesses and for different values of the hardening exponent

Returning to Figure 4.14, it can further be seen that, as the hardening exponent is decreased for a given level of the adhesive fracture energy, the effect of zone C, i.e. the cause of the presence and intensity of the peak, increases because the strains at the crack tip need to be higher to produce the same level of adhesive fracture energy, while the restraining effect of the high-modulus adherends at the adhesive/adherend interface remains the same. This means that the through-the-thickness gradient of strains and, hence, the shear stresses and strains at the adhesive/adherend are higher. Figure 4.14 also shows that the effect of the hardening exponent is more prominent for relatively large adhesive fracture energy values, since the higher the value of the adhesive fracture energy, the larger the plastic dissipation and, hence, the larger the differences between the different hardening exponents.

4.3.6. Effect of the Young's modulus of the adhesive

Figure 4.16 shows the evolution of the normalised adhesive fracture energy as a function of the normalised thickness of the adhesive layer for different values of the normalised Young's modulus of the adhesive E/E_S equal to 0.04, 0.06 (as in Figure 4.12) and 0.08, and, for each of these, for four different values of the normalised maximum principal stress, which are the same as those used in Figure 4.12.

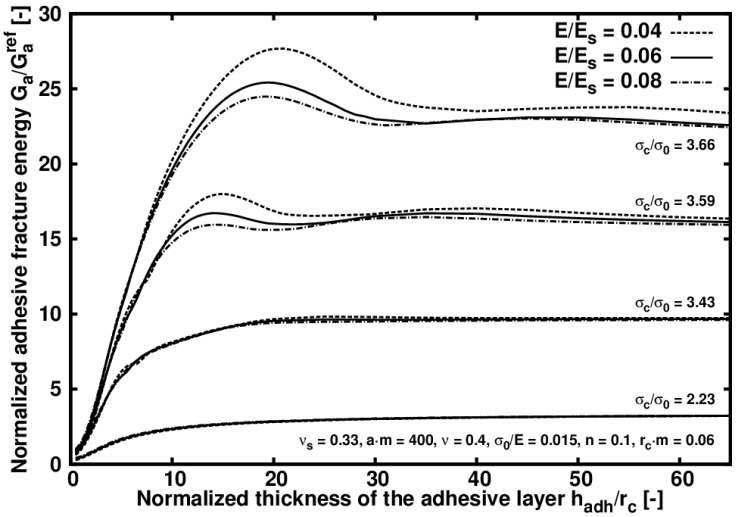

Figure 4.16: The predicted normalized adhesive fracture energy as a function of the normalized thickness of the adhesive layer for different values of the critical stress and of the Young modulus of the adhesive

It may be observed that the normalised adhesive fracture energy is relatively independent of the value of E/E_s at large thicknesses of the adhesive layer ($h_{adh}/r_c = 65$). This means that the adhesive fracture energy that is measured experimentally for relatively thick adhesive layers is largely independent of the Young's modulus of the adherends, which supports the idea that the TDCB test gives a value for the adhesive fracture energy that is intrinsic to the adhesive material when failure through the adhesive layer is observed.

Further, it may be seen in Figure 4.16 that, as the Young's modulus of the adhesive is decreased for a given value of the maximum principal stress, the effect of plastic dissipation in zone C increases, since the restraining effect of the high-modulus adherends at the adhesive/adherend interface becomes more important, compared to the modulus of the adhesive. This means that the through-the-thickness gradient of the E_{11} strains and the shear stresses and strain at the adhesive/adherend are larger. Figure 4.16 also shows that this effect is more important for relatively high values of the adhesive fracture energy; since the higher the adhesive fracture energy, the larger the effect of zone C, regardless of the value of E/E_s.

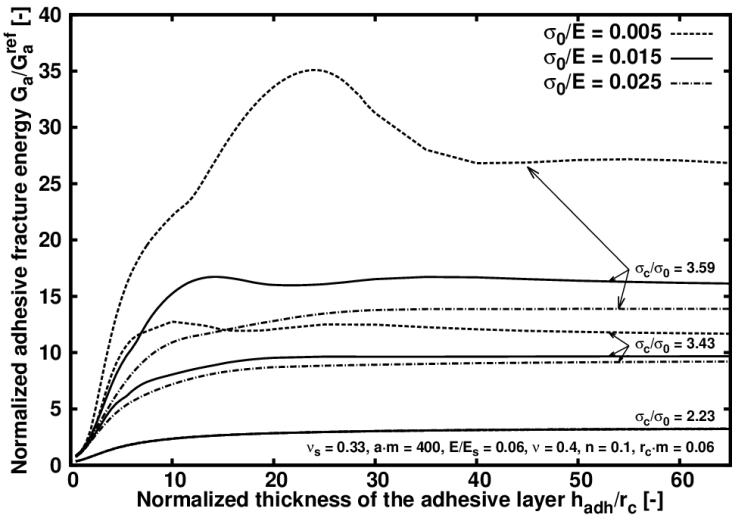

Figure 4.17: The predicted normalized adhesive fracture energy as a function of the normalized thickness of the adhesive layer for different values of the critical stress and of the initial yield stress of the adhesive

4.3.7. Effect of the initial yield stress of the adhesive

Figure 4.17 shows the change of the normalised adhesive fracture energy as a function of the normalised thickness of the adhesive layer for different values of the normalised initial yield stress of the adhesive σ_0/E for values equal to 0.005, 0.015 (as in Figure 4.12) and 0.025. Also, shown are the effects of three different values of the normalised maximum principal stress identical to those used in Figure 4.12, with the exception of the largest value of 3.66 which gave, together with a value of σ_0/E equal to 0.005, far higher values of the adhesive fracture energy that would have been difficult to represent clearly on the same plot.

It may be seen that, as the initial yield stress of the adhesive is decreased, (i) the overall level of the adhesive fracture energy increases because the yield strain is smaller and, hence, plastic dissipation is more easily generated, and, (ii) the effect of zone C is more prominent because the same shear strains at the adhesive/adherend interface induce more plastic dissipation. Figure 4.17 also shows that this effect is more important for relatively large values of the critical maximum principal stress for which the associated strains are larger. These results, as far as the curves for $\sigma_c/\sigma_0 > 2.23$ are concerned, are not in agreement with the results of Tvergaard and Hutchinson (1992) which showed that the ratio σ_0/E had a negligible effect. The reason for is that Tvergaard and Hutchinson (1992) studied infinite elastic-plastic solids for which the conditions of small-scale yielding conditions applied, which is not case in the present study. This may be expressed by considering when the height of the plastic zone is not small compared to the thickness of the adhesive layer, for example:

$$2r_Y > \frac{1}{10} h_{adh} \tag{4.16}$$

or, in non-dimensional form, using the right-hand side of Equation (4.15) when:

$$\frac{4}{3}\frac{G_a^{SSY}}{G_a^{ref}} > \frac{1}{10}\frac{h_{adh}}{r_c} \tag{4.17}$$

Noting in Figure 4.17 that the normalised adhesive layer thicknesses being considered range up to $h_{adh}/r_c = 65$, Equation (4.16) now becomes:

$$\frac{G_a^{SSY}}{G_a^{ref}} > \sim 5 \tag{4.18}$$

which is indeed the case for the curves with $\sigma_c/\sigma_0 > 2.23$.

4.4. Conclusions

A comparison between the numerical predictions of the MPS model and the experimental data showed that this model gave accurate results, using constant values of the material parameters which form the failure criterion (namely the maximum principal stress and the critical distance) for a given adhesive over a very wide range of thicknesses of the adhesive layer of 0.1-1.0 mm. This was found to be the case for all the adhesives studied, which showed very different values of their adhesive fracture energy, spanning the range of 200-6500 J/m², and for the very different test configurations employed, namely the LEFM TDCB test and the EPFM wedge-peel test. This model hence shows a great potential in engineering applications.

The results of the parametric study showed many similarities with the predictions that were obtained earlier, with the AACZ model of Chapter 3, by Tvergaard and Hutchinson (1992). Nevertheless, the AACZ approach, as shown in Chapter 3, fails to predict the change of the fracture energy with the thickness of the adhesive layer. The origin of the problem was tentatively proposed to result from the constant value of the energy spent in the cohesive zones independently of the degree of constraint at the crack tip. It was proposed that a damage based approach was the only viable way to circumvent this issue. The present Chapter shows that indeed the use of an extremely simple damage model allows the predictions of the present model to encompass a far larger range of thicknesses of the adhesive layer. In the present model, a change of constraint leads to an earlier attainment of the critical stress with smaller plastic strains in the near crack-tip region. It is exactly as if the local energy spent in an analogous CZM would be smaller. For the future, more elaborate damage models could obviously be used, at the expenses of more material parameters. The present study proves that the nucleation of damage might be, for many adhesive systems, the key element to model.

Chapter 5
Conclusions and perspectives

5.1. Main results

The present thesis has focused on the development of numerical models capable of predicting, with constant material parameters, the predominantly mode I fracture of adhesive joints made from epoxy-based structural adhesives and metallic adherends showing a negligible or only limited amount of mode II. The joints were tested according to three different test configurations with the test specimens showing different adhesive layer thicknesses, different adherend thicknesses and different adherend materials. The three types of test configuration were: the linear elastic fracture-mechanics (LEFM) tapered double-cantilever beam (TDCB) test, the elastic-plastic fracture-mechanics (EPFM) wedge-peel test and the EPFM fixed-arm peel test. They were tested under quasi-static conditions.

Two models were considered, both relying on finite-element analyses and representing the adherends as well as the adhesive with continuum elements. The first one, referred to as the AACZ model (Adherend + Adhesive + Cohesive Zone), consists of embedding in the adhesive a single row of a cohesive zone elements with zero thickness which are meant to represent and condense the damage mechanisms responsible for fracture. The second one, referred to as the MPS model (Maximum Principal Stress), considers that the conditions for steady-state crack propagation are met when the maximum principal stress reaches a particular value at a critical distance ahead of the crack tip, this particular value being needed to debond, cleave or cavitate the second-phase particles present in the adhesive.

Results showed that the AACZ model, when used with constant parameters, was successful at reproducing accurately:

- The external constraint effects, that is, the effect of a change in the type of test, the adherend material or the adherend thickness;

- The effect of the thickness of the adhesive layer over a range of thicknesses which, for some adhesives, could be relatively limited (of the order of 0.2 mm in range).

Results further showed that, in order to get accurate predictions, it was crucial to allow for the cohesive zone elements to unload elastically.

A general, working criterion making it possible to determine *a priori*, for a given adhesive and given material parameter values, the range of adhesive layer thicknesses for which the AACZ model is valid was not formulated as priority was given to developing and modelling the MPS model, for the reasons discussed below. Indeed, it was demonstrated there is a limit to the increase in adhesive fracture energy that the AACZ model is capable of predicting, with constant parameters, as the thickness of the adhesive layer is steadily increased to relatively large values. As a consequence, it is believed that the AACZ model is not applicable to rubber-toughened, epoxy-based adhesives which show significant increases of the adhesive fracture energy with the thickness of the adhesive layer.

Results showed that the MPS model, when used with constant parameters, has great potential in engineering applications since it was successful at reproducing accurately:

- The external constraint effects, that is, the effect of a change in the type of test, the adherend material or the adherend thickness;
- The effect of the thickness of the adhesive layer over a very large range of thicknesses (0.1-1 mm) regardless of the adhesive and the magnitude of the adhesive fracture energy (e.g. between 150 and 6500 J/m²) that was considered.

The models were also employed in the thesis, within their domain of validity, to conduct parametric studies and gain a better understanding of (i) the different energy contributions to the adhesive fracture energy and (ii) the effects of external and internal constraints, imposed by the adherends and the finite thickness of the adhesive layer. Both models reproduced an experimental trend commonly reported previously in the literature: namely that the adhesive fracture energy first increases linearly, then passes through a peak and then decreases down to a plateau value as the adhesive layer thickness is increased. The physical explanation for this trend was found by identifying and quantifying the different energy contributions to the adhesive fracture energy. These contributions are dominated by the plastic dissipation in three different zones: zone A, attributed to crack tip plasticity, zone B, attributed to a phenomenon called reverse plastic loading, and, zone C, attributed to the shear stresses and strains that develop at the

adhesive/adherend interface. These interfacial shear stresses and strains result from the gradient of the strains in the direction parallel to the crack plane, E_{11}, that develop between the crack tip, where these strains are maximum, and the adhesive/adherend interface, where they are restrained by the stiffer adherend. As the thickness of the adhesive layer is increased, the plastic dissipation in the three zones first increases, as there is more material available which explains why the adhesive fracture energy increases. As the thickness of the adhesive layer is increased further, the plastic dissipation in zones A and B stabilises, since the adhesive layer becomes sufficiently thick for the crack tip plasticity to develop fully. On the other hand, the plastic dissipation in zone C now progressively vanishes, since the distance between the crack tip and the adhesive/adherend interface becomes too large to build-up a significant gradient of E_{11} strains. It is noteworthy that it is the presence of zone C, and the way it changes with changes in the thickness of the adhesive layer, that explains why the adhesive fracture energy passes through a peak and decreases down to a plateau value.

The results of the parametric studies conducted with the MPS model showed that the magnitude of the adhesive fracture energy was largely dependent upon: (i) the value of the critical maximum principal stress (i.e. the value of G_a increasing very rapidly with σ_c), and (ii) the hardening properties of the adhesive (i.e. the value of G_a being magnified by a relatively low hardening-exponent and low initial yield stress values, both of which promote plastic dissipation in the adhesive layer). Both models also showed that the magnitude of the adhesive fracture energy could be largely affected by the locus of failure, especially at larger adhesive layer thickness, in agreement with the experiments. Namely, cracks running close to one of the adhesive/adherend interfaces result in lower values of the adhesive fracture energy. Finally, both models showed that the extrinsic constraint effects were generally quite limited and, more precisely, that the resulting differences they could induce in the values of the adhesive fracture energy at a given thickness of the adhesive layer were within the precision of the experimentally-measured values of G_a. The latter result strongly supports the hypothesis of the adhesive fracture energy, G_a, being a 'characteristic material property' of the adhesive joint, for a given thickness of the adhesive layer h_{adh}, which is independent of the test specimen and other aspects of the test configuration. (It should be mentioned, for the sake of completeness, that any given test configuration did fit in that picture. Indeed, the adhesive fracture energy values were predicted to increase significantly, at large values of the adhesive layer thickness, when using thin arms in the wedge-peel test with the position of the crack being along the centreline of the specimens. However, it is believed that this effect, attributed to significant bending stresses in the adhesive, is prevented to occur in reality as such joints

rather fail with the crack running close to one of the adhesive/adherend interfaces since it is more energy-favourable.)

5.2. Conclusions

Several conclusions can be drawn from the work that has been carried out in the thesis and, more particularly, from the above results.

Firstly, the failure mechanisms in common structural epoxy-based adhesives are highly-dependent upon the triaxial stress-state or the level of constraint, especially for the rubber-toughened systems which show large toughness values, typically above 1000 J/m².

To be of any serious interest in engineering applications, numerical models need to give accurate predictions with a minimum number of material parameters and, hence, reduced material characterization costs. A direct consequence of the first conclusion above and our second conclusion is thus than any suitable numerical model for engineering applications needs to take into account the dependence of the failure upon the level of constraint either inherently, as in the present MPS model, or through a separate equation governing the evolution of the parameters of the failure criterion as a function, for example, of the stress triaxility, as suggested by Hadavinia et al. (2006).

Thirdly, the failure of common structural epoxy-based adhesives (which generally contain second-phase particles) appears to be dominated by the nucleation of voids at the second-phase particles, regardless of the nature of these particles and of the details of the nucleation mechanism (cleavage, debonding or cavitation). This statement needs however to be supported further by more experimental evidence.

Fourthly, the mechanisms of void nucleation in such adhesives are essentially stress-driven processes. More particularly, they appear to be reasonably well captured, from the numerical point-of-view, by the attainment of a critical, macroscopic, maximum principal stress at or over a distance of the order of the average size of the particles. This statement needs however to be supported further by mirco-mechanical calculations.

Fifthly, the toughness of such adhesives essentially comes from the plastic energy that is dissipated in the bulk of the adhesive when attaining the conditions for void nucleation very locally at the crack tip. The toughness values are thus largely dependent upon the hardening capabilities of the adhesive and, for very tough adhesives which can exhibit large strains before failure, upon their rehardening capabilities. Nevertheless, the order of magnitude of the plastic dissipation is

already quite accurately captured with a simple isotropic von Mises plasticity model, providing the latter is fitted over a sufficiently large strain range with respect to the magnitude of the adhesive fracture energy against tensile stress-strain curves obtained on bulk specimens.

Finally, the forces and specimen deformations that are measured on bonded specimens in elastic-plastic fracture mechanics tests such as the wedge-peel test or the fixed-arm peel test significantly depend not only upon the adhesive fracture energy but also on the hardening properties of the adherend material as already suggested by Blackman et al. (2003c). Nevertheless, the latter can be modelled with sufficient accuracy with a simple isotropic von Mises plasticity model, providing it is fitted over the strain-range that is actually undergone by the adherends in the tests.

5.3. Perspectives

Recalling that the motivation behind this thesis is the development of a suitable analysis tool for the design of bonded joints, the MPS model clearly emerges as the better model and a very serious candidate for further work. However, there are a few aspects of the MPS model that need to be considered before final victory can be claimed. Below is a list of suggested steps that need to be considered, in sequential order, to achieve the ultimate goal of a fully-validated and accurate model to act as a design tool for all types of adhesive joints:

- The effect of the position of the crack within the adhesive layer on the predicted value of the adhesive fracture energy should be studied to see, by comparison with experimental data, whether the model is capable of predicting the locus failure associated with the minimum value of the adhesive fracture energy;

  If it is not the case, the model should either be supplemented with a criterion allowing for the accurate prediction of the locus of failure, or be used as it is currently formulated and all possible positions of the crack modelled to give a conservative approach.

- The model should be extended and validated against mixed-mode loading conditions showing larger mode II contributions than envisaged so far and against pure mode II conditions;

  As the failure criterion that is built into the model does not make any assumption about the remote loading, the present model should hopefully be readily applicable, as it is, to these very loading conditions. Another argument supporting this idea is that adhesive joints remotely loaded in

shear often fail locally in mode I anyway. However, if the local mechanisms responsible for fracture under loading conditions with significant mode II contributions turn out to be completely different from the ones identified in the present study, i.e. void nucleation at the second-phase particles, the model will unavoidably have to be supplemented with an additional, suitable criterion.

- The model should be able to take into consideration the effects of test temperature, test rate and test environment;

  A simple approach to this problem consists in modifying the material parameters according to a sub-model for the test temperature and rate (e.g. an Arrhenius equation) and some damage variable tracking the extent of ageing and, for example, degrading the material parameters used in the model. Another suitable option would be to adopt a micro-mechanical approach and to look at the stress partitioning between the epoxy and the second-phase particles, either analytically or through finite element calculations on representative volume elements, as their individual properties are modified by the test temperature, test rate and test environment.

- The model should be extended to polymer-matrix composites.

  This requires the capability to deal with their most often orthotropic behaviour, to predict the complex failure modes they can exhibit and to come with a suitable way of deciding between failure in the adhesive and failure in the adherends.

- Testing procedures and guidelines should be established to inform a potential designer which tests to undertake to obtain the material properties that are needed in the model;

  This includes the determination of the stress-strain curve of the adhesive (which are already well documented in the literature (see e.g. Charalambides and Olusanya, 1997) and the determination of the appropriate yield stress to be used in the model (which was shown in the present thesis to be critical for some adhesives). Further, a limited number of LEFM or EPFM tests should be run with the model to determine which combination of such tests gives very accurate material parameters and to provide the designer with sets of curves, in the spirit of the proposal of Ferracin et al. (2003), to enable them to read directly the parameters of the failure criterion from the results of these tests.

- As the computational times required by the model for the very simple geometries studied in the present thesis are already quite large, a proper methodology should be developed to make it possible to benefit from the model in the case of larger structures;

  The option that would be recommended, since it is computationally efficient, widely available in commercial finite element codes and already quite popular in the adhesive bonding community, would be to use cohesive zone elements to represent the full thickness of the adhesive layer. The cohesive zone law should be determined through homogenisation (see e.g. Salomonsson and Andersson, 2008) from detailed simulations performed with the present MPS model. (Care should be taken in ensuring that the cohesive zone elements are capable of reproducing the coupling between shear and normal deformations, as suggested by Sun et al. (2009).)

- The model should be extended and validated first against simple 3D cases and then against increasingly complex industrial test cases.

Finally, if all of the above steps are successfully completed, the resulting model should serve as the basis to the development of models applicable to fatigue, creep and impact conditions.

References

Adams, R.D., Comyn, J., Wake, W.C., 1997. Structural adhesive joints in Engineering (2nd edition). Chapman & Hall, London.

Andersson, T., Stigh, U., 2004. The stress–elongation relation for an adhesive layer loaded in peel using equilibrium of energetic forces. Int. J. Adhes. Adhes. 41, 413-434.

ASTM D 903. Standard test method for peel or stripping strength of adhesive bonds. ASTM International.

ASTM D 1876. Standard test method for peel resistance of adhesives (T-peel test). ASTM International.

ASTM D 3167. Standard test method for floating roller peel resistance of adhesives. ASTM International.

Bascom, W.D., Cottington, R.L., Jones, R.L., Peyser, P., 1975. The fracture of epoxy-and elastomer-modified epoxy polymers in bulk and as adhesives. J. Appl. Polym. Sci. 19, 2545-2562.

Bertholet, Y., 2006. Wafer Bonding for MEMS technology - Measurement, optimization and multiscale modelling of silicon wafer bonding interface fracture resistance. Ph.D. Thesis. Université catholique de Louvain.

Blackman, B.R.K., Hadavinia, H., Kinloch, A.J., Paraschi, M., Williams, J.G., 2003a. The calculation of adhesive fracture energies in mode I: revisiting the tapered double cantilever beam (TDCB) test. Eng. Fract. Mech. 70, 233-248.

Blackman, B.R.K., Hadavinia, H., Kinloch, A.J., Williams, J.G., 2003b. The use of a cohesive zone model to study the fracture of fibre composites and adhesively-bonded joints. Int. J. Fracture 119, 25-46.

Blackman, B.R.K., Kinloch, A.J., Paraschi, M., Teo, W.S., 2003c. Measuring the mode I adhesive fracture energy, G_{IC}, of structural adhesive joints: the results of an international round-robin. Int. J. Adhes. Adhes. 23, 293-305.

Broxterman, W.E., 2001. Structural adhesives: Trends and driving forces. Adhesive and Sealant Council's Convention & Exposition, New Orleans, LA (USA), Fall 2001.

CETIM, 2006. Guide du collage. Centre technique des industries mécaniques.

Chai, H., 1986. Bond thickness effect in adhesive joints and its significance for mode I interlaminar fracture of composites. In: Composite Materials Testing and Design, ASTM-STP 893, pp. 209-231.

Chai, H., 1988. Fracture work of thin bondline adhesive joints. J. Mater. Sci. Lett. 7, 399-401.

Chai, H., Chiang, M.Y.M., 1998. Finite element analysis of interfacial crack propagation based on local shear, Part II – Fracture. Int. J. Solids Struct. 35, 815-829.

Charalambides, M.N., Olusanya, A., 1997. Report 3: The Constitutive Models Suitable for Adhesives in some Finite Element Codes and Suggested Methods of Generating the Appropriate Materials Data. National Physical Laboratory Project PAJ 1: Failure Criteria and their Application to Visco-Elastic/Visco-Plastic Materials.

Ciba Geigy, 1995. User's guide to adhesives. Technical brochure.

Clarke, J.D., McGregor, I.J., 1993. Ultimate tensile stress over a zone: a new failure criterion for adhesive joints. J. Adhes. 42, 227-245.

Cooper, V., Ivankovic, A., Karac, A., Murphy, N., 2009. The effect of constraint on the fracture toughness of adhesively bonded joints. Proceedings of the 32nd annual meeting of the Adhesion Society, Savannah (USA), 33-35.

Cooper, V., Ivankovic, A., Karac, A., McAuliffe, D., Murphy, N., 2012. Effects of bond gap thickness on the fracture of nano-toughened epoxy adhesive joints. Submitted. Under revision.

Crocombe, A.D., 1989. Global yielding as a failure criterion for bonded joints. Int. J. Adhes. Adhes. 9, 145-143.

Crocombe, A.D., Kinloch, A.J., 1994. Review of adhesive bond failure criteria. MTS Adhesives project 2: Failure Modes and Criteria, AEA-ESD-0107, AEA Harwell

Crocombe, A.D., Richardson, G., Smith, P.A., 1995. A Unified Approach for Predicting the Strength of Cracked and Non-Cracked Adhesive Joints. J. Adhes. 49, 211-244.

Cui, J., Wang, R., Sinclair, A.N., Spelt, J.K., 2003. A calibrated finite element model of adhesive peeling. Int. J. Adhes. Adhes. 23, 199-206.

Da Silva, L.F.M., Adams, R.D., 2002. The strength of adhesively bonded T-joints. Int. J. Adhes. Adhes. 22, 311-315.

Davidson, B.D., 1998. A Predictive Methodology for Delamination Growth in Laminated Composites. Office of Aviation Research Report DOT/FAA/AR-97/87.

Davis, M.J., 1994. The development of an engineering standard for composite repairs. AGARD SMP Specialits Meeting, Sevilla (Spain), 3-5 October 1994.

Dean, R.H., Hutchinson, J.W., 1980. Quasi-static steady crack growth in small-scale yielding. In: Fracture Mechanics, ASTM-STP 700, pp. 383–405.

Dean, G.D., Duncan, B.C., 1998. Preparation and testing of bulk specimens of adhesives. NPL Measurement Good Practice Guide No 17.

Dean, G., Crocker, L., 2001. The Use of Finite Element Methods for Design with Adhesives. Measurement Good Practice Guide No 48. National Physical Laboratory.

Dewolfe, A., Gedney, R., 2010. Adhesives Gain Strength. www.ndtmag.com

Drucker, D.C., Prager, W., 1952. Soil mechanics and plastic analysis for limit design. Quart. J. Appl. Math. 10, 157-165.

Drugan, W.J., Rice, J.R., Sham, T.L., 1982. Asymptotic analysis of growing plane strain tensile cracks in elastic-ideally plastic solids. J. Mech. Phys. Solids 30, 447-473.

Duncan, B.C., 1999. Final report. National Physical Laboratory Project PAJ 1: Failure Criteria and their Application to Visco-Elastic/Visco-Plastic Materials.

FAA AC 20-107B, 2009. US Department of Transportation. Federal Aviation Administration. Advisory Circular No 20-107B.

Fawcett, A., 2004. Cobonding Primary Structure – Processing Issues and Related Tests. FAA Bonded Structures Workshop, Seattle (USA), June 16-18, 2004.

Fernlund, G., Spelt, J.K., 1991. Failure load prediction II – experimental results. Int. J. Adhes. Adhes. 11, 221-227.

Ferracin, T., Landis, C.M., Delannay, F., Pardoen, T., 2003. On the determination of the cohesive zone properties of an adhesive layer from the analysis of the wedge-peel test. Int. J. Solids Struct. 40, 2889-2904.

Ferracin, T., 2003. Mechanics of failure in adhesively bonded steel assemblies. Université catholique de Louvain, Belgium. PhD Thesis.

Georgiou, I., Hadavina, H., Ivankovic, A., Kinloch, A.J., Tropsa, V., Williams, J.G., 2003. Cohesive zone models and the plastically deforming peel test. J. Adhesion 79, 239-265.

Georgiou, I., 2003. The fracture of adhesively-bonded aluminium joints for automotive structures. Imperial College London, United Kingdom. PhD Thesis.

Goland, M., Reissner, E., 1944. The stresses in cemented joints. J. Appl. Mech., Trans. ASME 11, 17-17.

Grant, L.D.R., Adams, R.D., da Silva, L.F.M., 2009. Experimental and numerical analysis of single-lap joints for the automotive industry. Int. J. Adhes. Adhes. 29, 405-413.

Guiu, A., Shanahan, M.E., 2002. Adhesion between semi-crystalline polymers: grafted PE/EVOH copolymer. Int. J. Adhes. Adhes. 22, 415-420.

Hadavinia, H., Kawashita, L., Kinloch, A.J., Moore, D.R., Williams, J.G., 2006. A numerical analysis of the elastic-plastic peel test. Eng. Fract. Mech. 73, 2324-2335.

Hamoush, S.A., Ahmad, S.H., 1989. Fracture energy release rate of adhesive joints. Int. J. Adhes. Adhes. 9, 171-178.

Hart-Smith, L.J., 1973. Adhesive-bonded double-lap joints. NASA technical report CR-112235.

Hart-Smith, L.J., 1981. Effects of Flaws and Porosity on Strength of Adhesive-Bonded Joints. Douglas Aircraft Company Report MDC J4699, November 1981.

Harter, P., 2004. Certifying Bonded Structure – Adam Aircraft's Experience. FAA Bonded Structures Workshop, Seattle (USA), June 16-18, 2004.

Hoyt, D.M., Ward, S., 2004. Composite Bonded Joints Analysis, Data, and Substantiation. FAA Bonded Structures Workshop, Seattle (USA), June 16-18, 2004.

Hunston, D.L., Kinloch, A.J., Wang, S.S., 1989. Micromechanics of fracture in structural adhesive bonds. J. Adhesion 28, 103-114.

Hutchinson, J.W., Evans, A.G., 2000. Mechanics of materials: top-down approaches to fracture. Acta Mater. 48, 125-135.

Imanaka, M., Nakamura, Y., Nishimura, A., Iida, T., 2003. Fracture toughness of rubber-modified epoxy adhesives: effect of plastic deformability of the matrix phase. Comp. Sci. Technol. 63, 41-51.

Imanaka, M., Motohashi, S., Nishi, K., Nakamura, Y., Kimoto, M., 2009. Crack-growth behaviour of epoxy adhesives modified with liquid rubber and cross-linked rubber particles under mode I loading. Int. J. Adhes. Adhes. 29, 45-55.

Irwin, G.R., 1957. Analysis of stresses and strains near the end of crack traversing a plate. J. Appl. Mech. 24, 361-364.

Ivankovic, A., Pandya, K.C., Williams, J.G., 2004. Crack growth predictions in polyethylene using measured traction–separation curves. Eng. Fract. Mech. 71, 657-668.

Kafkalidis, M.S., Thouless, M.D., Yang, Q.D., Ward, S.M., 2000. Deformation and fracture of adhesive layers constrained by plastically-deforming adherends. J. Adhes. Sci. Technol. 14, 1593-1607.

Kawashita, L.F., Moore, D.R., Williams, J.G., 2004. The development of a mandrel peel test for the measurement of adhesive fracture toughness of epoxy-metal laminates. J. Adhesion 80, 147-167.

Kawashita, L.F., Moore, D.R., Williams, J.G., 2005. Comparison of Peel Tests for Metal–Polymer Laminates for Aerospace Applications. J. Adhesion 81, 561-586.

Kawashita, L.F., Moore, D.R., Williams, J.G., 2005. Analysis of peel arm curvature for the determination of fracture toughness in metal-polymer laminates. J. Mater. Sci. 40, 4541-4548.

Kawashita, L.F., Kinloch, A.J., Moore, D.R., Williams, J.G., 2008. The influence of bond line thickness and peel arm thickness on adhesive fracture toughness of rubber toughened epoxy–aluminium alloy laminates. Int. J. Adhes. Adhes. 28, 199-

210.

Kinloch, A.J., Shaw, S.J., 1981. The fracture resistance of a toughened epoxy adhesive. J. Adhes. 12, 59-77.

Kinloch, A.J., 1987. Adhesion and Adhesives: Science and Technology, first ed. Chapman & Hall, London.

Kinloch, A.J., Lau, C.C., Williams, J.G., 1994. The peeling of flexible laminates. Int. J. Fracture 66, 45-70.

Kinloch, A.J., 1997. Adhesives in engineering. Proc. Intsn Mech. Engrs Part G 211, 307-335.

Kim, K-S., Aravas, N., 1988. Elastoplastic analysis of the peel test. Int. J. Solids Struct. 24, 417-435.

Landis, C.M., Pardoen, T., Hutchinson, J.W., 2000. Crack velocity dependent toughness in rate dependent materials. Mech. Mater. 32, 663-678.

Li, S., Thouless, M.D., Waas, A.M., Schroeder, J.A., Zavattieri, P.D., 2006. Competing failure mechanisms in mixed-mode fracture of an adhesively bonded polymer-matrix composite. Int. J. Adhes. Adhes. 26, 609-616.

Liebl, C., Johlitz, M., Yagimli, B., Lion, A., 2012. Three-dimensional chemo-thermomechanically coupled simulation of curing adhesives including viscoplasticity and chemical shrinkage. Comput. Mech. 49, 603-615.

Martiny, Ph., Kinloch, A.J., Lani, F., Landis, C.M., Pardoen, T., 2005. Multiscale modelling of the steady-state fracture of adhesively-bonded joints. In: Proc. 28th Annual Meeting of the Adhesion Society. Mobile, USA, 2005. p.360.

Martiny, Ph., Lani, F., Kinloch, A.J., Pardoen, T., 2008. Numerical analysis of the energy contributions in peel tests: a steady-state multilevel finite element approach. Int. J. Adhes. Adhes. 28, 222-236.

Martiny, Ph., Lani, F., Kinloch, A.J., Pardoen, T., 2012. A multiscale parametric study of mode I fracture in metal-to-metal low-toughness adhesive joints. Int. J. Fract. 173, 105-133.

McAuliffe, D., Karac, A., Murphy, N., Ivankovic, A., 2011. Transferability of Adhesive Fracture Toughness Measurements between Peel and TDCB Test Methods for a

Nano-Toughened Epoxy. Proceedings of the 34th annual meeting of the Adhesion Society, Savannah (USA).

McCarthy, J.C., 1996. Summary report. MTS Adhesives Project 2: Failure Modes and Criteria, AEAT-0126, AEA Harwell.

MIL-HDBK-17-3F, 2002. Department of defense handbook. Composite Materials Handbook. Volume 3. Polymer matrix composites. Materials usage, design and analysis.

MIL-HDBK-691B, 1987. Military Standardization Handbook. Adhesive bonding.

MIL-HDBK-83377, 1997. Deparment of Defense Handbook. Adhesive bonding (structural) for aerospace and other systems, requirements for.

Minamo, 2010. Web page: www.cenaero.be/Minamo .

Mortensen, F., Thomsen, O.T., 2002. Analysis of Adhesive Bonded Joints: A Unified Approach. Comp. Sci. Technol. 62, 1011-1031.

Needleman, A., 1987. A continuum model for void nucleation by inclusion debonding. J. Appl. Mech. 54, 525-531.

Oplinger, D. W., 1994. Effects of Adherend Deflections in Single Lap Joints. Int. J. Solids Struct. 31, 2565-2587.

Panigrahi, S.K., Pradhan, B., 2007. Adhesion failure propagation in adhesively-bonded single-lap laminated FRP composite joints. J. Adhes. Sci. Technol. 21, 379-398.

Papini, M., Fernlund, G., Spelt, J.K., 1994. The effect of geometry on the fracture of adhesive joints. Int. J. Adhes. Adhes. 14, 5-13.

Pardoen, T., Marchal, Y., Delannay, F., 1999. Thickness dependence of cracking resistance in thin aluminium plates. J. Mech. Phys. Solids 47, 2093-2123.

Pardoen, T., Hachez, F., Marchioni, B., Blyth, P.H., Atkins, A.G., 2004. Mode I fracture of sheet metal. J. Mech. Phys. Solids 52, 423-452.

Pardoen, T., Ferracin, T., Landis, C.M., Delannay, F., 2005. Constraint effects in adhesive joint fracture. J. Mech. Phys. Solids 53, 1951-1983.

Pardoen, T., Pineau, A., 2007. Failure mechanisms of metals. In: Comprehensive structural integrity encyclopedia, vol. 2., Elsevier, Amsterdam.

Raghava, R., Caddell, R.M. Yeh, G.S.Y., 1973. The macroscopic yield behaviour of polymers. J. Mater. Sci 8, 225-232.

Rice, J.R., 1967. Fatigue crack propagation. In: Fatigue Crack Propagation, ASTM-STP 415, pp. 247.

Rice, J.R., Tracey, D.M., 1969. On the ductile enlargement of voids in triaxial stress fields. J. Mech. Phys. Solids 17, 201-217.

Ritchie, R.O., Knott, J.F., Rice, J.R., 1973. On the relationship between tensile stress and fracture toughness in mild steels. J. Mech. Phys. Solids 21, 395–410.

Roylance, D., 1996. Mechanics of materials. John Wiley & Sons, New York.

Salomonsson, K., Andersson, T., 2008. Modelling and parameter calibration of an adhesive layer at the meso level. Mech. Mater. 40, 48-65.

Siegmund, T., Brocks, W., 1998. Local fracture criteria: lengthscales and applications. Proceedings of the 2nd Euromech-Mecamat Conference, Magdeburg (Germany), 347-354.

Siegmund, T., Brocks, W., 1999. Prediction of the work of separation and implications to modelling. Int. J. Frac. 99, 97-116.

Sun, C., Thouless, M.D., Waas, A.M., Schroeder, J.A., Zavattieri, P.D., 2009. Rate effects in mode-II fracture of plastically deforming, adhesively bonded structures. Int. J. Fracture 156, 111-128.

Swift, H.W., 1952. Plastic instability under plane stress. J. Mech. Phys. Solids 1, 1-18.

Tomblin, J., Strole, K., Dodosh, G., Ilcewicz, L., 2005. Assessment of industry practices for aircraft bonded joints and structures. U.S. Department of Transportation. Federal Aviation Administration. Report DOT/FAA/AR-05/13.

Tvergaard, V., 1990. Effect of fiber debonding in a whisker-reinforced metal. Mater. Sci. Eng. A 125, 203-213.

Tvergaard, V., Hutchinson, J.W., 1992. The relation between crack growth resistance and fracture process parameters in elastic-plastic solids. J. Mech. Phys. Solids 40, 1377-1397.

Tvergaard, V., Hutchinson, J.W., 1994. Toughness of an interface along a thin ductile layer joining elastic solids. Philos. Mag. A 70, 641-656.

Tvergaard, V., Hutchinson, J.W., 1996. Effect of strain-dependent cohesive zone model on predictions of crack growth resistance. Int. J. Solids Struct. 33, 3297-3308.

Tvergaard, V., Hutchinson, J.W., 1996. On the toughness of ductile adhesive joints. J. Mech. Phys. Solids 44, 789-800.

Volkersen, O., 1938. Die Nietkraftverteilung in zugbeanspruchten Nietverbindungen mit konstanten Laschenquerschnitten. Luftfahrtforschung 15, 41.

Voto, C., 2004. Alenia experience in metal bonding. FAA Bonded Structures Workshop, London (UK), October 26-27, 2004.

Wei, Y., Hutchinson, J.W., 1997. Nonlinear delamination mechanics for thin films. J. Mech. Phys. Solids 45, 1137-1159.

Wucher, B., 2009. Simulation transitoire de la rupture de joints collés. Student project report. Cenaero.

Yang, Q.D., Thouless, M.D., Ward, S.M., 1999. Numerical simulations of adhesively-bonded beams failing with extensive plastic deformation. J. Mech. Phys. Solids 47, 1337-1353.

Yang, Q.D., Thouless, M.D., Ward, S.M., 2000. Analysis of the symmetrical 90°-peel test with extensive plastic deformation. J. Adhes. 72, 115-132.

List of publications

Scientific papers in relation to the present thesis

Martiny, Ph., Lani, F., Kinloch, A.J., Pardoen, T., 2008. Numerical analysis of the energy contributions in peel tests: a steady-state multilevel finite element approach. Int. J. Adhes. Adhes. 28, 222-236.

Martiny, Ph., Lani, F., Kinloch, A.J., Pardoen, T., 2012. A multiscale parametric study of mode I fracture in metal-to-metal low-toughness adhesive joints. Int. J. Fract. 173, 105-133.

Martiny, Ph., Lani, F., Kinloch, A.J., Pardoen, T., 2012. A maximum stress at a distance criterion for the prediction of fracture in adhesively-bonded joints. Submitted to Engineering Fracture Mechanics.

Communications in conferences in relation to the present thesis

Martiny, Ph., Kinloch, A.J., Lani, F., Landis, C., Pardoen, T., 2005. Multiscale modelling of the steady-state fracture of adhesively-bonded joints. 28th Annual Adhesion Society Meeting, February 2005, Mobile, Alabama (USA)

Martiny, Ph., Lani, F., Landis, C., Kinloch, A.J., Pardoen, T., 2005. Parametric study of the plastic dissipation in the peeling of adhesively-bonded joints. 9th International Conference on the Science and Technology of Adhesion and Adhesives, 7-9 September 2005, Oxford (UK)

Martiny, Ph., Kinloch, A.J., Lani, F., Landis, C., Pardoen, T., 2006. Parametric study of the plastic dissipation in the peeling of adhesively-bonded joints. 7th National Congress on Theoretical and Applied Mechanics, May 29-30 2006, Mons (Belgium)

Martiny, Ph., Lani, F., Kinloch, A.J., Pardoen, T., 2008. Micro-mechanical modelling of the fracture of adhesively-bonded joints under steady-state peeling conditions. 5th ESIS TC4 Conference on the Fracture of Polymers, Composites and Adhesives, 7-11 September 2008, Les Diablerets (Switzerland)

Martiny, Ph., Lani, F., Kinloch, A.J., Pardoen, T., 2009. Micro-mechanical modelling of the fracture in adhesive joints. 32nd Annual Adhesion Society meeting, February 2009, Savannah, Georgia (USA)

Martiny, Ph., Lani, F., Kinloch, A.J., Pardoen, T., 2011. A damage-based model for the fracture of rubber-toughened epoxy adhesives. 6th ESIS TC4 Conference on the Fracture of Polymers, Composites and Adhesives, 11-15 September 2011, Les Diablerets (Switzerland)

Other selected publications

Wyart, E., Dulfot, M., Coulon, D., Martiny, Ph., Pardoen, T., Remacle, J.F., Lani, F., 2007. A substructured FE/XFE method for stress-intensity factors computation in an industrial structure. European Journal of Mechanics 16, 199-212

Wyart, E., Dulfot, M., Coulon, D., Martiny, Ph., Pardoen, T., Remacle, J.F., Lani, F., 2008. Substructuring FE-XFE approaches applied to three-dimensional crack propagation. J. Comp. Appl. Math. 215, 626-638

Martiny, Ph., Carlier, V., Bertin, A., Lani, F., 2011. Minimal experimental characterization for accurate prediction of the cure-induced deformations in composites. 16th International Conference on Composite Structures (ICCS 16), 28-30 June 2011, Porto (Portugal)

Ph. Martiny, 2011. La prédiction des déformations en sortie de cuisson en vue de la compensation de moule. Séminaire NAFEMS «Matériaux composites et simulation numérique», 30 November 2011, Noisy (France).